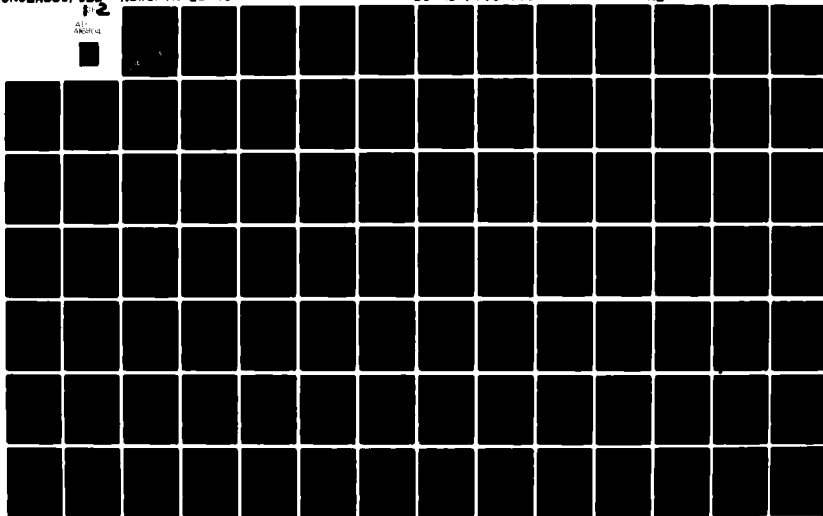


AD-A116 904

NAVAL SURFACE WEAPONS CENTER SILVER SPRING MD F/G 16/4  
AN INVISCID COMPUTATIONAL METHOD FOR TACTICAL MISSILE CONFIGURA--ETC(U)  
DEC 81 A B WARDLAW, F P BALTAKIS, J M SOLOMON  
NSWC/TR-81-457 SBI-AD-F500 038 NL

UNCLASSIFIED

1-2  
ALL INFORMATION CONTAINED  
HEREIN IS UNCLASSIFIED



AT-F500038

12

AD A116904

NSWC TR 81-457

## AN INVISCID COMPUTATIONAL METHOD FOR TACTICAL MISSILE CONFIGURATIONS

BY A. B. WARDLAW, JR., F. P. BALTAKIS,  
J. M. SOLOMON, L. B. HACKERMAN

RESEARCH AND TECHNOLOGY DEPARTMENT

1 DECEMBER 1981

Approved for public release, distribution unlimited.

DTIC  
ELECTE  
JUL 13 1982  
S B



NAVAL SURFACE WEAPONS CENTER

Dahlgren, Virginia 22448 • Silver Spring, Maryland 20910

DTIC FILE COPY

82 07 06 037

UNCLASSIFIED

SECURITY CLASSIFICATION OF THIS PAGE (When Data Entered)

REPORT DOCUMENTATION PAGE		READ INSTRUCTIONS BEFORE COMPLETING FORM
1. REPORT NUMBER NSWC TR 81-457	2. GOVT ACCESSION NO. AD-A116 904	3. RECIPIENT'S CATALOG NUMBER
4. TITLE (and Subtitle) AN INVISCID COMPUTATIONAL METHOD FOR TACTICAL MISSILE CONFIGURATIONS		5. TYPE OF REPORT & PERIOD COVERED
		6. PERFORMING ORG. REPORT NUMBER
7. AUTHOR(s) A. B. Wardlaw, Jr., F. P. Baltakis, J. M. Solomon L. B. Hackerman		8. CONTRACT OR GRANT NUMBER(s)
9. PERFORMING ORGANIZATION NAME AND ADDRESS Naval Surface Weapons Center White Oak Silver Spring, MD 20910		10. PROGRAM ELEMENT, PROJECT, TASK AREA & WORK UNIT NUMBERS
11. CONTROLLING OFFICE NAME AND ADDRESS		12. REPORT DATE 1 December 1981
		13. NUMBER OF PAGES 117
14. MONITORING AGENCY NAME & ADDRESS (if different from Controlling Office)		15. SECURITY CLASS. (of this report) UNCLASSIFIED
		15a. DECLASSIFICATION/DOWNGRADING SCHEDULE
16. DISTRIBUTION STATEMENT (of this Report)  Approved for public release, distribution unlimited		
17. DISTRIBUTION STATEMENT (of the abstract entered in Block 20, if different from Report)		
18. SUPPLEMENTARY NOTES		
19. KEY WORDS (Continue on reverse side if necessary and identify by block number)  Tactical Missile Numerical Methods		
20. ABSTRACT (Continue on reverse side if necessary and identify by block number)  A finite difference method suitable for the design of finned bodies in supersonic flight is described. Efficient numerical calculations are achieved using a thin fin approximation which neglects fin thickness but retains a description of the fin surface slope. The resulting algorithm is suitable for treating relatively thin, straight fins with sharp edges which may be deflected. Methods for treating the fin leading and trailing edges are described which are dependent on the Mach number of the flow normal to the leading edge. The leading and trailing edge analysis varies from exact to		

DD FORM 1473

EDITION OF 1 NOV 65 IS OBSOLETE  
S/N 3102-LF-014-6601

UNCLASSIFIED

SECURITY CLASSIFICATION OF THIS PAGE (When Data Entered)

UNCLASSIFIED

SECURITY CLASSIFICATION OF THIS PAGE (When Data Entered)

20. (Cont.)

empirical as the normal component varies from a supersonic to subsonic. A procedure for modeling body crossflow separation using a Kutta condition is described which yields a reasonable leeward vortex structure. Calculations are compared to experiment for body-alone, body-wing, body-tail and body-wing-tail configurations. The computer program, developed in this study, is described in a separate report.

UNCLASSIFIED

SECURITY CLASSIFICATION OF THIS PAGE (When Data Entered)

## FOREWORD

A finite difference method suitable for the design of finned bodies in supersonic flight is described. Efficient numerical calculations are achieved using a thin fin approximation which neglects fin thickness but retains a description of the fin surface slope. The resulting algorithm is suitable for treating relatively thin, straight fins, with sharp edges which may be deflected. Methods for treating the fin leading and trailing edges are described which are dependent on the Mach number of the flow normal to the leading edge. The leading and trailing edge analysis varies from exact to empirical as the normal component varies from a supersonic to subsonic. A procedure for modeling body crossflow separation using a Kutta condition is described which yields a reasonable leeside vortex structure. Calculations are compared to experiment for body-alone, body-wing, body-tail and body-wing-tail configurations. The computer program, developed in this study, is described in a separate report.

*Ira M. Blatstein*

IRA M. BLATSTEIN  
By direction

Accession For	
NTIS GRA&I	<input checked="" type="checkbox"/>
DTIC TAB	<input type="checkbox"/>
Unannounced	<input type="checkbox"/>
Justification	
Ev	
Distribution	
Availability Codes	
Av. to pub. or	
Dist	Special
A	



## CONTENTS

<u>Section</u>		<u>Page</u>
1	INTRODUCTION.....	9
2	COMPUTATIONAL ALGORITHM .....	11
	2.1 COMPUTATIONAL REGION.....	11
	2.2 INTERIOR, BODY, AND SHOCK POINTS.....	12
	2.3 FIN SURFACES.....	19
	2.3.1 THE THIN FIN APPROXIMATION AND IMPLEMENTATION..	19
	2.3.2 FIN SURFACE BOUNDARY CONDITIONS.....	20
	2.4 FIN EDGES AND SURFACE SLOPE DISCONTINUITIES.....	24
	2.4.1 LEADING EDGES.....	24
	2.4.2 TRAILING EDGES.....	26
	2.4.3 SURFACE SLOPE DISCONTINUITIES.....	27
	2.4.4 EXPANSION AND COMPRESSION TURNS.....	28
	2.5 TREATMENT OF INLETS.....	31
3	SPECIAL PROCEDURES.....	35
	3.1 ALTERATION OF X DIFFERENCING FOR FIN AND INTERIOR POINTS ADJACENT TO THE FIN TIP.....	35
	3.2 SUPPRESSION OF Y DERIVATIVES NEAR THE LEADING EDGE...	36
	3.3 APPLICATION OF SMOOTHING TO INTERIOR, BODY, AND FIN POINTS.....	37
	3.4 BODY CROSSFLOW SEPARATION.....	38
4	COMPARISON OF CALCULATION AND EXPERIMENT.....	41
	4.1 BODY ALONE.....	41
	4.2 CONFIGURATIONS WITH SUPERSONIC LEADING EDGES.....	42
	4.3 CONFIGURATIONS WITH TRANSONIC LEADING EDGES.....	43
	4.4 CONFIGURATIONS WITH SUBSONIC LEADING EDGES.....	44
5	CONCLUDING REMARKS.....	47
	REFERENCES.....	93
	NOMENCLATURE.....	97
	APPENDIX A - CHARACTERISTIC ANALYSIS OF THE FIN SURFACE.....	A-1
	APPENDIX B - CALCULATION OF AERODYNAMIC COEFFICIENTS.....	B-1

## ILLUSTRATIONS

<u>Figure</u>		<u>Page</u>
1	CYLINDRICAL COORDINATE SYSTEM USED FOR INVISCID FLOW CALCULATIONS.....	49
2	THIN FIN APPROXIMATIONS IN PHYSICAL AND COMPUTATIONAL COORDINATES.....	50
3	VECTORS USED IN THE ANALYSIS OF FIN LEADING, TRAILING EDGES AND SURFACE SLOPE DISCONTINUITIES.....	51
4	THE EFFECT OF CHANGING THE LEADING EDGE PRESSURE AND STREAMLINE DIRECTION ON A SWEEP WING SURFACE PRESSURE PROFILE.....	52
5	VECTORS ASSOCIATED WITH COMPRESSION AND EXPANSION TURNS.....	53
6	COMPRESSION REGIMES USED IN OPTION 1 ANALYSIS.....	54
7	EFFECT OF SUPPRESSING Y DERIVATIVES FOR VARIOUS STRENGTH JUMPS AT THE LEADING EDGE.....	55
8	CROSSFLOW PLANE WITH AND WITHOUT PRESCRIBED SEPARATION.....	55
9	EXPERIMENTAL AND CALCULATED FLOW FIELDS ON A BODY ALONE CONFIGURATION, $\alpha = 15^\circ$ , $M = 3.0$ , $Z = 13$ CALIBERS, REFERENCE 20.....	56
10	BODY ALONE SURFACE PRESSURE DISTRIBUTIONS WITH AND WITHOUT BODY CROSSFLOW SEPARATION, $\alpha = 15^\circ$ , $M = 3.0$ , $Z = 13$ CALIBERS.....	57
11	CALCULATED AND MEASURED FIN SURFACE PRESSURES ON A CLIPPED DELTA FIN CONFIGURATION IN THE "+" ROLL POSITION, $\alpha = 3.8^\circ$ , $M = 3.7$ , REFERENCE 21.....	58
12	CALCULATED AND MEASURED FIN SURFACE PRESSURES ON A CLIPPED DELTA FIN CONFIGURATION IN THE "+" ROLL POSITION, $\alpha = 7.8^\circ$ , $M = 3.7$ , REFERENCE 21.....	59
13	CALCULATED AND MEASURED FIN SURFACE PRESSURES ON A CLIPPED DELTA FIN CONFIGURATION IN THE "X" ROLL POSITION, $\alpha = 3.8^\circ$ , $M = 3.7$ , REFERENCE 21.....	60
14	CALCULATED AND MEASURED FIN SURFACE PRESSURES ON A CRANKED DELTA FIN CONFIGURATION IN THE "X" ROLL POSITION, $\alpha = 3.8^\circ$ , $M = 3.7$ , REFERENCE 21.....	61
15	CALCULATED AND MEASURED FIN SURFACE PRESSURES ON A CRANKED DELTA FIN CONFIGURATION IN THE "+" ROLL POSITION, $\alpha = 7.8^\circ$ , $M = 3.7$ , REFERENCE 21.....	62
16	CALCULATED CROSSFLOW FIELD PRESSURE AND DENSITY CONTOURS FOR A CLIPPED DELTA FIN CONFIGURATION IN THE "+" ROLL POSITION, $\alpha = 7.8^\circ$ , $M = 3.7$ , $Z = 37$ , REFERENCE 21 .....	63

## ILLUSTRATIONS (Cont.)

<u>Figure</u>		<u>Page</u>
17	CALCULATED AND MEASURED NORMAL FORCE COEFFICIENT, $C_N$ AND CENTER OF PRESSURE, $Z_{ac}/L$ , FOR BODY-WING AND BODY-WING-TAIL CONFIGURATIONS OF REFERENCE 20, at $M = 2.0$ , $\alpha \pm 10^\circ$ .....	64
18	CALCULATED CROSSFLOW FIELD FOR THE BODY-WING-TAIL CONFIGURATION OF REFERENCE 22, $M = 2.0$ , $\alpha = 10^\circ$ .....	65
19	CALCULATED AND MEASURED FIN SURFACE PRESSURES ON THE THIN SWEPT WING CONFIGURATION OF REFERENCE 14 AT $M = 4.5$ , $\alpha = 2^\circ$ and $6^\circ$ .....	67
20	CALCULATED AND MEASURED FIN SURFACE PRESSURES ON A THICK SWEPT WING CONFIGURATION OF REFERENCE 14 AT $M = 4.5$ , $\alpha = 2^\circ$ and $6^\circ$ .....	68
21	CALCULATED AND MEASURED FIN SURFACE PRESSURES ON A THIN SWEPT WING CONFIGURATION OF REFERENCE 14 AT $M = 2.5$ , $\alpha = 2^\circ$ and $6^\circ$ ..	69
22	CALCULATED AND MEASURED FIN SURFACE PRESSURES ON A THICK SWEPT WING CONFIGURATION OF REFERENCE 14 AT $M = 2.5$ , $\alpha = 2^\circ$ and $6^\circ$ ..	70
23	CALCULATED AND MEASURED BODY SURFACE PRESSURES ON THE THICK SWEPT WING CONFIGURATION OF REFERENCE 14 AT $M = 2.5$ , $\alpha = 2^\circ$ and $6^\circ$ .....	71
24	CALCULATED AND MEASURED BODY SURFACE PRESSURES ON THE THICK SWEPT WING CONFIGURATION OF REFERENCE 14 AT $M = 4.5$ , $\alpha = 2^\circ$ AND $6^\circ$ .....	72
25	CALCULATED CROSSFLOW FIELD ON THE THIN SWEPT WING CONFIGURATION OF REFERENCE 14 AT $M = 4.5$ , $\alpha = 6^\circ$ , $Z = 62$ .....	73
26	CALCULATED CROSSFLOW FIELD ON THE THIN SWEPT WING CONFIGURATION OF REFERENCE 14 AT $M = 2.5$ , $\alpha = 6^\circ$ , $Z = 62$ .....	74
27	CALCULATED AND MEASURED FIN SURFACE PRESSURES ON THE DELTA WING CONFIGURATION OF REFERENCE 23, IN THE "+" ROLL POSITION AT $M = 2.7$ , $\alpha = 10^\circ$ .....	75
28	CALCULATED AND MEASURED FIN SURFACE PRESSURES ON THE DELTA WING CONFIGURATION OF REFERENCE 23, IN THE "X" ROLL POSITION AT $M = 2.7$ , $\alpha = 10^\circ$ .....	76
29	CALCULATED AND MEASURED BODY SURFACE PRESSURES ON THE DELTA WING CONFIGURATION OF REFERENCE 23, IN THE "+" ROLL POSITION AT $M = 2.7$ , $\alpha = 10^\circ$ .....	77
30	CALCULATED AND MEASURED BODY SURFACE PRESSURES ON THE DELTA WING CONFIGURATION OF REFERENCE 23, IN THE "X" ROLL POSITION AT $M = 2.7$ , $\alpha = 10^\circ$ .....	78



NSWC TR 81-457  
ILLUSTRATIONS (Cont.)

Figure		<u>Page</u>
31	CALCULATED CROSSFLOW FIELD ON THE DELTA WING CONFIGURATION OF REFERENCE 23 IN THE "+" ROLL POSITION AT $M = 2.7$ , $\alpha = 10^\circ$ , $Z = 36.5$ .....	79
32	CALCULATED CROSSFLOW FIELD ON THE DELTA WING CONFIGURATION OF REFERENCE 23 IN THE "X" ROLL POSITION AT $M = 2.7$ , $\alpha = 10^\circ$ , $Z = 36.5$ .....	80
33	CALCULATED AND MEASURED WING SURFACE PRESSURES ON THE SWEEPED WING CONFIGURATION OF REFERENCE 24 AT $M = 2.3$ AND $\alpha = 8.8^\circ$ .....	81
34	CALCULATED AND MEASURED WING SURFACE PRESSURES ON THE SWEEPED WING CONFIGURATION OF REFERENCE 24 AT $M = 2.96$ AND $\alpha = 8.6^\circ$ .....	82
35	CALCULATED AND MEASURED BODY SURFACE PRESSURES ON THE SWEEPED WING CONFIGURATION OF REFERENCE 24 AT $M = 2.3$ AND $\alpha = 8.8^\circ$ .....	83
36	CALCULATED AND MEASURED BODY SURFACE PRESSURES ON THE SWEEPED WING CONFIGURATIONS OF REFERENCE 24 AT $M = 2.96$ AND $\alpha = 8.6^\circ$ .....	84
37	CALCULATED CROSSFLOW PLANE FLOW FIELD ON THE DELTA WING CONFIGURATION OF REFERENCE 24 AT $M = 2.3$ , $\alpha = 8.8^\circ$ AND $Z = 36$ .....	85
38	CALCULATED CROSSFLOW PLANE FLOW FIELD ON THE DELTA WING CONFIGURATION OF REFERENCE 24 AT $M = 2.96$ , $\alpha = 8.6^\circ$ AND $Z = 36$ .....	86
39	CALCULATED AND MEASURED SURFACE PRESSURES ON THE DELTA WING OF REFERENCE 26 AT $M = 2.86$ AND $\alpha = 10.3^\circ$ .....	87
40	CALCULATED CROSSFLOW PLANE FLOW FIELD ON THE DELTA WING CONFIGURATION OF REFERENCE 26 AT $M = 2.86$ AND $\alpha = 10.3^\circ$ THE ILLUSTRATED STATION IS UPSTREAM OF THE TRAILING EDGE.....	88
41	CALCULATED AND MEASURED NORMAL FORCE COEFFICIENT AND CENTER OF PRESSURE FOR TWO WING-BODY-TAIL CONFIGURATIONS OF REFERENCE 27 AT $\alpha = 6^\circ$ AND $12^\circ$ , $M = 2.86$ AND TAIL UNDEFLECTED.....	89
42	CALCULATED AND MEASURED NORMAL FORCE COEFFICIENT AND CENTER OF PRESSURE FOR TWO WING-BODY-TAIL CONFIGURATIONS OF REFERENCE 27 AT $\alpha = 6^\circ$ AND $12^\circ$ , $M = 2.86$ AND TAIL DEFLECTED TO $20^\circ$ .....	90
43	CALCULATED CROSSFLOW PLANE FLOW FIELD FOR THE W1 BODY-WING-TAIL CONFIGURATION OF REFERENCE 27 AT $M = 2.86$ AND $\alpha = 12^\circ$ . THE FORWARD PLANE IS DOWNSTREAM OF THE WING TRAILING EDGE, THE MIDDLE STATION IS UPSTREAM OF THE TAIL LEADING EDGE, THE REAR STATION IS DOWNSTREAM OF THE TAIL TRAILING EDGE.....	91

## SECTION 1

## INTRODUCTION

A practical means of predicting the nonlinear, inviscid, supersonic shock layer on missile configurations is to numerically solve the steady, three-dimensional inviscid equations using an efficient finite difference method. Several computer programs are currently available for calculating flow fields about arbitrary bodies in supersonic flow. However, their application to practical wing-body-tail configurations presents some serious computational problems. Existing codes treat the complete fin-body cross section as a single entity. Thus when cylindrical coordinates described in Figure 1 are used, a large number of  $\phi$  mesh planes are needed to adequately resolve the fin. When several fins are present at the same axial station, the number of grid points needed becomes prohibitively large for practical design calculations. The number of grid points can be substantially reduced by mapping the fin body cross-section into a more rounded figure. The existing methods utilizing this approach are based on conformal mapping techniques developed by Moretti<sup>2,8</sup> (also see References 3 and 6). However, the mappings are complicated even for the case of a single smooth fin or wing and often tend to cluster large number of mesh points near wing tips. This reduces the permissible marching step and increases computational time.

The primary focus of the present study is the development of a more efficient numerical technique for treating finned bodies. To achieve this, the approach used here departs from the basic computational strategy used in References 1-7 when fin surfaces are present. Instead of considering the cross-sectional body-fin geometry as a single entity, the present method considers the body alone (i.e., the body with all fin surfaces removed) and the fin geometries separately. The computational grid is generated using normalizing transformations<sup>1,4,5,7</sup> applied to the body alone configuration. The fin surfaces are allowed to extend into the computational region and can be adequately resolved within a relatively coarse computational grid. In order to treat the complex flow in the immediate vicinity of fin leading and trailing edges, appropriate local analyses are built into the program which depend strongly on the local Mach number of the flow component normal to the edge. These local analyses can range from locally exact, when the edge is sharp and the normal velocity component is sufficiently supersonic, to ad hoc or semi-empirical in other situations. It is possible to exercise the above computational procedure without recourse to a special leading edge analysis. However, such a procedure is not as robust and does not resolve the leading edge region as accurately.

Within this framework, various approaches for numerically treating general fin surface shapes are possible. One approach is to introduce extra computational points to represent the fin surfaces which would float within the basic grid. This would complicate the application of the boundary conditions on the fin surfaces. Another approach, is to subdivide the flow domain into several sub-regions each containing the flow between adjacent fin surfaces. Relatively simple transformations are applied separately in each sub-region to map adjacent fin surfaces onto constant computational coordinate planes. Relatively coarse meshes could be used in each sub-region and the computations in the various sub-regions could be linked in a manner suggested by Hindman, et al.<sup>9</sup> Both the above mentioned approaches are in principle capable of handling general fin surface geometries.

To simplify the development for the present study, the analysis is restricted to relatively thin fins with sharp edges which lie approximately along constant  $\phi$  planes. A thin fin approximation is employed which neglects the fin thickness but retains the actual fin surface slopes. For an important class of body-fin configurations, the thin fin approximation allows the direct use of the basic grid generated for the body alone shape without the introduction of floating points to describe the fin surface or additional mappings.

A computer program has been developed using the thin fin algorithm which is capable of treating configurations with a large number of lifting surfaces. The types of geometries which can be handled are restricted as follows:

1. The body alone surface,  $b(z, \phi)$ , must be single valued in  $\phi$ . This precludes a direct treatment of items such as detached inlets.
2. Fins must be relatively thin and lie near constant  $\phi$  planes. In practice it has been found that reasonable agreement can be obtained between calculation and experiment on relatively thick or deflected fins. By moving the coordinate system origin, it is often possible to position fins along constant  $\phi$  planes.
3. Fin edges must be sharp and the fin edge radial location,  $l(z)$ , can be single or double valued in  $z$ . This allows swept trailing edge configurations to be treated.
4. Fins cannot extend through the bow shock.

In addition to the above requirements, the flow field must remain supersonic throughout the entire calculation. This precludes bodies with blunt protuberances which feature upstream subsonic flow.

The computational method described in this report is an extension of the method developed earlier for re-entry bodies with cuts and flaps. A detailed description of this method is contained in Reference 10 and will be only briefly outlined here. The present report provides a description of the analysis for configurations with fins, various special procedures required for different configurations and flow conditions, and also comparisons of the numerical results with available experimental data. A description of the computer program and user guide is provided in Reference 11.

## SECTION 2

## COMPUTATIONAL ALGORITHM

Euler's equations are solved numerically in a region bounded by the missile body (i.e., with lifting surfaces excluded) and the bow shock. At interior points these equations are cast in weak conservation form and advanced using the MacCormack predictor-corrector method. At the body, fin surfaces and bow shock, special sets of equations are solved using the MacCormack predictor-corrector method with appropriate one-sided differences. These sets of relations combine the admissible characteristic compatibility relations and the appropriate boundary condition.

2.1 COMPUTATIONAL REGION

The flow field equations are initially written in cylindrical coordinates  $(r, \phi, z)$ , shown in Figure 1, and then transformed into  $(X, Y, Z)$  coordinates for the purpose of numerical integration. The current computational algorithm admits transformations of the form:

$$Z = z, X = X(r, \phi, z), Y = Y(\phi, z) \quad (1)$$

This transformation maps each crossflow plane into the square computational domain depicted in Figure 2. The missile body (i.e., excluding the lifting surfaces) and shock are located at  $X=0$  and  $X=1$  respectively while the  $Y=0$  and  $Y=1$  planes correspond to  $\phi = 0$  and  $\phi = \phi_*$ . Fin surfaces are allowed to extend into the computational domain along constant  $Y$  planes. The thickness of fins is neglected via the thin fin assumption which is described later in this section. Two sets of variable values are carried at grid points describing a fin, one for the upper surface and the other for the lower surface. The required mapping is thus only a function of the body alone plus shock geometry and it is expressed as a composite of two transformations. The first is the usual normalizing transformation given by

$$\begin{aligned} \bar{x} &= [r - b(\phi, z)] / [c(\phi, z) - b(\phi, z)] \\ \bar{y} &= \phi / \phi_*, \quad \bar{z} = z \end{aligned} \quad (2)$$

The second mapping is primarily used to cluster computational points in  $r, \phi, z$  space while retaining a uniform grid in the computational region. This mapping is conveniently expressed in inverted form as

$$\bar{x} = f(X, Y, Z), \quad \bar{y} = g(Y, Z), \quad \bar{z} = Z \quad (3)$$

where  $f(0,Y,Z) = 0$ ,  $f(1,Y,Z) = 1$ ;  $g(0,Z) = 0$ ,  $g(1,Z) = 1$ . Apart from these conditions, the mapping functions  $f$  and  $g$  are arbitrary provided that the functions and their derivatives through the second order are smoothly defined and  $f_X$  and  $g_Y$  are positive. In the present code the functions  $f$  and  $g$  can be analytically or numerically defined as is discussed in Reference 11. In the latter case the required derivatives are defined using second order finite difference methods. If mesh clustering is not required,  $f \equiv X$  and  $g \equiv Y$ . From (2) and (3):

$$\begin{aligned} Y_Z &= -g_Z/g_Y, \quad Y_\phi = 1/(\phi * g_Y), \\ X_r &= 1/[f_X(c-b)], \\ X_Z &= -(f_Z + Y_Z f_Y)/f_X + X_r[(f-1)b_Z - f c_Z], \\ X_\phi &= -Y_\phi f_Y/f_X + X_r[(f-1)b_\phi - f c_\phi]. \end{aligned} \quad (4)$$

When there are no fins present each computational plane,  $Z = \text{constant}$ , is covered by a uniform mesh defined by

$$\{(X_n, Y_m) : X_n = (n-1)\Delta X, Y_m = (m-1)\Delta Y, n = 1, 2, \dots, N; m = 1, 2, \dots, M\}$$

where  $\Delta X = 1/(N-1)$  and  $\Delta Y = 1/(M-1)$  for the symmetric case and  $\Delta Y = 1/M$  for the asymmetric case ( $N, M$  are positive integers). When fins are present, this computational mesh is modified by applying planar cuts along the fin surfaces.

The algorithm for advancing the unknown flow field quantities from  $Z = Z^k$  to  $Z^{k+1} = Z^k + \Delta Z$  depends on the location of the individual mesh point in the shock layer. These are divided into the following four types: interior, body surface, shock, and fin surface points. The procedure for treating the first three types of points is outlined in the next section with more details provided in Reference 10. This is followed by a discussion of the fin surface treatment. The derivation of the fin surface compatibility relations is provided in Appendix A.

## 2.2 INTERIOR, BODY, AND SHOCK POINTS

The flow field quantities at interior points are advanced using Euler's equations in weak conservation form:

$$\frac{\partial (r\tilde{U})}{\partial z} + \frac{\partial (r\tilde{F})}{\partial r} + \frac{\partial \tilde{G}}{\partial \phi} = \tilde{E} \quad (5)$$

where  $\tilde{U}, \tilde{F}, \tilde{G}$ , and  $\tilde{E}$  are column vectors defined in transpose form by

$$\begin{aligned} \tilde{U}^t &= (\rho w, p + \rho w^2, \rho w u, \rho w v) \\ \tilde{F}^t &= (\rho u, \rho w u, p + \rho u^2, \rho v u) \\ \tilde{G}^t &= (\rho v, \rho v w, \rho v u, p + \rho v^2) \\ \tilde{E}^t &= (0, 0, p + \rho v^2, -\rho u v). \end{aligned} \quad (6)$$

The energy equation for a steady inviscid flow with an isoenergetic free stream reduces to the following algebraic relation:

$$h + \frac{1}{2} (u^2 + v^2 + w^2) = h_\infty + \frac{1}{2} (u_\infty^2 + v_\infty^2 + w_\infty^2) = \text{const.} \equiv H_0 \quad (7)$$

The gas is assumed to be perfect which allows the system to be closed by applying the definition:

$$h = \frac{\gamma p}{(\gamma - 1)\rho} \quad (8a)$$

Additional thermodynamic relations which are used throughout this report are:

$$a^2 = \gamma p / \rho \quad (8b)$$

$$s = \ln p - \gamma \ln \rho \quad (8c)$$

The system (5) when transformed by (1) can be written as

$$\frac{\partial U}{\partial Z} + \frac{\partial F}{\partial X} + \frac{\partial G}{\partial Y} = E \quad (9)$$

where

$$U = rJ^{-1}\tilde{U}, \quad F = rJ^{-1} [X_Z\tilde{U} + X_r\tilde{F} + (X_\phi/r)\tilde{G}],$$

$$G = rJ^{-1}[Y_Z\tilde{U} + (Y_\phi/r)\tilde{G}], \quad E = (J^{-1})\tilde{E}, \quad J = (X_r Y_\phi)$$

The above equations are integrated using MacCormack differencing:

$$U_{n,m}^* = - \left( \frac{F_{n+I,m}^k - F_{n+I-1,m}^k}{\Delta X} \right) \Delta Z - \left( \frac{G_{n,m+J}^k - G_{n,m+J-1}^k}{\Delta Y} \right) \Delta Z + E_{n,m}^k \Delta Z + U_{n,m}^k \quad (10a)$$

$$U_{n,m}^{k+1} = \frac{1}{2} \left[ U_{n,m}^k + U_{n,m}^* - \left( \frac{F_{n+I-1,m}^* - F_{n-I,m}^*}{\Delta X} \right) \Delta Z - \left( \frac{G_{n,m+I-J}^* - G_{n,m-J}^*}{\Delta Y} \right) \Delta Z + E_{n,m}^* \Delta Z \right] \quad (10b)$$

where  $U^*$  is the predictor value and  $F_{n,m}^* = F(U^*, Z^{k+1}, X_m, Y_m)$ .

Here  $I, J = 1$  produces a forward difference in the predictor step and a backward difference in the corrector while  $I, J = 0$  yields a backward difference in the predictor step and forward difference in the corrector step. At the end of both the predictor and corrector steps the physical variables  $p, \rho, u, v, w$  are decoded from  $U$  and (7) using the relations:

$$w = \frac{U_2 [\gamma + \sqrt{1 - \phi}]}{U_1 (\gamma + 1)}, \quad \phi = (\gamma^2 - 1) \left[ H_0 \left( \frac{U_1}{U_2} \right)^2 - 1 \right] \quad (11)$$

$$u = U_3/U_1, \quad v = U_4/U_1$$

$$p = (U_2 - U_1 w)(J/r); \quad \rho = (U_1/w)(J/r)$$

The step size,  $\Delta Z$ , is chosen to satisfy the CFL stability conditions for the MacCormack scheme. This consists of ensuring that the domain of dependence of the partial differential equations is contained within the domain of dependence of the finite difference equation at all points. The derivation of the CFL condition for the MacCormack scheme is provided in Reference 10. The resulting relations are:

$$\Delta Z = \zeta \Delta X \min \left\{ \frac{w^2 - a^2}{\mu} \right\} \quad (12)$$

where:

$$\mu = \max(\mu_1, \mu_2, \mu_3)$$

$$\mu_1 = \left| wA - a^2 X_z \right| + a \sqrt{(w^2 - a^2)(X_r^2 + X_\phi^2/r^2) + (A - wX_z)^2}$$

$$\mu_2 = \left| \tilde{\delta} \left[ \left| wB - a^2 Y_z \right| + a \sqrt{(w^2 + v^2 - a^2)(Y_\phi^2/r^2)} \right] \right|$$

$$\mu_3 = \left| wA - a^2 X_z - \tilde{\delta}(wB - a^2 Y_z) \right|$$

$$+ a \sqrt{(w^2 - a^2) \left[ X_r^2 + \frac{1}{r^2} (X_\phi - \tilde{\delta} Y_\phi)^2 \right] + (wX_z - A + \tilde{\delta} v Y_\phi/r)^2}$$

$$\tilde{\delta} = \begin{cases} \Delta X/\Delta Y, & \text{if } I = J \\ -\Delta X/\Delta Y, & \text{if } I \neq J \end{cases}$$

$$A = X \frac{u}{r} + \frac{X_\phi}{r} v + X \frac{w}{z}; \quad B = \frac{Y_\phi v}{r} + Y \frac{w}{z}; \quad \delta = \text{safety factor} \sim .9$$

The minimum  $\Delta Z$  taken over all the computational points is used as the step size.

On the body boundary ( $X = 0$ ) the component of velocity normal to the body surface must vanish; i.e.,

$$u - b_z w - (b_\phi/b)v = 0. \quad (13)$$

This condition is supplemented with certain characteristic compatibility relations associated with the system (9). This approach was originally suggested by Kentzer<sup>12</sup> for unsteady flow problems and has been adapted, in different form, to steady supersonic flow in References 4 and 5. The method used in this work is given in detail in Reference 10 and is only briefly

reviewed. It is found that there are three independent characteristic relations which are admissible on  $X = 0$ . These can be written as a system of quasi-linear first order partial differential equations on  $X=0$  for advancing  $P = \ln(p)$ ,

$V_2 = u \frac{b_\phi}{b} + v$  and  $s$ . The resulting relations are:

$$\frac{\partial P}{\partial Z} = \left[ X \lambda \frac{\partial P}{\partial X} - \frac{1}{\beta_1} \{ \rho w [ \lambda + \frac{\partial A}{\partial X} - (a_7 w + a_4 v) ] + \hat{p} \} \right] \frac{1}{P} \quad (14a)$$

$$\text{where } \hat{p} = \frac{\rho v}{b} \frac{V_2}{2} + w \lambda \frac{e}{+1} + \vec{\xi} \cdot \frac{\partial \hat{G}}{\partial Y} \quad (14b)$$

$$+ p [\xi_2 (T_{g5} Y_z + T_{g6}) + \frac{1}{b} \xi_4 (T_{g5} Y_\phi + b_\phi/b)]$$

$$\lambda = \frac{a^2 (\beta - b_z)}{w^2 - a^2}, \quad \beta_1 = \sqrt{\left(\frac{w^2}{a^2}\right) v_\omega^2 - [1 + (\frac{b_\phi}{b})^2]}$$

$$a_7 = \frac{\partial b_z}{\partial Z} = b_{zz} - b_{z\phi} Y_z / Y_\phi$$

$$a_4 = \frac{\partial (b_\phi/b)}{\partial Z} = \frac{1}{b} [b_{z\phi} - \frac{b_z b_\phi}{b} - (b_{\phi\phi} - b_\phi^2/b) Y_z / Y_\phi]$$

$$\vec{\xi} = (\xi_1, \xi_2, \xi_3, \xi_4)$$

$$\xi_1 = w \lambda (2 - v_\omega^2 \kappa_1 / \rho), \quad \xi_2 = b_z - \lambda + w^2 \kappa_1 \lambda / \rho$$

$$\xi_3 = w u \kappa_1 \lambda / \rho - 1, \quad \xi_4 = w v \kappa_1 \lambda / \rho + b_\phi / b$$

$$\kappa_1 = \left(\frac{\partial \rho}{\partial h}\right)_p = 1 / \left(\frac{\partial h}{\partial \rho}\right)_p \quad (\kappa_1 = -\rho/h \text{ for a perfect gas})$$

$$T_{g5} = g_{YY} / g_Y, \quad T_{g6} = g_{ZY} / g_Y, \quad \hat{G} = GJ/r$$

$$v_\omega^2 = 1 + (b_\phi/b)^2 + b_z^2$$

$$\frac{\partial V_2}{\partial Z} = a_4 u + \hat{v} / \rho w \quad (15a)$$



where

$$\hat{v} = \bar{\eta} \cdot \frac{\partial \hat{G}}{\partial \bar{Y}} - \rho v w b_z / b - \frac{p}{b} (T_{g5} Y_\phi + b_\phi / b) \quad (15b)$$

$$\bar{\eta} = (\eta_1, \eta_2, \eta_3, \eta_4)$$

$$\eta_1 = V_2, \quad \eta_2 = 0, \quad \eta_3 = -b_\phi / b, \quad \eta_4 = -1$$

$$\frac{\partial s}{\partial Z} = -\frac{B}{W} \frac{\partial s}{\partial Y} \quad (16)$$

Equations (14) to (16) are advanced using a predictor-corrector method of the form (10) but with the X derivatives replaced by forward differences in both the predictor and corrector steps. This differencing scheme which is first order accurate can be made second order accurate using the procedure given in Reference 10. At the end of both the predictor and corrector steps, wall values of  $p, \rho, u, v, w$  are determined from  $P, V_2, s, (7), (8c)$  and (13) which can be manipulated to give the relations:

$$p = \exp(P); \quad q^2 = 2(H_0 - h)$$

$$\rho = (p / \exp(s))^{1/\gamma}$$

$$w = \sqrt{[1 + (b_\phi / b)^2] q^2 - V_2^2} / v_w \quad (17)$$

$$v = [V_2 - (b_\phi / b) b_z w] / [1 + (b_\phi / b)^2]$$

$$u = b_z w + (b_\phi / b) v$$

Alternative expressions for  $\hat{p}$  and  $\hat{v}$  of (14b) and (15b) which often give improved results are:

$$\hat{p} = \frac{\rho v}{b} V_2 + [b_z Y_z + \frac{1}{b} b_\phi Y_\phi + \frac{(Bw - Y_z)}{a} \lambda +] \frac{\partial p}{\partial Y} \quad (14c)$$

$$- \rho B (a_5 w + a_3 v)$$

$$+ \rho w \lambda \{ (T_{f6} - T_{g6}) w + \frac{v}{b} T_{f7} + \frac{w}{b} [Y_\phi \frac{\partial (v/w)}{\partial Y} + b_z] \}$$

where

$$a_5 = \frac{\partial b_z}{\partial Y} = b_{z\phi} / Y_\phi$$

$$a_3 = \frac{\partial(b_\phi/b)}{\partial Y} = [b_{\phi\phi}/b - (b_\phi/b)^2] / Y_\phi$$

$$T_{f6} = T_{g6} + \frac{f_{ZX} + Y f_{YZ}}{f_X} - \frac{(b_z - c_z)}{(c - b)}; \quad T_{f7} = \frac{Y f_{YX}}{f_X} - \frac{(b_\phi - c_\phi)}{(c - b)}$$

and

$$\hat{v} = \rho B(a_3 u - \frac{\partial v_2}{\partial Y}) - \frac{1}{b} Y \frac{\partial p}{\partial Y} - \frac{\rho v w}{b} b_z \quad (15c)$$

These equations are algebraically identical to (14b) and (15b). They produce slightly different numerical results because the X and Y differences involve different quantities.

Many body configurations of interest have sharp corners or edges such as those found on biconics and other segmented shapes. If the upstream body surface velocity normal to this edge is supersonic, either a shock wave or an expansion fan will be attached to this edge producing a discontinuity in surface flow variables. To handle this situation, an oblique shock or Prandtl-Meyer expansion is applied at the edge as is described in References 8 and 10. In the interior these discontinuities are captured using the dissipative and conservation properties of the interior point scheme.

At the bow shock, flow field properties, as well as the shock slope, are unknown. The correct boundary conditions are provided by the Rankine-Hugoniot conditions which relate the free stream properties, the shock slopes, and the properties behind the shock. An analysis of the characteristics associated with the system (9) indicates there is one admissible characteristic relation on  $X = 1$  (see Reference 10). This expression, when combined with the Rankine-Hugoniot relations, results in the following system of equations which are used to advance  $c$ ,  $c_z$  and  $c_\phi$ :

$$\frac{\partial c}{\partial Z} = c_z - (Y/Y_\phi) c_\phi$$

$$\frac{\partial c_\phi}{\partial Z} = Y_\phi \frac{\partial c}{\partial Y} - Y_z \frac{\partial c_\phi}{\partial Y} \quad (18)$$

$$\frac{\partial c}{\partial Z} = \frac{1}{C_1} \left\{ R_s - \frac{C_2}{c} \left[ \left( Y_\phi \frac{\partial c}{\partial Y} - Y_z \frac{\partial c_\phi}{\partial Y} \right) - \frac{c_\phi}{c} (c_z - Y_z c_\phi / Y_\phi) \right] \right\}$$

where

$$C_1 = \{ (v_s w_\infty - c_z V_{n_\infty}) A_1 - (p - p_\infty) [1 + (c_\phi/c)^2] \} / v_s^2$$

$$C_2 = \{ [v_s v_\infty - (c_\phi/c) V_{n_\infty}] A_1 + c_z (c_\phi/c) (p - p_\infty) \} / v_s^2$$

$$A_1 = [\beta_0 \rho_\infty V_{n_\infty} + \rho (v_s w_\infty - c_z V_{n_\infty})] A_0 + \beta_0 \rho_\infty (V_{n_\infty} - V_n)$$

$$A_0 = \frac{(V_{n_\infty} - V_n) [a^2 + V_n^2 + \kappa_1 (a^2/\rho) V_n (V_{n_\infty} - V_n)]}{V_{n_\infty} (a^2 - V_n^2)}$$

$$\beta_0 = \frac{1}{a} \sqrt{(w^2 - a^2) [1 + (c_\phi/c)^2] + [u - (c_\phi/c)v]^2}$$

$$\kappa_1 = \left( \frac{\partial \rho}{\partial h} \right)_p = 1 / \left( \frac{\partial h}{\partial p} \right)_p \quad (\kappa_1 = -\frac{\rho}{h} \text{ for a perfect gas})$$

$$R_s = \vec{\zeta} \cdot \left( \frac{\partial \hat{F}}{\partial X} + \frac{\partial \hat{G}}{\partial Y} + \hat{E} \right) - (A_1 - v_s \rho w) [v_\infty + (c_\phi/c) u_\infty] Y / (Y v_s)$$

$$\hat{F} = FJ/r; \quad \hat{E} = \frac{(\tilde{F} - \tilde{E})}{r} - \left[ \frac{\partial X}{\partial X} \tilde{z} + \frac{\partial Y}{\partial Y} \tilde{z} \right] \tilde{U} - \frac{\partial X}{\partial X} \tilde{r} \tilde{F} - \left[ \frac{\partial X}{\partial X} \tilde{\phi} + \frac{\partial Y}{\partial Y} \tilde{\phi} \right] (\tilde{G}/r)$$

$$\vec{\zeta} = (\zeta_1, \zeta_2, \zeta_3, \zeta_4)$$

$$\zeta_1 = [2 - (\kappa_1/\rho) V_n^2] \lambda_-, \quad \zeta_2 = [(u - (c_\phi/c)v) - \lambda_-] / w + \lambda_- \kappa_1 w / \rho$$

$$\zeta_3 = \lambda_- \kappa_1 u / \rho - 1, \quad \zeta_4 = c_\phi / c + \lambda_- \kappa_1 v / \rho$$

$$\lambda_- = -a^2 \{ \beta_0 w + [u - (c_\phi/c)v] \} / (w^2 - a^2)$$

$$V_n = (u - v c_\phi / c - w c_z) / v_s; \quad v_s^2 = 1 + \left( \frac{c_\phi}{c} \right)^2 + \frac{c^2}{z^2}$$

In the above, the quantity  $\vec{\zeta} \cdot \left( \frac{\partial \hat{F}}{\partial X} + \frac{\partial \hat{G}}{\partial Y} + \hat{E} \right)$  denotes the inner product of these vectors and  $V_{n_\infty}$  is the free stream velocity component normal to the

shock. Since  $C_1 > 0$ , the equations (15) - (17) can be used to advance  $c$ ,  $c_z$ , and  $c_\phi$  in a predictor-corrector method of the form (10) but with the  $X$  derivatives replaced by backward differences in both the predictor and corrector steps. With the local shock angles thus determined, the flow variables at  $X = 1$  follow from the Rankine-Hugoniot conditions and the known free-stream conditions. The resulting relations are:

$$p = \frac{1}{\gamma+1} \left[ p_\infty (1-\gamma) + 2 \rho_\infty V_{n_\infty}^2 \right] \quad (19)$$

$$\rho = \rho_\infty^2 V_{n_\infty}^2 / (\rho_\infty V_{n_\infty}^2 + p_\infty - p)$$

$$u = u_\infty + \left( \frac{V_{n_\infty}}{V_S} \right) \left( 1 - \frac{\rho_\infty}{\rho} \right), \quad w = w_\infty - (u - u_\infty) c_z, \quad v = v_\infty - (u - u_\infty) (c_\phi / c)$$

In the above,  $w_\infty, v_\infty, u_\infty$  are the free stream velocity components given by  $V_\infty \cos\beta \cos\alpha$ ,  $V_\infty (\cos\beta \sin\alpha \sin\phi - \sin\beta \cos\phi)$ , and  $-V_\infty (\cos\beta \sin\alpha \cos\phi + \sin\beta \sin\phi)$ , respectively.

### 2.3 FIN SURFACES

**2.3.1 THE THIN FIN APPROXIMATION AND IMPLEMENTATION.** The thin fin approximation is applicable to fins with surfaces that lie close to a constant  $\phi$  plane, say  $\phi = \phi_f$ , which is defined as the fin plane. The fin geometry is assumed to be represented by two surfaces, the upper and lower surfaces, each described independently by relations of the form

$$\phi = \phi_f + \sigma(r, z) \quad (20)$$

In the cross-section  $Z = \text{constant}$ , the actual fin surfaces will lie within the computational mesh as shown in Figure 2. The thin fin approximation assumes that  $\sigma$  is small and thus places the fin surfaces along the fin plane corresponding to  $Y = Y_f$  in each  $Z = \text{constant}$  plane. Although the fin is approximated by a zero thickness plane lying on  $\phi = \phi_f$ , the surface slopes are described to  $O(|\sigma|)$ . The fin surface is prescribed by specifying  $\theta(r, z), \nu(r, z), L(z)$  and the first derivatives of these quantities. Here  $\theta$  and  $\nu$  are the angles between the fin surface tangency plane and the fin planes in the  $r$  and  $z$  directions respectively, and the quantity  $L$  is the radial location of the fin edge. In terms of  $\theta, \nu$  the derivatives of  $\sigma$  correct to  $O(|\sigma|)$  are given by:

$$\begin{aligned} r\sigma_r &= \tan \theta, \quad r\sigma_z = \tan \nu, \\ r\sigma_{rr} &= \sec^2 \theta (\theta_r - \nu_r) - \sigma_r \end{aligned} \quad (21)$$

$$r\sigma_{zz} = \sec^2 \psi \sigma_z - r \tan^2 \psi, \quad r\sigma_{rz} = \sec^2 \theta (\theta_z - \sigma_z)$$

Within the restriction that  $|\sigma|$  be "small", the thin fin approximation can be applied to arbitrary fin geometries including surfaces with discontinuous slopes and fins with "small" deflections, camber, and variations in dihedral.

The numerical algorithm for treating fins by the thin fin approximation requires that the computational mesh be chosen so that each fin plane is coincident with a computational mesh plane,  $Y = Y_f$ . Two sets of computational points are carried on the  $Y = Y_f$  plane to describe the flow properties on the upper and lower surfaces as is illustrated in Figure 2. The upper surface of a fin features an outward normal that has a positive  $\bar{e}_\phi$  component, while the lower surface has a negative  $\bar{e}_\phi$  component associated with its outward normal. As the calculation is marched down the length of the body, fin surfaces are encountered on  $Y = Y_f$ . Thus a point at some  $X$  may at one axial location be an interior flow field point and in the next axial step move onto the fin. Here the interior point is split into two points corresponding to the upper and lower fin surfaces. The fin points thus created are referred to as leading edge points. For a fixed  $X$ , a pair of points which are on the fin at one axial step can in the next step move off the fin and become a single interior flow field point. Such a point will be referred to as a trailing edge point. The flow variables at leading and trailing edge points are determined from an appropriate local analysis which is described in the following subsections. The adjustment for the presence of a leading or trailing edge is made immediately after the completion of the step in which the edge is encountered. The values of the flow variables prior to the adjustment are termed upstream while the adjusted values are termed downstream. Note that the locations of leading and trailing edge points are within one  $\Delta Z$  of the physical edges of the wing.

**2.3.2 FIN SURFACE BOUNDARY CONDITIONS.** On a fin surface, the velocity component normal to the surface must vanish; i.e.,

$$v/r - \sigma_z w - \sigma_r u = 0. \quad (22)$$

The numerical methods used to advance the fin surface points are based on the appropriate characteristic compatibility relations associated with (9) which are derived in Appendix A. Both the upper and lower fin surfaces, although considered separately, are treated using the same techniques. For fin surface points not on the fin body junction ( $X=0$ ), the three compatibility relations listed below are used to advance  $s$ ,  $V_3 = u + r\sigma_r v$  and  $P = \ln p$  along the fin surface:

$$\frac{\partial s}{\partial Z} = -\frac{1}{w}(X_z w + X_r u + X_\phi v/r) \frac{\partial s}{\partial X} \quad (23)$$

$$\partial V_3 / \partial Z = v(\alpha_1 + \alpha_3) + \tilde{V}/\rho w \quad (24)$$

$$\text{where } \tilde{V} = (-V_3, 0, 1, r\sigma_r) \frac{\partial (\frac{\hat{F}}{\partial X})}{\partial X} + p \left[ \frac{\partial X_r}{\partial X} + r\sigma_r \frac{\partial (X_\phi/r)}{\partial X} \right],$$

$$\alpha_1 = r\sigma_{rz} - (\sigma_r + r\sigma_{rr})\alpha_0, \quad \alpha_0 = (\sigma_z X_\phi + X_z) / (X_r + r\sigma_r X_\phi)$$

$$\begin{aligned}
\frac{\partial p}{\partial Z} = & \lambda Y_{\xi} \left[ \frac{\partial p}{\partial Y} + \frac{\rho w (\sigma_z}{\beta} \frac{\partial w}{\partial Y} + \sigma_r \frac{\partial u}{\partial Y} - \frac{1}{r} \frac{\partial v}{\partial Y} \right] \\
& + (1/\beta) \left[ \rho w [u(\alpha_1 - \lambda) + w\alpha_2 + vV_3/(rw)]/r \right. \\
& - \hat{\eta} \frac{\partial \hat{F}}{\partial X} + (\rho w^2 \lambda + p\eta_2) \frac{\partial X_z}{\partial X} + (\rho w \lambda + p\eta_3) \frac{\partial X_r}{\partial X} \\
& \left. + (\rho w v \lambda + p\eta_4) \frac{\partial (X_{\phi}/r)}{\partial X} \right]
\end{aligned} \quad (25)$$

$$\text{where } \beta = \pm \left[ \frac{w^2}{a^2} \left( \frac{1}{r^2} + \sigma_r^2 + \sigma_z^2 \right) - \frac{1}{r^2} - \sigma_r^2 \right]^{1/2}$$

$$\lambda = \frac{a^2(\beta - \sigma_z)}{w^2 - a^2}, \quad Y_{\xi} = Y_{\phi} X_r / (X_r + \sigma_r X_{\phi})$$

$$\alpha_2 = r \sigma_{zz} - a_0(\sigma_z + r \sigma_{rz}), \quad \eta_1 = \lambda w (2 - \kappa |\bar{q}|^2),$$

$$\eta_2 = (w\kappa - 1)\lambda + \sigma_z, \quad \eta_3 = w\lambda\kappa + \sigma_r,$$

$$\eta_4 = wv\lambda\kappa - 1/r$$

$$\rho\kappa = (\partial\rho/\partial h) = -\frac{\rho}{p} \text{ for a perfect gas.}$$

The upper and lower signs in  $\beta$  are used on the upper and lower fin surfaces, respectively. The quantities  $\frac{\partial}{\partial Z}$  and  $\frac{\partial}{\partial X}$  in (23) (24), and (25) represent the

partial derivatives of quantities defined on the fin surface and thus are functions of  $Z$  and  $X$  only. Equations (23), (24), (25) follow from the compatibility equations derived in Appendix A without approximation. The thin fin assumption is applied by evaluating flow field variables and transformation quantities ( $X_r, X_z, X_{\phi}$ , etc.) at the fin plane rather than at the actual fin surface. Predictor-corrector differencing of the form of (10) is used to march the solution in  $Z$ . However, the  $Y$  derivatives are replaced by forward differences on the upper fin surface and the backward ones on the lower fin surface in both the predictor and corrector steps. At the end of each computational step, the quantities  $p, \rho, u, v, w$  are determined by simultaneously solving (7), (8c), (22) and the definition of  $V_3$ . This yields:

$$p = \exp(P) \quad (26a)$$

$$\rho = [p/\exp(s)]^{1/\gamma} \quad (26b)$$

$$w = \sqrt{\frac{2(H_0 - h)(1 + r^2 \sigma_r^2) - V_3^2}{r^2 \sigma_r^2 + r^2 \sigma_z^2 + 1}} \quad (26c)$$

$$v = \frac{(r \sigma_r) V_3 + r \sigma_z w}{1 + r^2 \sigma_r^2} \quad (26d)$$

$$u = V_3 - r \sigma_r v \quad (26e)$$

The fin body junction is assumed to be a sharp corner. At this corner both (13) and (22) are satisfied and thus flow is directed along the corner. This implies that entropy is constant along the corner except at compressive discontinuities in body or fin slope and at leading and trailing edges. Since (7) also holds, only one additional relation is needed to completely determine the flow variables along the junction. This is given by a characteristic compatibility condition. However, an ambiguity arises in the choice of an appropriate characteristic condition. Two possible equations are derived in Appendix A:

$$\begin{aligned} \frac{\partial p}{\partial Z} = & X_r \Lambda_1 \left[ \frac{\partial p}{\partial X} + \frac{\rho w}{\beta_1} \left( b \frac{\partial w}{\partial X} + \frac{b}{b} \frac{\partial v}{\partial X} - \frac{\partial u}{\partial X} \right) \right. \\ & + \frac{\rho w}{b \beta_1} \left\{ b Y_5 \Lambda_1 \left( \sigma_r \frac{\partial u}{\partial Y} + \sigma_z \frac{\partial w}{\partial Y} - \frac{1}{b} \frac{\partial v}{\partial Y} \right) \right. \\ & + w (\alpha_4 + \alpha_2 \Lambda_2) + u (\alpha_1 \Lambda_2 - \Lambda_1) + v [\alpha_5 \\ & \left. \left. - (V_2 - \Lambda_2 V_3 / b) / w \right] \right\} \end{aligned} \quad (27a)$$

where

$$\begin{aligned} \Lambda_1 = & a^2 (\sigma_z T - b_z R + \beta_1 R) / \Omega_1, \quad \Lambda_2 = (-\Omega_2 \\ & + a^2 \sigma_z \beta_1) / \Omega_1, \quad \beta_1 = \{ (\Omega_1 \Omega_3 - \Omega_2^2) / [a^2 (w^2 - a^2) R] \}^{1/2}, \\ R = & \sigma_z^2 + \sigma_r^2 + 1/b^2, \quad S = b_z^2 + 1 + b_\phi^2/b^2, \quad T = \sigma_z b_z \\ & - \sigma_r - b_\phi/b^2, \quad \Omega_1 = (w^2 - a^2) R + a^2 \sigma_z^2, \quad \Omega_2 = (w^2 \\ & - a^2) T + a^2 b_z \sigma_z, \quad \Omega_3 = (w^2 - a^2) S + a^2 b_z^2, \\ \alpha_4 = & b(b_{zz} + \alpha_3 b_{z\phi}), \quad \alpha_3 = (\sigma_r b_z + \sigma_z) / (1 - \sigma_r b_\phi), \\ \alpha_5 = & b_\phi z - b_\phi b_z / b + \alpha_3 (b b_{\phi\phi} - b_\phi^2) / b^2, \end{aligned}$$

and

$$\begin{aligned}
 \frac{\partial p}{\partial Z} = & \gamma \Lambda_3 \left[ \frac{\partial p}{\partial Y} + \frac{\rho w}{\beta_2} \left( \sigma_z \frac{\partial w}{\partial Y} + \sigma_r \frac{\partial u}{\partial Y} - \frac{1}{b} \frac{\partial v}{\partial Y} \right) \right] \\
 & + \frac{\rho w}{b\beta_2} \left[ \frac{bX}{r} \Lambda_3 \left( b \frac{\partial w}{\partial X} - \frac{\partial u}{\partial X} + \frac{b}{b} \frac{\partial v}{\partial X} \right) \right. \\
 & + w(\alpha_4 \Lambda_4 + \alpha_2) + u(\alpha_1 - \Lambda_3) + v[\Lambda_4 \alpha_5 \\
 & \left. - (\Lambda_4 V_2 - V_3/b)/w \right] \quad (27b)
 \end{aligned}$$

where  $\Lambda_3 = a^2 [b_z T - \sigma_z S + S\beta_2]/\Omega_3$ ,  $\Lambda_4 = (-\Omega_2 + a^2 b_z \beta_2)/\Omega_3$ ,  $\beta_2 = \pm \beta_1 (R/S)^{1/2}$ . The upper and lower

signs are used for the upper and lower surface junctions, respectively. In (27),  $\frac{\partial}{\partial X}$  and  $\frac{\partial}{\partial Z}$  represent the derivatives of quantities defined on the fin

surface as a function of X and Z only. Equation (27a) is based on the bicharacteristic lying along the wing surface while (27b) corresponds to the bicharacteristic lying along the body surface. Both equations appear to produce similar results except when large pressure gradients occur in the vicinity of the junction (i.e., close to a leading edge or surface discontinuities). Computational experience seems to indicate that the more robust relation corresponds to the equation lying along the direction with the smallest pressure gradients. Both of the above equations follow from the compatibility equations derived without approximation. The thin fin assumption is introduced by evaluating the flow field variables and transformation quantities at the fin plane rather than at the actual fin surface.

At the completion of the predictor-corrector sequence, the pressure along the corner has been determined using equations (27a) or (27b) and the entropy is unchanged from the value at the previous step. The quantity  $\rho$  is obtained from (8c), the enthalpy from (8a) and the magnitude of the velocity from (7). The velocity components u, v, w are resolved by requiring that the velocity vector be coincident with the corner direction which is given by  $\vec{n}_f \times \vec{n}_b$ , where  $\vec{n}_f$  and  $\vec{n}_b$  are the normal vectors to the fin and body surface respectively, as shown in Figure 3. Hence,

$$u = \frac{(b_z + \sigma_z b_\phi)}{|\vec{n}_c|} |\vec{q}|; \quad v = \frac{b(\sigma_r b_z + \sigma_z)}{|\vec{n}_c|} |\vec{q}|; \quad w = \frac{(1 - \sigma_z b_\phi)}{|\vec{n}_c|} |\vec{q}| \quad (28)$$

where  $\vec{n}_c = (b_z + \sigma_z b_\phi)\vec{e}_r + b(\sigma_r b_z + \sigma_z)\vec{e}_\phi + (1 - \sigma_r b_\phi)\vec{e}_z$



## 2.4 FIN EDGES AND SURFACE SLOPE DISCONTINUITIES

2.4.1 LEADING EDGES. A leading edge point occurs when an interior point moves onto the fin surface. This point must then be split into two points in order to allow both the upper and lower fin surfaces to be described. Several different strategies are available for treating leading edge points. The simplest approach is to switch from the interior point advancement scheme (9) to the fin surface scheme (23), (24), (25) at the leading edge. This is referred to as option 0. To accomplish this, the computation is carried out through the predictor step using the interior point advancement scheme. At the end of the predictor step the  $z$  value is advanced, the fin geometry is updated, and the leading edge is detected. The corrector step at the leading edge point is completed using the fin surface compatibility equations. Thus for a leading edge occurring in step  $k$  at  $(X_n, Y_m)$ :

$$\begin{aligned} p_{n,m}^k &= (p_{n,m}^{k-1} + p_{n,m}^* + \left. \frac{dp}{dz} \right|_{n,m} \Delta Z)/2 \\ v_{3,n,m}^k &= (v_{3,n,m}^{k-1} + v_{3,n,m}^* + \left. \frac{dv_3}{dz} \right|_{n,m} \Delta Z)/2 \\ s_{n,m}^k &= (s_{n,m}^{k-1} + s_{n,m}^* + \left. \frac{ds}{dz} \right|_{n,m} \Delta Z)/2 \end{aligned} \quad (29)$$

Here  $P^*, V_3^*$  and  $s^*$  are the values at the end of the predictor sequence. To evaluate the above requires that  $P^*, V_3^*, s^*$  and  $p^{k-1}, v_3^{k-1}, s^{k-1}$  be constructed. The quantities  $P^*, P, s$  and  $s^*$  follow directly from calculated  $p^*, p$  and  $\rho$  values. To form  $V_3 = u + (r\sigma_r)v$  and  $V_3^* = u^* + (r\sigma_r)v^*$  the value of  $(r\sigma_r)$  at the leading edge point is used. Leading edges at the body fin junction are treated in a similar fashion, but in this case only the pressure is advanced.

The leading edge option 0 represents a formal discretization of the various applicable equations without recourse to additional modeling at the leading edge. In principle, for this option to be successful, sufficiently fine grid and step size must be used to allow the solution to "capture" the effects associated with the presence of the fin edge. In practice, this option gives poor results or fails altogether when the flow features shock or expansion waves which produce large jumps in the vicinity of the edge.

An alternative approach is to apply locally an analysis which models the flow very near to the leading edge. This is designated as option 1. The justification for this option is that in most calculations, for reasons of computational efficiency, the mesh spacing in the vicinity of the edge is not sufficiently fine for option 0 to yield satisfactory results. The computational algorithm proceeds by completing the step in which a leading edge is encountered without taking the fin surface into account. The resulting flow properties are then taken as the conditions immediately upstream of the leading edge. An appropriate local analysis is then used to determine the flow quantities immediately downstream of the edge for both the upper and lower fin surfaces. The downstream flow quantities are then assigned to the leading edge points on the appropriate fin surface. The fin surface variables,  $P, V_3, s$  are then

advanced from the downstream values using the procedures described in Section 2.3.

The velocity vectors used to characterize the local flow at the leading edge are shown in Figure 3 where  $\vec{n}_f$  is the fin surface normal and  $\vec{n}_-$  is the normal to the plane defined by the upstream velocity vector  $\vec{q}$  and leading edge tangent vector  $\vec{t}$ . These vectors are defined by:

$$\begin{aligned}\vec{t} &= L_z \vec{e}_r + \vec{e}_z \\ \vec{n}_f &= -r \sigma_r \vec{e}_r + \vec{e}_\phi - r \sigma_z \vec{e}_z \\ \vec{n}_- &= v \vec{e}_r + (L_z w - u) \vec{e}_\phi - L_z v \vec{e}_z\end{aligned}\quad (30)$$

Depending on the orientations of  $\vec{n}_f$ ,  $\vec{n}_-$  and  $\vec{q}$ , the local analysis introduces an appropriate expansion or compression turn of  $\vec{q}$  from the plane normal to  $\vec{n}_-$  into the plane normal to  $\vec{n}_f$ . The specific turning procedure, which strongly depends on  $M_n$  (the Mach number of the upstream velocity component normal to the edge) is described in Section 2.4.4. The local analysis is exact if the turn on both sides of the wing can be accomplished either by a Prandtl-Meyer expansion or an oblique shock attached to the leading edge. In other cases, the concept of the exact local analysis breaks down and approximate or heuristic local analysis procedures are used as outlined in Section 2.4.4.

In cases when Option 1 is used and an attached shock does not exist at the leading edge, it has been found necessary to specify the downstream streamline direction. Figure 4 illustrates the influence of changes in streamline direction on the calculated surface pressures. As the streamline direction is turned outward, the pressure gradient downstream of the leading edge becomes increasingly negative. In the current method the streamline direction is set such that  $\tan(u/w) = .09911$ .

At the body fin junction option 1 is implemented by rotating the leading edge flow velocity vector within the tangency plane until it is in the corner direction,  $\vec{n}_c$ , which is given by (28). The required turning angle is:

$$\delta = \mp \sin^{-1}[(\vec{q} \cdot \vec{n}_f) / (|\vec{q}| |\vec{n}_f|)] \quad (31)$$

The - and + sign apply to the upper and lower surface respectively. An expansion occurs if  $\delta < 0$  and a compression if  $\delta > 0$ . The turning procedures described in Section 2.4.4 are used to determine the downstream values of  $p$ ,  $\rho$ , and  $q$ . It is possible for a body slope discontinuity to occur at the same axial station as a body-fin junction leading edge. In this case the body discontinuity is treated first with the presence of the fin neglected, using the procedures described in Reference 10. The body-fin junction leading edge treatment described above is then applied. In some cases the turning angle predicted by (31) becomes excessive, producing an unrealistically large pressure jump and possibly subsonic flow. Since viscous effects are likely to be important in these regions, the computational algorithm allows a reduction of the turning angle calculated from (31). For this purpose a multiplying factor,  $C_T$ , is introduced, the value of which is user-selected and is  $\leq 1$ .

If  $M_n$  is significantly less than unity, the jump conditions assigned by option 1 often do not give satisfactory results. This is particularly true on the expansion surfaces where the local analysis produces extremely low pressures. The condition  $M_n < 1$  occurs on highly swept wings which feature leeside separation and a large leeside vortex. This vortex generates a suction on the upper wing surface which increases the wing lift. Under these circumstances, the streamlines on the upper and the lower wing surfaces are directed outward at locations near the edges. The conditions at the leading edge are thus strongly influenced by the flow on the fin surface. To handle this situation, option 2 is introduced. When an interior point  $(X_n, Y_m)$  moves onto the fin, the leading edge pressure and density is determined by averaging values at  $(X_{n-1}, Y_m)$  and  $(X_n, Y_m)$ . Using (7) the magnitude of the velocity vector at the leading edge is determined and this vector is assumed to be parallel to the fin edge. The resulting expressions for the properties at a leading edge point  $(X_n, Y_m)$  are:

$$\begin{aligned}
 P_{n,m} &= (P_{n-1,m} + P_{n,m})/2 \\
 \rho_{n,m} &= (\rho_{n-1,m} + \rho_{n,m})/2 \\
 q &= \sqrt{2(H_0 - h)} \\
 u_{n,m} &= q L_z / (1 + L_z^{2/2}) \\
 v_{n,m} &= 0 \\
 w_{n,m} &= q / (1 + L_z^{2/2})
 \end{aligned} \tag{32}$$

**2.4.2 TRAILING EDGES.** At a trailing edge the two points on  $Y=Y_f$  representing the upper and lower fin surfaces, are coalesced into a single interior flow field point. A local analysis is used to determine the flow downstream of the trailing edge. The computational algorithm proceeds by completing the step in which a trailing edge is encountered without taking the fin edge into account. The resulting flow properties on the upper and lower fin surfaces are the upstream values and represent the flow properties on the two fin surfaces immediately upstream of the trailing edge. The local analysis uses these two sets of flow properties in conjunction with the local fin geometry to determine the value of the flow immediately downstream of the trailing edge.

The trailing edge local analysis is dependent on the Mach number normal to the trailing edge. If the flow component normal to the trailing edge on both surfaces is sufficiently supersonic, the streamlines from the upper and lower sides of the fin will turn onto a slip surface with normal  $\bar{s}$  (see Figure 3) by means of a system of oblique shocks and/or expansions which are attached to the trailing edge. The orientation of the slip plane onto which the streamlines are turned is such that the final pressures on both sides of the slip surface will be the same. Reference 13 describes an iterative procedure for determining the plane orientation. Unfortunately this scheme is cumbersome to apply and convergence cannot be guaranteed. Thus, this procedure has been discarded in favor of a simpler method that turns both of the surface streamlines onto the fin plane (i.e.,  $\bar{s} = \bar{e}_\phi$ ). The coalesced property values for  $p, \rho, u, v$

are then determined by averaging the results on the upper and lower surface streamlines. The velocity component  $w$  is solved for from (7) which ensures that the coalesced trailing edge point has the correct total enthalpy.

If the flow components normal to the trailing edge on either wing surface are subsonic, a different algorithm is applied. At a trailing edge point  $(X_n, Y_m)$ , flow properties are assigned to be those at  $(X_{n+1}, Y_m)$ , unless this point is a fin point. In that case properties at  $(X_{n-1}, Y_m)$  are used. If both of these points are on the fin, the upper and lower surface properties are set to the average values at points  $(X_n, Y_{m+1})$  and  $(X_n, Y_{m-1})$ .

At trailing edge points located on the body-fin junction the flow is turned within the body tangency plane using shocks or expansions until it is directed along the fin plane with normal  $\vec{s} = \vec{e}_\phi$ . The required turning angle is:

$$\delta = \cos^{-1} \frac{ub_z + w}{[1 + b_z^2]^{1/2} |\vec{q}|} \quad (33)$$

On an upper fin surface a compression is required if  $v < 0$  and an expansion if  $v > 0$ . The reverse sign convention applies on lower surfaces. The resulting values of  $p$  and  $\rho$  are determined by averaging the downstream properties on the upper and lower surfaces. Since  $\vec{q} \cdot \vec{e}_\phi = 0$ ,  $v = 0$  and  $u$  and  $w$  components are solved for by satisfying the total enthalpy condition (7) and the body boundary condition (13). This yields:

$$w = \left[ \frac{2(H_o - h)}{(1 + b_z^2)} \right]^{1/2} \quad (34)$$

$$u = b_z w$$

**2.4.3 SURFACE SLOPE DISCONTINUITIES.** Fin surfaces of design interest often contain slope discontinuities. Particularly when the surface velocity component normal to the discontinuity is supersonic, it is advantageous to apply a local analysis. This procedure turns the flow across the discontinuity by means of an oblique shock wave or expansion. The computational algorithm for handling fin surface discontinuities is analogous to that developed for body discontinuities in Reference 10. The scheme proceeds by completing the step in which the slope discontinuity is detected without taking into account the presence of the discontinuity. The resulting values at the end of this step are the upstream properties which in conjunction with the local fin geometry are used via the local analysis to determine downstream conditions.

A fin surface slope discontinuity is defined to occur if the following inequality is satisfied:

$$\left| |v_z^k - v_z^{k-1}| - \Delta Z \max(|v_z^k|, |v_z^{k-1}|) \right| + \left| |e_z^k - e_z^{k-1}| - \Delta Z \max(|e_z^k|, |e_z^{k-1}|) \right| \geq 2(10^{-6})$$

$$\text{where} \quad v_z^k = v_z^k - \frac{X_z v_r^k}{X_r} \quad e_z^k = e_z^k - \frac{X_z e_r^k}{X_r} \quad (35)$$

The upstream flow properties and the vectors normal to the fin surface upstream ( $\vec{n}_f^-$ ) and downstream ( $\vec{n}_f^+$ ) of the surface slope discontinuity form the necessary inputs for the turning procedure outlined in the following section. The vectors  $\vec{n}_f^-$  and  $\vec{n}_f^+$  are illustrated in Figure 3.

**2.4.4 EXPANSION AND COMPRESSION TURNS.** As indicated in Sections 2.4.1 to 2.4.3, the treatment of leading edges, trailing edges and surface slope discontinuities involves turning the flow by either a compression or expansion. This section provides the analysis used in implementing these turns and constructing the velocity downstream of the turn.

The parameters needed for calculating a compression or expansion turn are:  $\vec{n}_-$ ,  $\vec{n}_+$ ,  $p_-$ ,  $p_+$  and  $q_-$ . Here the minus and plus subscripts refer to the quantities upstream and downstream of the turns respectively. The vectors  $\vec{n}_-$  and  $\vec{n}_+$ , which are involved in this analysis, are illustrated in Figure 5. In the case of a leading edge, the  $\vec{n}_-$  vector used in this section corresponds to the  $\vec{n}_-$  vector defined in Section 2.4.1 while the  $\vec{n}_+$  vector corresponds to  $\vec{n}_f$ . Similarly, at the trailing edge  $\vec{n}_-$  corresponds to  $\vec{n}_f$  and  $\vec{n}_+$  to  $\vec{s}$  while at surface slope discontinuities  $\vec{n}_-$  corresponds to  $\vec{n}_f^-$  and  $\vec{n}_+$  to  $\vec{n}_f^+$ . Using this information the following turn parameters are calculated:

$$\begin{aligned} \delta &= \cos^{-1} \left( \frac{\vec{n}_- \cdot \vec{n}_+}{|\vec{n}_-| |\vec{n}_+|} \right) \\ \vec{r} &= \vec{n}_- \times \vec{n}_+ \\ \vec{s}_- &= \vec{n}_- \times \vec{r} \\ q_{n_-} &= \frac{\vec{q}_- \cdot \vec{s}_-}{|\vec{s}_-|} \\ q_r &= \frac{\vec{q}_- \cdot \vec{r}}{|\vec{r}|} \\ M_n &= \frac{q_n}{a} \end{aligned} \quad (36)$$

Here  $\delta$  is the turning angle,  $q_r$  is the upstream velocity component tangent to the edge of the discontinuity and  $q_n$  is the upstream velocity component normal to the edge. The vectors  $\vec{r}$  and  $\vec{s}_-$  are illustrated in

Figure 5. To facilitate consideration of both upper and lower fin surfaces, the parameter  $\beta$  is introduced which has a value of +1 and -1 on the upper and lower surfaces respectively. A turn is an expansion if  $\beta q_n < 0$  and a compression if  $\beta q_n > 0$ .

For an expansion turn the Prandtl-Meyer relations are applied if  $M_n \geq \sqrt{1.05}$ . These are given, in differential form, by:

$$\frac{dp}{d\alpha} = \frac{-\rho q_n^2}{\sqrt{\frac{q_n^2}{a^2} - 1}} \quad (37)$$

$$\frac{dp}{d\alpha} = \frac{1}{a^2} \frac{dp}{d\alpha}$$

$$q_n^2 = 2(H_0 - h) - q_r^2$$

Integration of (37) from  $\alpha = 0$  where  $q_n = q_n$ ,  $p = p_-$ ,  $\rho = \rho_-$  to  $\alpha = \delta$ , using the second order improved Euler method, gives  $p_+$ ,  $\rho_+$ ,  $q_n+$ . If  $0 < M_n < \sqrt{1.05}$  the flow is isentropically expanded to  $M_n = \sqrt{1.05}$  using the relations:

$$\frac{p^*}{p_-} = \left[ \frac{1 + \frac{(\gamma-1)M^2}{2}}{1 + \frac{(\gamma-1)M^2}{2}} \right]^{\frac{\gamma}{(\gamma-1)}}$$

$$\frac{\rho^*}{\rho_-} = \left( \frac{p^*}{p_-} \right)^{1/\gamma} \quad (38)$$

$$q^* = M_2 \left[ \frac{\gamma p^*}{\rho^*} \right]^{1/2}$$

where

$$M_1 = M_n \text{ and } M_2 = \sqrt{1.05}.$$

Equations (37) are then integrated using  $p^*$ ,  $\rho^*$  and  $q^*$  as the initial conditions. The choice of  $M_n = \sqrt{1.05}$  as the lower bound for the direct application of the Prandtl-Meyer relations is not crucial and any number slightly greater than unity, which avoids special treatment of the improper integral when  $M_n = 1$ , would be satisfactory.

A compression turn occurs if  $\beta q_n \geq 0$ . In these cases several possible turning strategies are considered. The domain of application of each strategy, as a function of normal Mach number,  $M_n$ , and turning angle,  $\delta$ , is illustrated in Figure 6. The oblique shock relations are used if there exists an oblique shock solution with supersonic downstream flow. Such a solution is permitted if  $M_n > 1$  and  $\delta < \delta^*$ , where:

$$\delta^* = \tan^{-1} \left[ \frac{M_n^2 \sin 2\sigma^* - 2 \cot \sigma^*}{2 + M_n^2 (\gamma + \cos 2\sigma^*)} \right] \quad (39)$$

$$\sigma^* = \sin^{-1} \left[ \frac{(\gamma + 1) M_n^2 - 3 + \gamma + \sqrt{C}}{4\gamma M_n^2} \right]^{1/2}$$

$$C = (\gamma + 1) \left[ (\gamma + 1) M_\infty^4 - 2(3 - \gamma) M_\infty^2 + \gamma + 9 \right].$$

If an oblique shock solution exists, the shock angle is determined by solving the cubic relation:

$$x^3 + c_1 x^2 + c_2 x + c_3 = 0$$

$$c_1 = -(1 + 2/M_n^2) - \gamma \sin^2 \theta \quad (40)$$

$$c_2 = (2M_n^2 + 1)/M_n^4 + [(\gamma + 1)^2/4 + (\gamma - 1)/M_n^2] \sin^2 \theta$$

$$c_3 = \cos^2 \theta / M_n^4$$

for the middle root. Here  $x$  is the sine-squared of the shock angle. With the shock angle determined, the Rankine-Hugoniot relations can be applied to the calculated conditions downstream of the shock:

$$\frac{p_+}{p_-} = [2\gamma M_n^2 x - (\gamma - 1)] / (\gamma + 1)$$

$$\frac{\rho_+}{\rho_-} = (\gamma + 1) M_n^2 x / [(\gamma - 1) M_n^2 x + 2] \quad (41)$$

$$\frac{q_+}{q_-} = \sqrt{\frac{1 - 4(M_n^2 x - 1)(\gamma M_n^2 x + 1)}{2\gamma(\gamma + 1) M_n^2 x}}$$

If  $M_n > 1$  and an oblique shock is not permitted, the downstream flow field conditions are determined using an empirical procedure which was developed using the data of Reference 14. An effective shock angle is estimated using the following relation:

$$\sigma_{\text{eff}} = \frac{\pi}{2} - \lambda \left[ \frac{\pi}{2} - \sigma^* \right] \quad (42)$$

$$\lambda = \text{Max} [0, \text{Min}[1.94 - .65 \left(\frac{\delta}{\delta^*}\right), 3.4 - 1.405 \left(\frac{\delta}{\delta^*}\right)]]$$

When  $\delta/\delta^* = 2.42$ , the above equation predicts a normal shock. For further increases in  $\delta/\delta^*$ , the subsonic flow behind the shock is isentropically compressed from  $M_s$ , the Mach number behind the shock, to a final Mach number of  $M_f$ . The quantity  $M_f$  is determined from the following equation:

$$M_f = \text{Max} [M_s[1 - \psi + (.13)\sin(\pi\psi)], 0.] \quad (43)$$

$$\psi = \frac{(\delta - 2.42\delta^*)}{\text{Max} [.314, \text{Min} (.855, 1.438 - .815M_n)]}$$

Downstream conditions are then predicted by applying (38) with  $M_1 = M_s$  and  $M_2 = M_f$ . When  $M_n < 1$ , a shock is not associated with a compression turn and downstream conditions are predicted by isentropically compressing the normal flow component to  $M_f$ .

The condition  $M_n < 0$  can occur on either an expansion or compression turn and indicates that the velocity vector does not cross the edge of the discontinuity. This situation is treated by isentropically stagnating the flow component normal to the leading edge using (38) with  $M_1 = M_n$  and  $M_2 = 0$ . At the completion of this procedure,  $q_{n+} = 0$  and the velocity vector is directed along the edge of the discontinuity.

At the completion of the expansion or compression turning procedures,  $p_+$ ,  $\rho_+$ ,  $q_{n+}$  have been determined and  $q_\tau$  is unchanged. The downstream velocity vector, can be constructed from:

$$\vec{q}_+ = q_\tau \vec{\tau} + \beta q_{n+} \frac{\vec{s}_+}{|\vec{s}_+|} \quad (44)$$

where

$$\vec{s}_+ = \vec{n}_+ \times \vec{\tau}$$

Here the upper sign is used for a compression turn and the lower for an expansion turn.

## 2.5 TREATMENT OF INLETS

Provisions are included in the computer program for considering inlets which are attached to the missile body. The inlet may have an arbitrary shape provided that the inlet cowling and the missile body together can be represented by  $r = b(\phi, z)$ , where  $b(\phi, z)$  is single-valued in  $\phi$  for each  $z$ . Also the cowling lip must be sharp and must lie in a plane perpendicular to the body axis.



The presence of an inlet is checked at each  $\phi$  plane, at every step. An inlet is defined to occur on plane  $m$  at step  $k$  if:

$$\left| \left| b_m^k - b_m^{k-1} \right| - \max(|b_{z_m}^k|, |b_{z_m}^{k-1}|) \Delta z \right| > .01 \quad (45)$$

where

$$b_{z_m}^k = b_m^k - \frac{Y}{z_m} b_m^k$$

Here  $b$  is the body radius,  $b_z, b_\phi$  are the derivatives of  $b$  with respect to  $z$  and  $\phi$ . The computational step in which an inlet is detected is completed using the body radius from the previous step,  $b_m^{k-1}$ . The flow field at a radius of less than  $b_m^k$  is then excluded from the computation by rezoning which places the body surface of plane  $m$  at a radius of  $b_m^k$  and leaves the shock location unaltered. The same number of radial points are retained along plane  $m$  and their distribution is determined by  $f(X, Y, Z)$  of (3). The flow properties at the new grid point locations are determined from old values by linear interpolation. At the wall the interpolated properties are interpreted as the conditions immediately upstream of the inlet lip. The conditions immediately downstream of the lip are obtained using the local analysis of Section 2.4.4. The velocity vector is turned through the angle:

$$\delta = \cos^{-1} \left[ \frac{\vec{n}_- \cdot \vec{n}_f}{|\vec{n}_-| |\vec{n}_f|} \right] \quad (46)$$

Here  $\vec{n}_- = \vec{e}_r - \frac{b_\phi}{b} \vec{e}_\phi + \frac{1}{w} \left( \frac{v b_\phi}{b} - u \right) \vec{e}_z$  and is perpendicular to the plane containing the lip tangency vector and the velocity vector  $\vec{q}$ . To accomplish this turn the upstream velocity vector is broken into components normal,  $q_n$ , and parallel  $q_\tau$ , to the lip using  $\vec{n}_-$  and  $\vec{n}_b$ , the inlet surface normals. The resultant relation are:

$$\begin{aligned} \vec{\tau} &= \vec{n}_- \times \vec{n}_b \\ q_n &= \frac{\vec{q} \cdot (\vec{n}_- \times \vec{\tau})}{|\vec{n}_- \times \vec{\tau}|} \\ q_\tau &= \frac{\vec{\tau} \cdot \vec{q}}{|\vec{\tau}|} \end{aligned} \quad (47)$$

The properties  $p_-, \rho_-, q_n$  are known and serve as the initial conditions to the turn which is accomplished using the procedure described in Section 2.4.4. A compression turn is required if  $\vec{q} \cdot \vec{n}_b < 0$  and an expansion if  $\vec{q} \cdot \vec{n}_b > 0$ . The turning procedure produces  $p_+, \rho_+, q_{n+}$  while leaving  $q_\tau$  unchanged. The final velocity vector can then be constructed from

$$q = q_{\tau} \frac{\vec{\tau}}{|\vec{\tau}|} + \left( \frac{\vec{n} \times \vec{\tau}}{|\vec{n}_b \times \vec{\tau}|} \right) q_{n_-} \quad (48)$$

in which the plus sign is used for a compression turn and minus sign for expansion.

### SECTION 3

#### SPECIAL PROCEDURES

The presence of fin surfaces in the interior of the computational domain requires the introduction of some special differencing procedures. In addition, physical considerations have motivated other adjustments to the differencing used at both fin and interior points located next to the fin edge.

3.1 ALTERATION OF X DIFFERENCING FOR FIN AND INTERIOR POINTS ADJACENT TO THE FIN TIP. The types of points under consideration in this subsection are A, B, C, of Figure 2. Selection of appropriate schemes for advancing these points depends on the Mach number normal to the leading edge and the applied leading edge treatment. Several differencing strategies are available.

Option 0 for the fin points such as A, B and interior points such as C is similar to the computational algorithm applied elsewhere in the flow field. Fin points A, B are advanced using the usual fin surface point algorithm. The MacCormack scheme for advancing point C must be modified since there are two adjacent sets of flow values (i.e., points A and B) corresponding to the upper and lower fin surfaces. Point C is advanced in two separate calculations using first the lower fin surface values at A and then the upper fin surface values at B. The resulting two conservation vectors are then averaged.

A second strategy, option 1, advances the fin edge points A, B without using the information at point C, and interior points such as C without recourse to the information at points A, B. To advance point C using this option, X differences are taken in the direction away from the fin in both the predictor and corrector steps. Using one-sided X differences to advance points A, B has been found to produce unsatisfactory results. Instead, X derivatives calculated from flow properties at A and C or B and C are set to zero. The computational algorithm has been constructed with sufficient generality to allow C to be advanced using A, B, or A and B.

The choice of which option to use in calculating X differences for fin edge points and adjacent interior points, is primarily dictated by the treatment employed at the leading edge. If the leading edge is treated without recourse to a local analysis (i.e., leading edge option 0), points A, B, C are advanced using X differencing option 0 which allows points off the fin to be influenced by points on the fin. When a local analysis is used (i.e., leading edge option 1), the X differencing option 1 is recommended. The rationale for selecting this combination of options can be seen by considering the leading edge with an attached shock wave. Here the Mach number normal to the leading edge is supersonic and the interior points on the fin plane, such as C, should not be influenced by the presence of the fin. The use of option 1 practically eliminates all of the upstream influence of the fin. The X derivatives, calculated on the fin surface, should reflect local surface variations. If information at point C is used to advance A, B, the X derivatives will reflect property variations across the shock, and the calculated values will be greatly

in excess of the local values. The use of option 1 essentially assumes that the flow properties at the tip are equal to those at the adjacent fin point.

In the case of a subsonic leading edge, a more complicated choice is necessary. Here compression surfaces are advanced using both X differencing and leading edge options of 0, while the expansion surfaces are treated with X differencing and leading edge options of 1 and 2. The interior point adjacent to the fin tip, C, is advanced using X differencing option 0.

**3.2 SUPPRESSION OF Y DERIVATIVES NEAR THE LEADING EDGE.** Figure 7 illustrates the calculated surface pressures on a fin in uniform flow. The calculated results should exhibit a constant pressure downstream of the leading edge, but in fact overshoot the leading edge value. The excessive pressure values aft of the leading edge are a consequence of the numerical procedure and the error becomes more severe as the magnitude of the pressure jump at the leading edge increases. Such inaccuracies at the leading edge can have a strong influence on the total vehicle aerodynamics. The calculated pressure overshoot at the leading edge may be suppressed by damping the Y derivatives which occur in (25) and (27) that advance the fin and corner pressures. Such a procedure, described below, is automatically implemented on leading edges which feature a pressure rise.

Following the occurrence of a leading edge the Y derivatives are set to 0 for one step and damped for an additional  $K_s$  steps. The damping is accomplished by multiplying the Y derivatives by a factor  $0 \leq D_c \leq 1$ . A new  $K_s$  is calculated for each leading edge point encountered. The value of  $K_s$  for a leading edge point occurring at  $(X_n, Y_m, Z_k)$  is based on the magnitude of

$$\frac{\Delta p}{\Delta \phi} = \frac{P_{n,m+1}^{k+1} - P_{n,m}^{k+1}}{(\phi_{n,m+1}^{k+1} - \phi_{n,m}^{k+1})}$$

Here the top and bottom signs apply to the upper and lower fin surfaces respectively, while the  $k + 1$  superscript indicates that this quantity is evaluated one step following the occurrence of the leading edge. The algorithm for selecting  $K_s$  is:

$$K_s = \left\lceil \left[ \text{Min} \left( \frac{\Delta p}{\Delta \phi} .5655, 4.28 + .08 \frac{\Delta p}{\Delta \phi} \right) \text{Max} \left( 1.33 - .2 M_n, .7 \right) \right] \right\rceil \quad (49)$$

where  $\lceil x \rceil$  = largest integer not exceeding x.

The Damping factor  $D_c$  is calculated from:

$$D_c = \begin{cases} 0 & k \leq (K_s - 4) \\ 1 - \frac{(K_s - k)}{4} & (K_s - 4) < k \leq K_s \end{cases} \quad (50)$$

Here  $k$  is the number of steps following the occurrence of the leading edge.

At the body fin junction, the algorithm for predicting  $K_s$  at point  $(X_1, Y_m)$  is given by

$$K_s = \left[ .35 \left( \frac{\Delta p}{\Delta \phi} \right)^k \right] \quad (51)$$

If  $k < K_s$  the corner relations for advancing pressure are not used. Instead, the velocity vector is isentropically turned, first within the body tangency plane and then within the fin tangency plane, until it is parallel to the corner.

**3.3 APPLICATION OF SMOOTHING TO INTERIOR, BODY, AND FIN POINTS.** In computations featuring body separation, and on highly swept wings with subsonic normal Mach numbers at the leading edge, large vortex structures develop in the flow field. In such circumstances it is often necessary to smooth the calculated flow field. This is accomplished by applying a switched Schuman filter<sup>15</sup> with a density switch after the completion of each corrector step, prior to decoding. (The use of the Schuman filter is one way of introducing artificial viscosity.) For interior points smoothing is applied to the conservation vector  $U$ , while at the body and fin surfaces it is applied along the surface to the advanced quantities. The smoothing algorithm is as follows:

interior (52a)

$$\begin{aligned} \vec{U}_{i,j} = & \vec{U}_{i,j}^c + (\vec{U}_{i+1,j}^c - \vec{U}_{i,j}^c) C_{i+1/2,j} - (\vec{U}_{i,j}^c - \vec{U}_{i-1,j}^c) C_{i-1/2,j} \\ & + (\vec{U}_{i,j+1}^c - \vec{U}_{i,j}^c) C_{i,j+1/2} - (\vec{U}_{i,j}^c - \vec{U}_{i,j-1}^c) C_{i,j-1/2} \end{aligned}$$

wall (52b)

$$\vec{W}_{i,j} = \vec{W}_{i,j}^c + (\vec{W}_{i,j+1}^c - \vec{W}_{i,j}^c) C_{i,j+1/2} - (\vec{W}_{i,j}^c - \vec{W}_{i,j-1}^c) C_{i,j-1/2}$$

fin (52c)

$$\vec{H}_{i,j} = \vec{H}_{i,j}^c + (\vec{H}_{i+1,j}^c - \vec{H}_{i,j}^c) C_{i+1/2,j} - (\vec{H}_{i,j}^c - \vec{H}_{i-1,j}^c) C_{i-1/2,j}$$

corner (52d)

$$\vec{J}_{i,j} = \vec{J}_{i,j}^c + (\vec{J}_{i,j+1}^c - \vec{J}_{i,j}^c) C_{i,j+1/2} - (\vec{J}_{i,j}^c - \vec{J}_{i+1,j}^c) C_{i+1/2,j}$$

$$\text{where } \vec{W}_{i,j} = \begin{Bmatrix} \ln p_{i,j} \\ s_{i,j} \\ u_{i,j} \frac{b_{i,j}}{b_j} + v_{i,j} \end{Bmatrix}; \quad \vec{H}_{i,j} = \begin{Bmatrix} \ln p_{i,j} \\ s_{i,j} \\ u_{i,j} + (r_{ij}) \frac{v_{i,j}}{r_{i,j}} \end{Bmatrix}$$

$$\vec{J}_{i,j} = \begin{Bmatrix} \ln p_{i,j} \\ s_{i,j} \end{Bmatrix}$$

$$C_{i+1/2,j}^c = \frac{(\rho_{i+1,j} - \rho_{i,j})}{(\rho_{i+1,j} + \rho_{i,j})} C_X; \quad C_{i,j+1/2}^c = \frac{(\rho_{i,j+1} - \rho_{i,j})}{(\rho_{i,j+1} + \rho_{i,j})} C_Y$$

Here  $C_X, C_Y$  are specified constants. The superscript  $c$  indicates the quantity values following the corrector step. The switched Schuman filter smooths quantities in conservative form which preserves the numerical scheme's ability to capture shocks at interior points. Application of the switched Schuman filter to the advanced wall, body, and fin quantities, rather than to  $p, \rho, u, v, w$ , ensures that the final flow variables at a surface point satisfy the flow tangency boundary condition and the total enthalpy constraint, (7).

Smoothing is applied only when requested by the user or at interior points if the decoded pressure value is negative. In the later case, only the point at which the negative pressure occurred is smoothed using  $C_{i+1/2,j} = .25$  and  $C_{i,j+1/2} = 0$ . A diagnostic message is also printed indicating that this procedure has been applied. In the sample calculations discussed in Section 4 the user specified smoothing is applied only where indicated and the automatic smoothing is rarely invoked.

### 3.4 BODY CROSSFLOW SEPARATION

At incidences greater than about  $10^\circ$ , the flow on the leeside of a slender body separates and forms a symmetric vortex pattern. When such a configuration is treated with an inviscid code, a crossflow shock develops (illustrated qualitatively on Figure 8) and the surface pressure ahead of the shock becomes unrealistically low. It has been observed in Ref. 16 that a more realistic lee side flow pattern may be achieved by prescribing body surface boundary conditions that facilitate crossflow separation. This section describes a procedure that may be used with the present code to simulate crossflow separation in cases where pitch plane symmetry exists. The present method prescribes the direction of the two body surface streamlines located nearest to the experimentally observed separation line.

The separation line on the body surface can be specified by prescribing

$$\phi_s = \phi_s(z) \quad (53)$$

The position vector,  $\vec{r}_s$ , of the point on the separation line in the meridian plane  $\phi_s$  is given by

$$\vec{r}_s = b(\phi_s, z) \vec{e}_r + z \vec{e}_z$$

and the unit vector,  $\vec{t}_s$ , tangent to the separation line, by

$$\vec{t}_s = \frac{d\vec{r}_s}{dz} / \left| \frac{d\vec{r}_s}{dz} \right| \quad (54)$$

where

$$\frac{d\vec{r}_s}{dz} = \frac{\partial \vec{r}_s}{\partial \phi} \phi'_s + \frac{\partial \vec{r}_s}{\partial z} = (\phi'_s b_\phi + b_z) \vec{e}_r + \phi'_s b_\phi \vec{e}_\phi + \vec{e}_z$$

$$\phi'_s \equiv \frac{d\phi_s}{dz}$$

The specific form of (53), used in the present program, is the following correlation of experimental data for circular bodies (Reference 17):

$$\phi_s = 2.23 \left\{ \frac{1}{2} [z/b(z) - 3.] \tan \alpha \right\}^{-.23} \quad (53a)$$

for  $z > (.450/\tan \alpha + 3)b(z)$ .

Noting that the crossflow velocity is the projection of the velocity vector onto the  $z = \text{constant}$  plane, and that the tangent to the body in the crossflow plane is  $(b_\phi/b) \vec{e}_r + \vec{e}_\phi$ , the ratio of the total velocity to the crossflow velocity is given by

$$\psi = \frac{[(b_\phi/b) \vec{e}_r + \vec{e}_\phi] \cdot \vec{q}}{q \sqrt{(b_\phi/b)^2 + 1}} = \frac{V_2}{\sqrt{(2H_0 - h) [(b_\phi/b)^2 + 1]}} \quad (55)$$

At the separation point, the surface velocity is prescribed to be in the direction of  $\vec{t}_s$  and is given by (54). This is enforced by solving (55) for  $V_2$  using  $\psi = \psi_s$ , where  $\psi_s$  is determined from:

$$\psi_s = \frac{[(b_\phi/b) \vec{e}_r + \vec{e}_\phi] \cdot \vec{t}_s}{[(b_\phi/b)^2 + 1]^{1/2}} = \frac{(b_\phi/b) (\phi'_s b_\phi + b_z) + \phi'_s b}{\left\{ [(b_\phi/b)^2 + 1] [(\phi'_s b_\phi + b_z)^2 + \phi'^2_s b^2 + 1] \right\}^{1/2}} \quad (56)$$

Since the present method does not explicitly track the separation point, (56) cannot be imposed directly because separation generally occurs between computational points. It is, therefore, assumed that the crossflow velocity ratio,  $\psi$ , varies smoothly on the body surface and that the separation affects only the two body points adjacent to the separation point.

Consider the case where the separation point lies between  $(X_1, Y_m)$  and  $(X_1, Y_{m+1})$ . The required  $\psi$ 's at  $(X_1, Y_m)$  and  $(X_1, Y_{m+1})$  are determined using the following linear interpolations:

$$\psi_{1,m} = \psi_{1,m-1} + (\psi_s - \psi_{1,m-1}) (\phi_{1,m} - \phi_{1,m-1}) / (\phi_s - \phi_{1,m-1}) \quad (57)$$

$$\psi_{1,m+1} = \psi_{1,m+2} + (\psi_s - \psi_{1,m+2}) (\phi_{1,m+1} - \phi_{1,m+2}) / (\phi_s - \phi_{1,m+2})$$

Here  $\psi_{1,m-1}$  and  $\psi_{1,m+2}$  are calculated by evaluating (56) using the flow properties at points  $(X_1, Y_{m-1})$  and  $(X_1, Y_{m+2})$  respectively. To ensure that pressure and density behave smoothly near the separation point,  $s$  and  $p$  at points  $(X_1, Y_m)$  and  $(X_1, Y_{m+1})$  are determined by linear interpolation:

$$p_{1,m+j} = p_{1,m-1} + (p_{1,m+2} - p_{1,m-1}) (\phi_{1,m+j} - \phi_{1,m-1}) / (\phi_{1,m+2} - \phi_{1,m-1}) \quad (58)$$

$$s_{1,m+j} = s_{1,m-1} + (s_{1,m+2} - s_{1,m-1}) (\phi_{1,m+j} - \phi_{1,m-1}) / (\phi_{1,m+2} - \phi_{1,m-1})$$

where:  $j = 1, 2$

At the end of each computational step the advanced quantities at points  $(X_1, Y_m)$  and  $(X_1, Y_{m+1})$  are decoded using (17) which enforces the tangency boundary conditions and the correct stagnation enthalpy.

Application of (55), (56), (57) and (58) on a circular body produces a vortex in the leeward flow field. Crossflow velocities which are positive on the windward side of the body become negative leeward of the separation point. When the flow field vortex becomes sufficiently large, an interval of positive surface crossflow velocities (i.e., a secondary separation) develops between the separation point and the leeward symmetry plane. This interval is unstable and, shortly after such a region develops, the calculation fails unless the body smoothing option is applied.



## SECTION 4

## COMPARISON OF CALCULATION AND EXPERIMENT

This section presents comparisons of calculation and experiment using the algorithms outlined in Sections 2 and 3. A description of the computer code, listing and set of user's instructions can be found in Ref. 11. The range of cases covered in this section includes body alone with and without crossflow separation, body-fin configurations with supersonic, subsonic and transonic leading edges and a body-wing-tail configuration with and without tail deflection. The input variables used to execute each run are listed in Ref. 11. Most of the cases presented in this section have been reported previously<sup>13,18,19</sup>. However, different versions of the numerical method were used in these references and in some instances the results may differ from those shown in this report.

All the cases featured in this report have bodies with pointed nose tips. The initial data plane is located near the tip and the flow field on this plane is generated using a method described in Ref 11. This procedure provides an estimate for the flow field about a cone tangent to the body at the starting plane by integrating one-dimensional conical equations. The resulting flow field is approximate except at zero incidence. Experience suggests that the calculations described in this section are relatively insensitive to the flow field used at the starting plane.

**4.1 BODY ALONE.** A body alone calculation was carried out with and without crossflow separation on a tangent ogive cylinder of nose fineness 3, and afterbody length of 10 calibers. The angle of incidence was  $15^\circ$  and the free stream Mach number was 3. To minimize the computational cost, the runs were completed in three steps. The first part covered  $Z/D < 2$  and used a uniform  $11 \times 13$  mesh\* while the second and third used a  $31 \times 37$  mesh. The third section covered  $Z/D > 5$  and featured mesh clustering in the  $r$  direction. In the crossflow separation run, the separation started at  $Z/D = 2$ . As shown in Fig. 9, application of the crossflow separation brings the flow field into reasonable qualitative agreement with the measurements of Oberkampf<sup>20</sup>. Calculated surface pressures with and without crossflow separation are compared in Fig. 10. In both cases the computed pressure is considerably lower than experimental in the vicinity of separation. The pressure rise on the leeward side of the body in the crossflow separation case is triggered by separation, while in the other case it is due to the crossflow shock which develops on the leeside of the body.

\*The notation  $(N \times M)$  indicates  $N$  planes in the  $r$  direction and  $M$  planes in the  $\phi$  direction.

4.2 CONFIGURATIONS WITH SUPERSONIC LEADING EDGES. In Ref. 21 a tangent ogive body, equipped with tail fins or several different planforms, is tested in supersonic flow. The fins feature surface slope discontinuities at various locations along the surface. The free stream Mach number is sufficiently large to allow an attached shock solution at the fin leading edge in almost all cases. Numerical results have been compared to experimentally measured surface pressures taken at Mach 3.7 for configurations featuring clipped delta and cranked tail fins.

Calculations for these cases were made in two sections. A uniform 13 X 13 mesh was used to advance the calculation to an axial station slightly forward of the tail leading edge. The flow field was then rezoned to a uniform 40 X 37 mesh for the computations over the tail surfaces. The leading edges were treated using option 1 (i.e., by applying the local analysis) and X differencing option 1 was used until the fin tip was encountered. Along the fin tip the adjacent interior point was advanced using option 0 as was the fin tip point on the compression (i.e., lower) side of the fin. The fin tip point on the expansion surface of the fin was advanced using option 1.

Calculated and measured fin surface pressures are compared for the cranked and clipped delta fin configurations in the "+" and "X" roll orientation in Figs. 11 to 15. All figures show reasonable agreement between calculation and experiment. The scatter in the experimental data is a result of using experimental measurements from repeated runs. On fin surfaces which feature strong leading edge shocks, the predicted results tend to be lower than experimental. Also, the pressures are not accurately predicted along the body-fin junction. The body boundary layer and the fin leading edge shock interaction, presumably have an influence on the corner and account for much of this discrepancy. On fin surfaces which have a weak leading edge shock or expansion, the predicted and measured fin tip pressure profiles are in good agreement. However, the pressures along the corner are underpredicted. Over the entire span, calculated pressures on the trailing edge panel tend to be less than measured, probably reflecting the existence of a thick boundary layer or separation.

A flow field vector, pressure and density contour plots, in a crossflow plane upstream of the trailing edge, are shown in Fig. 16. There are no experimental data available for comparison; however, the results appear to be qualitatively correct and show a leading edge shock propagating into the flow field from all three fins.

The normal force and pitching moment computations for an airplane type configuration at Mach 2 are shown on Fig. 17 in comparison to experimental data of Ref. 22. This case features attached shocks on the wing and tail surfaces. The calculation was carried out using a uniform 13 X 13 mesh forward of the wing and a uniform 19 X 19 mesh over the remainder of the body. The leading edge and X differencing options were set to 1. To prevent the flow from becoming subsonic along the wing-body junction, the leading edge turning angle at this location was damped by setting  $C_T = .25$  for wing compression and tail surfaces and  $C_T = .5$  on the wing expansion surface. The computed and measured normal force and pitching moment coefficients for body-wing and body-wing-tail configurations at an incidence of  $10^\circ$  are in good agreement. The computed crossflow field at an axial station just upstream of the wing trailing edge and tail section are illustrated on Fig. 13.

4.3 CONFIGURATIONS WITH TRANSONIC LEADING EDGES. This section focuses on cases where the Mach number normal to the leading edge is near unity and is too small to allow an attached leading edge shock. Under these conditions the local analysis at the leading edge is approximate.

The wind tunnel tests of Ref. 14 offer an opportunity to compare calculation and experiment for the swept wing configuration depicted in Fig. 19. Measurements were taken on two wings with the same planform but different thicknesses. The calculations were performed at Mach numbers of 2.5 and 4.5, at incidences of  $2^\circ$  and  $6^\circ$  using a uniform 15 X 13 mesh, and with leading edge and X differencing options set to 1. The wing section of the configuration was also rerun on a finer 25 X 25 mesh for the thin wing configuration at an incidence of  $6^\circ$  at both Mach numbers. A comparison of calculated and measured wing and body surface pressures is presented in Figs. 19 to 24. The calculated crossflow field of the thin wing configuration at  $\alpha = 6^\circ$  is presented in Figs. 25 and 26 for Mach numbers of 4.5 and 2.5 respectively. In each case the crossflow velocity vectors, pressure and density contours are illustrated at axial stations slightly forward of the trailing edge point of the wing-body junction.

Another example of a configuration with transonic leading edges for which experimental data were available, is illustrated in Figs. 27 to 30. In Ref. 23, pressure measurements are provided on wing and body surfaces for both "+" and "X" roll orientations. Calculations were performed at Mach 2.7 at  $10^\circ$  incidence for both roll orientations. A uniform 11 X 13 mesh was used forward of the wing and a uniform 18 X 21 mesh for the remainder. Leading edge and X differencing options were set to 1. Calculated and measured fin surface pressures are compared in Figs. 27 and 28 which represent the "+" and "X" roll orientations respectively. In both cases the leading edge points near the body feature detached shocks, while those further outboard on the wings have attached shocks. Figs. 29 and 30 compare calculated and measured body surface pressures for the "+" and "X" roll orientations respectively. The calculated crossflow fields forward and aft of the trailing edge are illustrated in Figs. 31 and 32 for both of these orientations.

The final transonic leading edge example considered is a swept wing model depicted in Fig. 33. The experimental data are taken from Ref. 24 and include pressure measurements on the wing and body surfaces. Calculations have been made at Mach numbers of 2.3 and 2.96 at incidences of  $8.8^\circ$  and  $8.6^\circ$  respectively. A uniform 13 X 13 mesh was applied to the nose region ( $z < 5$ ) while the remainder of the body was calculated using an 18 X 19 mesh. Option 1 was used for the leading edge and for the X differencing. Wing surface pressure results are compared to experimental values in Figs. 33 and 34 for Mach numbers of 2.3 and 2.96 respectively. Calculated and measured body surface pressures are shown in Figs. 35 and 36 and the computed crossflow plane flow fields at an axial station upstream of the trailing edge are illustrated in Figs. 37 and 38.

A comparison of calculated and measured fin surface pressures for all three configurations indicates that on expansion surfaces agreement is reasonably good except at the combination of low Mach number and high incidence conditions, where experimental values are smaller than the predicted ones. On compression surfaces best agreement was obtained for the swept configuration of Ref. 14 (see

Figs. 19-22). This is to be expected since these data were used to generate the semi-empirical leading edge relation. Reasonable agreement was obtained for the other two cases (i.e., Figs. 27, 28 and 33, 34) which lends credence to the semi-empirical leading edge analysis. The calculated body surface pressures (see Figs. 23, 24, 29, 30, 35, 36) also feature correct behavior in the presence of the wing. On the windward side of the body, surface pressure increases generated by the presence of the wing, are correctly accounted for, although the location of the predicted pressure peak, in some cases, is downstream of the measured one. On the leeside of the body the calculated body surface pressure decreases appropriately in the vicinity of the wing, and there is no evidence of a discrepancy between the locations of the predicted and measured pressure minimums. In some cases (i.e., Fig. 23, 24) there is a substantial difference between predicted and measured pressure levels on the leeside of the body. This is, most likely, attributable to the leeside boundary layer influence.

**4.4 CONFIGURATIONS WITH SUBSONIC LEADING EDGES.** The cases examined in this section feature highly swept wings having leading edge normal Mach numbers that are less than unity. Under these conditions, the flow rounding the edge of the wing separates and rolls up to form a vortex which, in turn, induces a large suction on the lee surface of the wing. Previous studies (e.g., Ref. 25) have indicated that numerical solutions to Euler's equations exhibit this type of flow field for wings with subsonic leading edges.

The first case considered is the swept wing shown in Fig. 39. Experimental surface pressures are taken from Ref. 26, and the comparison is shown for a Mach number of 2.86 and an incidence of  $10.3^\circ$ . The current computational procedure requires the presence of a missile body. Hence, it was necessary to add to the wing-alone shape a small circular centerbody of a diameter equal to the wing thickness. The nose tip for this body consisted of a cone of a half angle of  $5^\circ$ . The presence of this center body invalidates a surface pressure comparison near the center of the wing. However, farther along the span, this wing should provide a meaningful comparison of experiment and calculation. The computation was carried out with a uniform  $19 \times 19$  mesh. Smoothing was applied to the interior of the flow field and also to the wing and leeward body surfaces. On the windward surface, option 0 was used for the leading edge and the X differencing while on the leeward surface the respective options were 2 and 1. The interior point, adjacent to the wing tip, was advanced using X differencing option 0. The surface slope discontinuity jump was suppressed for  $z < 10.6$ . A comparison of the calculated and measured surface pressures on the upper and lower wing surfaces is presented in Fig. 39. The leeside pressure profile exhibits the expected suction near the outer tip. On the compression surface the predicted pressures tend to be lower than experimental. The crossflow velocity vectors and pressure and density contours are plotted on Fig. 40 at an axial station just upstream of the trailing edge. The expected leeside vortex is evident.

In Fig. 41 normal force and center of pressure prediction for two body-wing-tail configurations are compared to experimental data of Ref. 27. Calculations for these bodies have been carried out at a free stream Mach number of 2.86 and incidences of  $6^\circ$  and  $12^\circ$ , with and without tail deflection. The computations were completed in three sections: upstream of the wing, wing section, and the tail section. The respective mesh sizes were  $13 \times 13$ ,  $19 \times 25$ , and  $19 \times 25$ . The effect of the horizontal tail deflection of  $-20^\circ$  is shown in

Fig. 42. The deflected tail case was simulated by decreasing the slope angle,  $\nu$ , on the compression surface by  $\tan(20^\circ)$  and increasing it on the expansion surface by the same amount. The wing featured subsonic leading edges, and leading edge option 0 was applied on compression surfaces and option 2 on expansion surfaces. The X differencing option 0 was used on the compression surface and on the interior point adjacent to the fin tip, while option 1 was used on the expansion surface. The wing-body junction turn was damped by setting  $C_T = .5$  for both the wing and tail surfaces. For the section of the calculation which covered the wing surfaces, interior points were smoothed using  $C_X = C_Y = .2$  while the expansion wing surface and body surface leeward of the wing was smoothed using  $C_{i,j+1/2} = .2$ . For section 3 of the calculation which covered the tail, leading edge and X differencing options were set to 1 and the interior flow field was smoothed using  $C_X = C_Y = .3$ . The calculated normal force and center of pressure are in reasonable agreement with experiment for both deflected and undeflected tail surfaces. The crossflow velocity vectors are illustrated in Fig. 43 for crossflow planes aft of the wing trailing edge, forwards of the tail leading edge and aft of the tail trailing edge.

## SECTION 5

## CONCLUDING REMARKS

A numerical method has been developed which predicts the inviscid supersonic flow field about finned configurations of engineering interest. The computational requirements are generally modest. All of the cases demonstrated in this report required less than two minutes on a CDC 7600 and used between 110k and 170k core storage (octal). The present study differs from previous methods by treating the fin and body geometries separately. Simple transformations, based on the body alone geometry, are used to map the physical plane into the computational one. A local analysis is applied to fin edge which facilitates the use of coarse computational grids. At present a thin fin approximation is employed which limits the applicability of the computational procedure to relatively thin fins with sharp leading edges. With this formulation it is possible to treat a wide variety of configurations of engineering interest which may contain an arbitrary number of fins at small angles of deflection, camber or dihedral. By appropriate modeling at wing tips and at estimated body separation points, it appears feasible to simulate flow field vortices.

Special procedures are used to analyze the flow on leading and trailing edges. This treatment is dependent on the Mach number of the flow normal to the leading edge. The treatment of the supersonic case is straight forward since the local analysis is exact. In the subsonic and transonic cases the local analysis is empirical and several options are available for treating fin leading edges. Here, experience with similar cases for which there is experimental data may improve results.

The computational procedure has been applied to a number of different configurations. Good agreement has been obtained between experiment and calculation, particularly with respect to aerodynamic coefficients. The calculated pressure is generally in reasonable agreement with experiment. Here deficiencies are more likely to occur near body-fin junctions and close to the leading edges on wings with detached shocks. The pressure gradients on the wing surfaces reflect the correct variation with leading edge Mach number, even on the leeward side of the wing in subsonic flow. Here the appropriate suction appears on the fin surface near to the tip. Vector and pressure contour plots of the flow field have also been presented for a number of cases. Although there is no experimental information for direct comparison, the flow field exhibits the expected structures. For configurations with supersonic leading edges, shock waves can be seen propagating off the edges into the flow field, while in the subsonic case, a large leeside vortex is seen to develop. In several cases normal force and pitching moment coefficients have been calculated and compared to experiment. Good agreement has been obtained even for configurations with deflected tails.

ACKNOWLEDGEMENTS

This work was jointly supported by the Naval Sea Systems Command and the Naval Air Systems Command. The authors would also like to acknowledge the enthusiastic support of Dr. Frank G. Moore of the Naval Surface Weapons Center, Dahlgren, VA., throughout the course of this investigation.

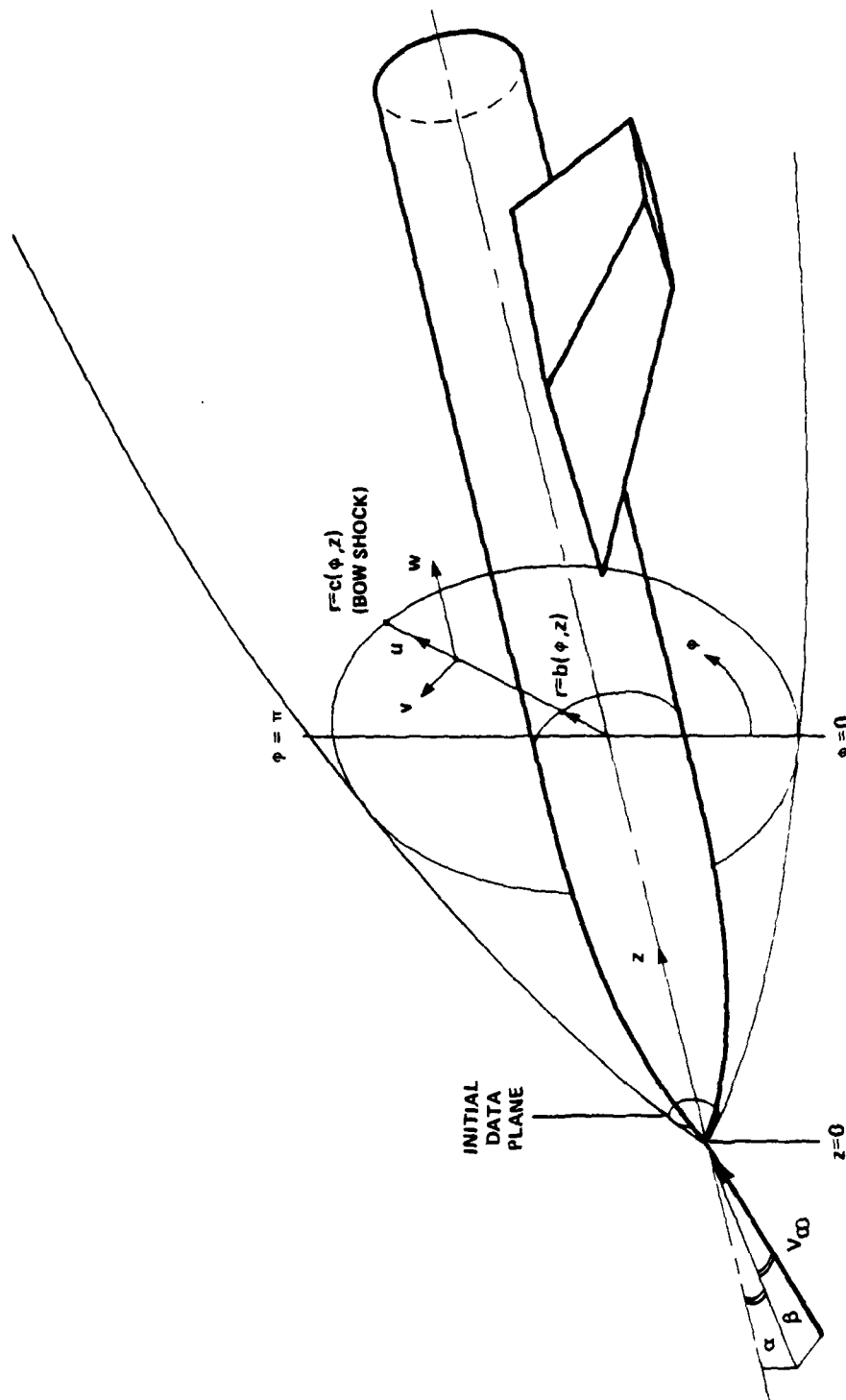


Figure 1. Cylindrical coordinate system used for inviscid flow calculations



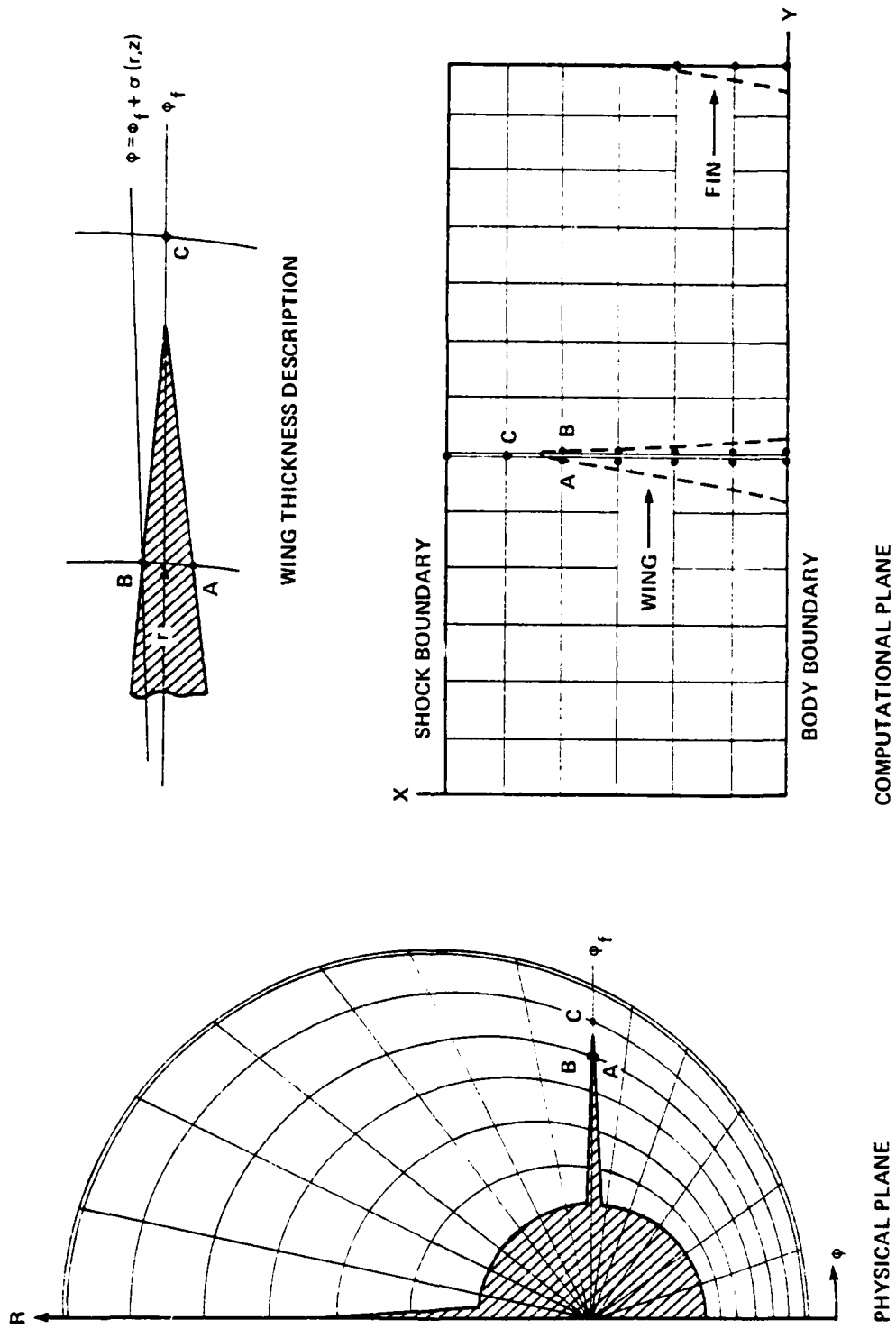


Figure 2. Thin fin approximations in physical and computational coordinates

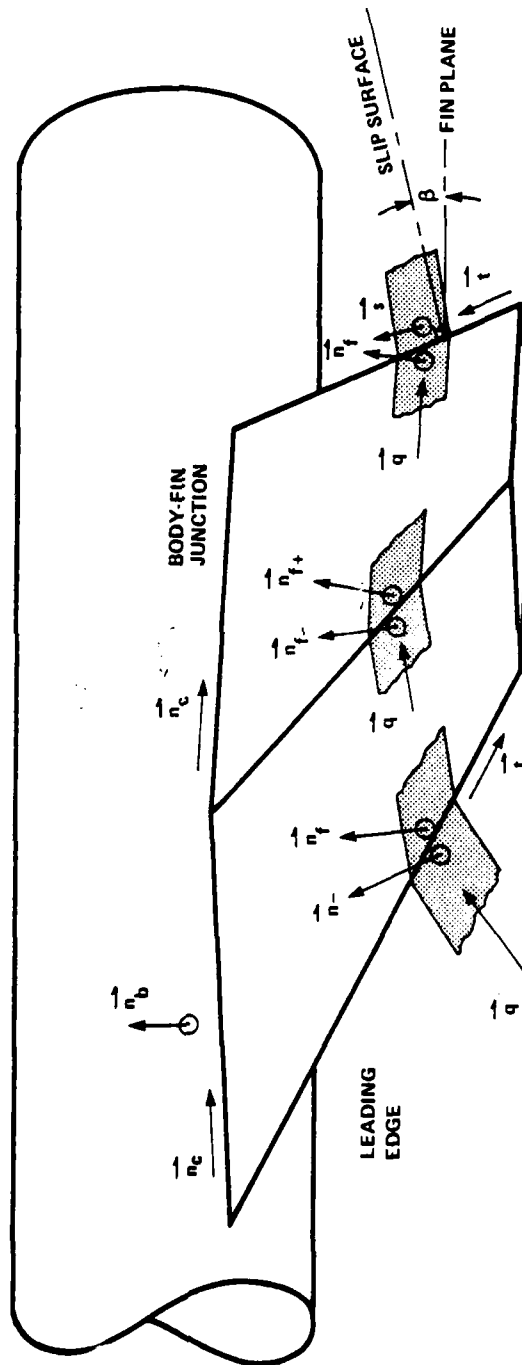


Figure 3. Vectors used in the analysis of fin leading, trailing edges and surface slope discontinuities

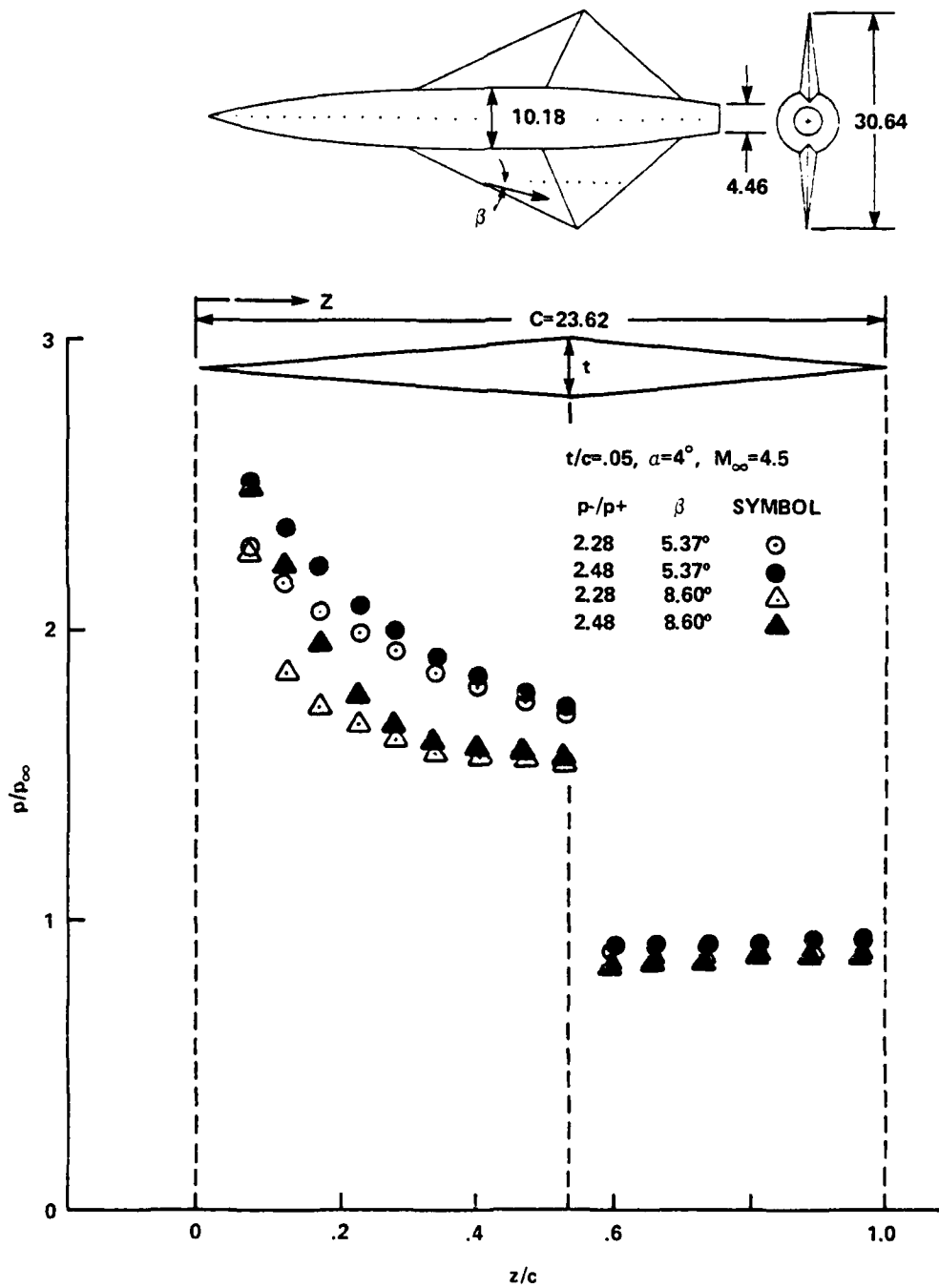


Figure 4. The effect of changing the leading edge pressure and streamline direction on a swept wing surface pressure profile

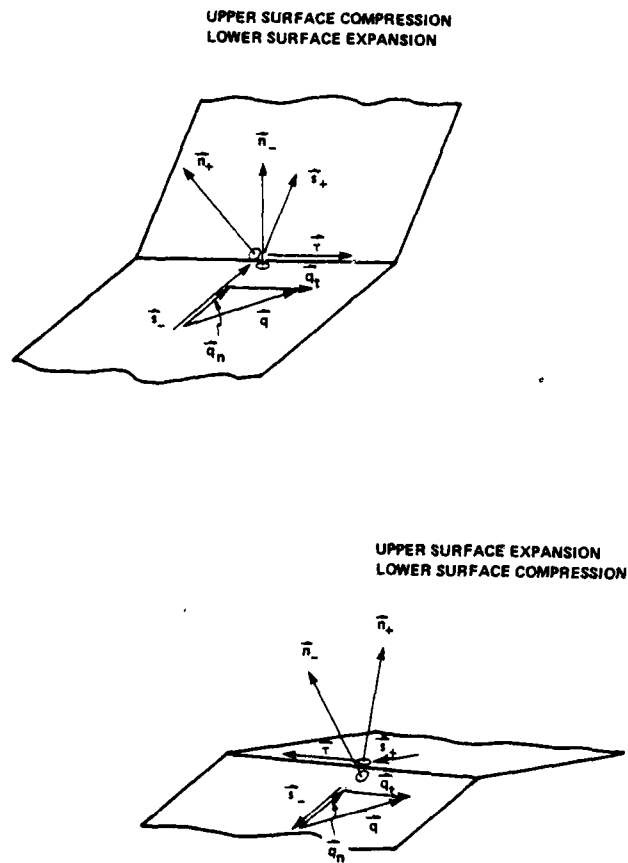


Figure 5. Vectors associated with compression and expansion turns

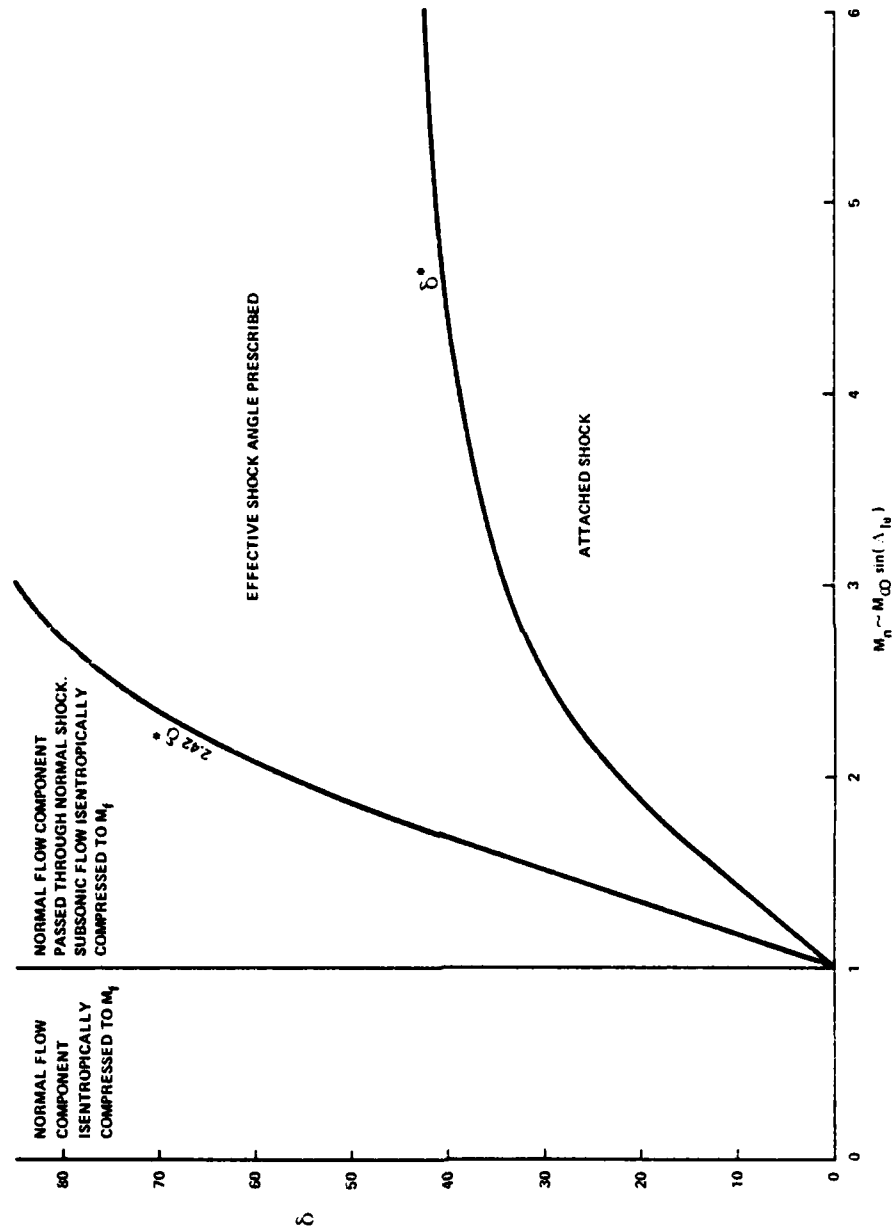


Figure 6. Compression regimes used in the option 1 analysis

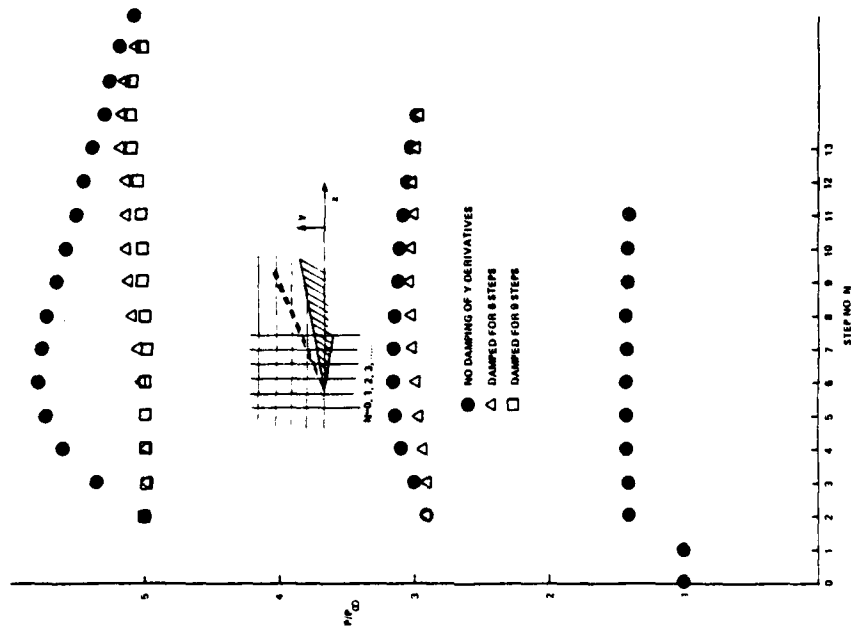


Figure 7. Effect of suppressing  $Y$  derivatives for various strength jumps at the leading edge

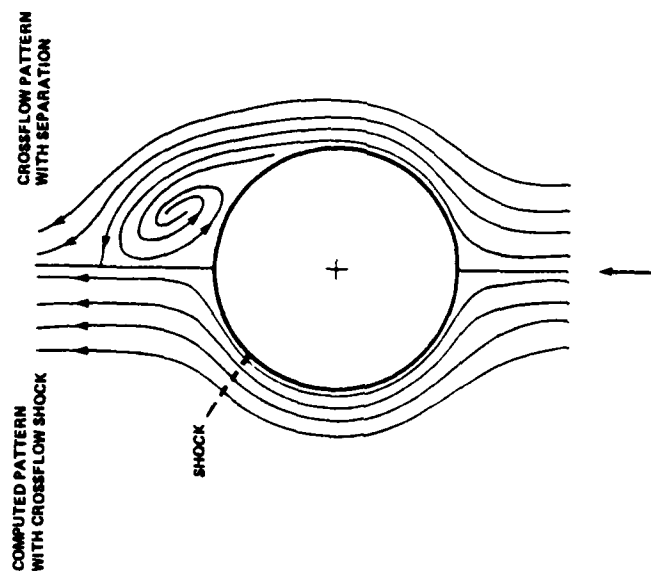


Figure 8. Crossflow plane with and without prescribed separation

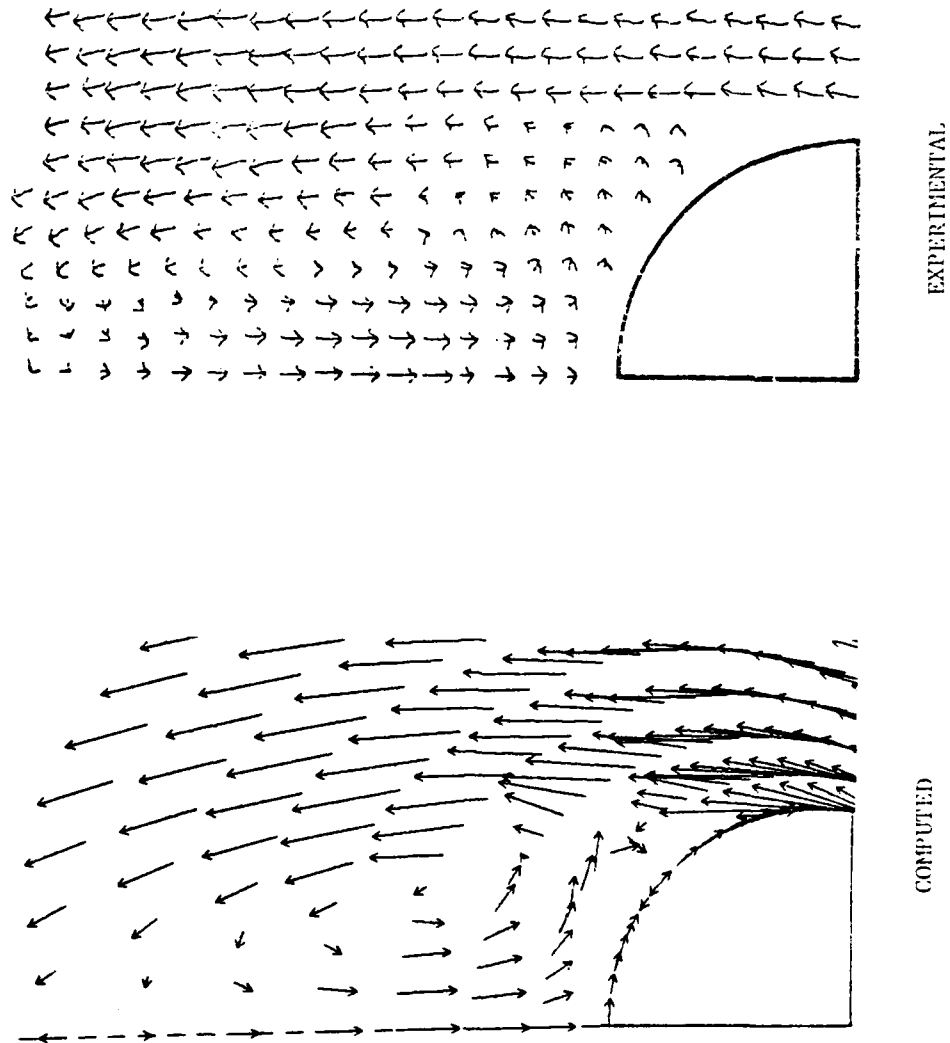


Figure 9. Experimental and calculated flow fields on a body alone configuration,  $\alpha = 15^\circ$ ,  $M = 3.0$ ,  $Z = 1$ ; calibers, Ref. 20

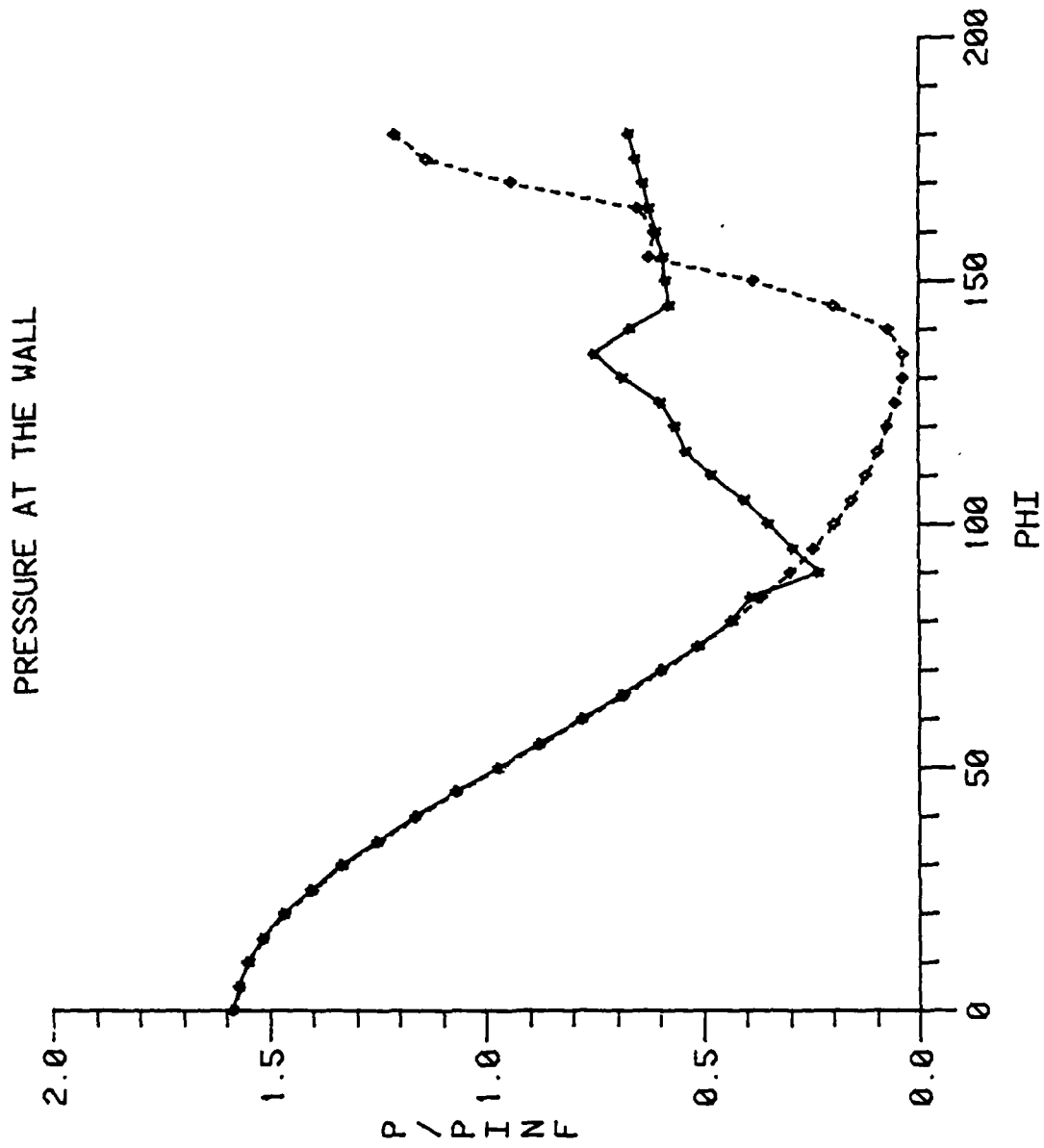


Figure 10. Body alone surface pressure distributions with and without body crossflow separation,  $\alpha = 15^\circ$ ,  $M = 3.0$ ,  $Z = 13$  calibers



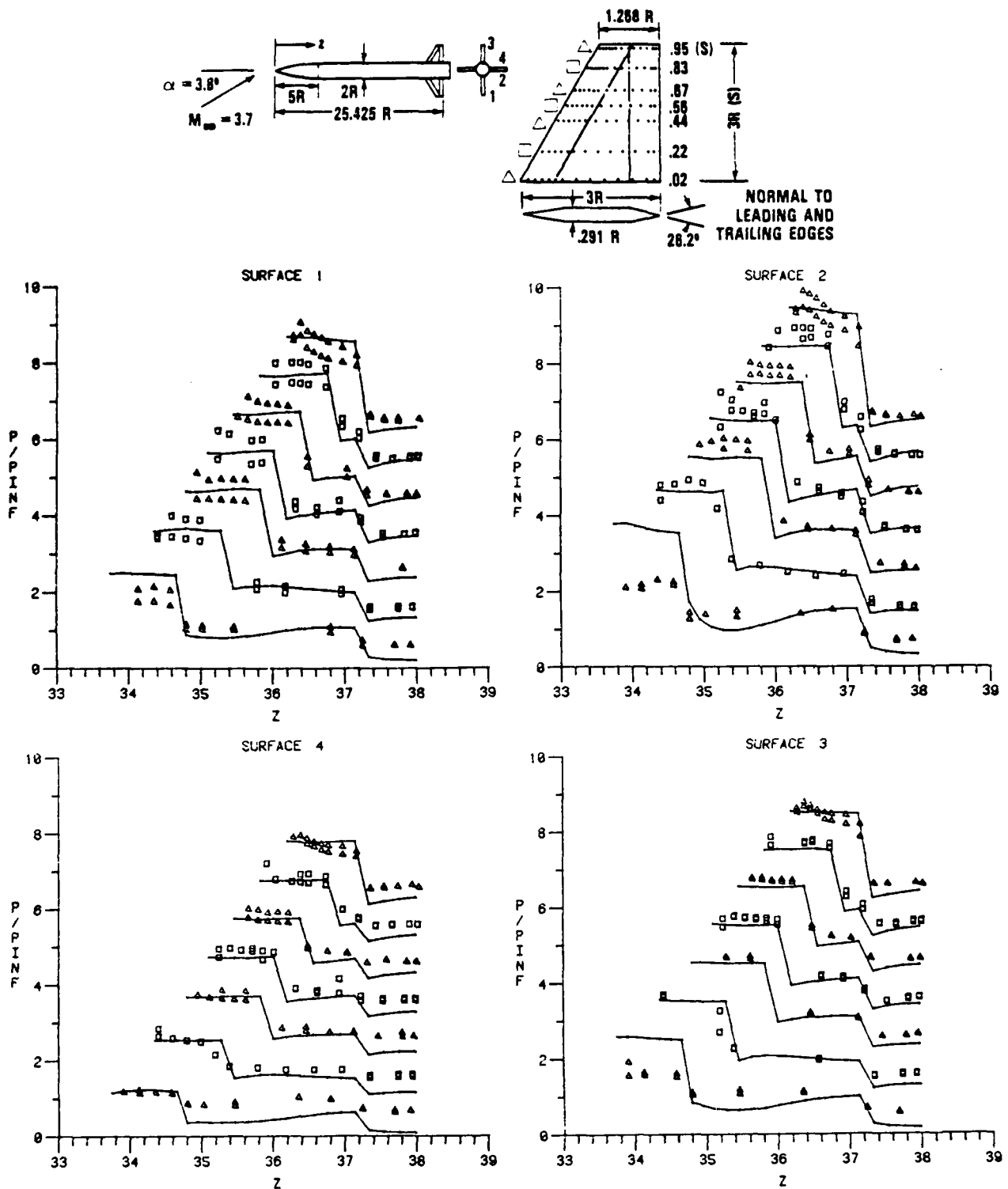


Figure 11. Calculated and measured fin surface pressures on a clipped delta fin configuration in the "+" roll position,  $\alpha = 3.8^\circ$ ,  $M = 3.7$ , Ref. 21. (Zero reference shifted by 1.0 for each successive curve.)

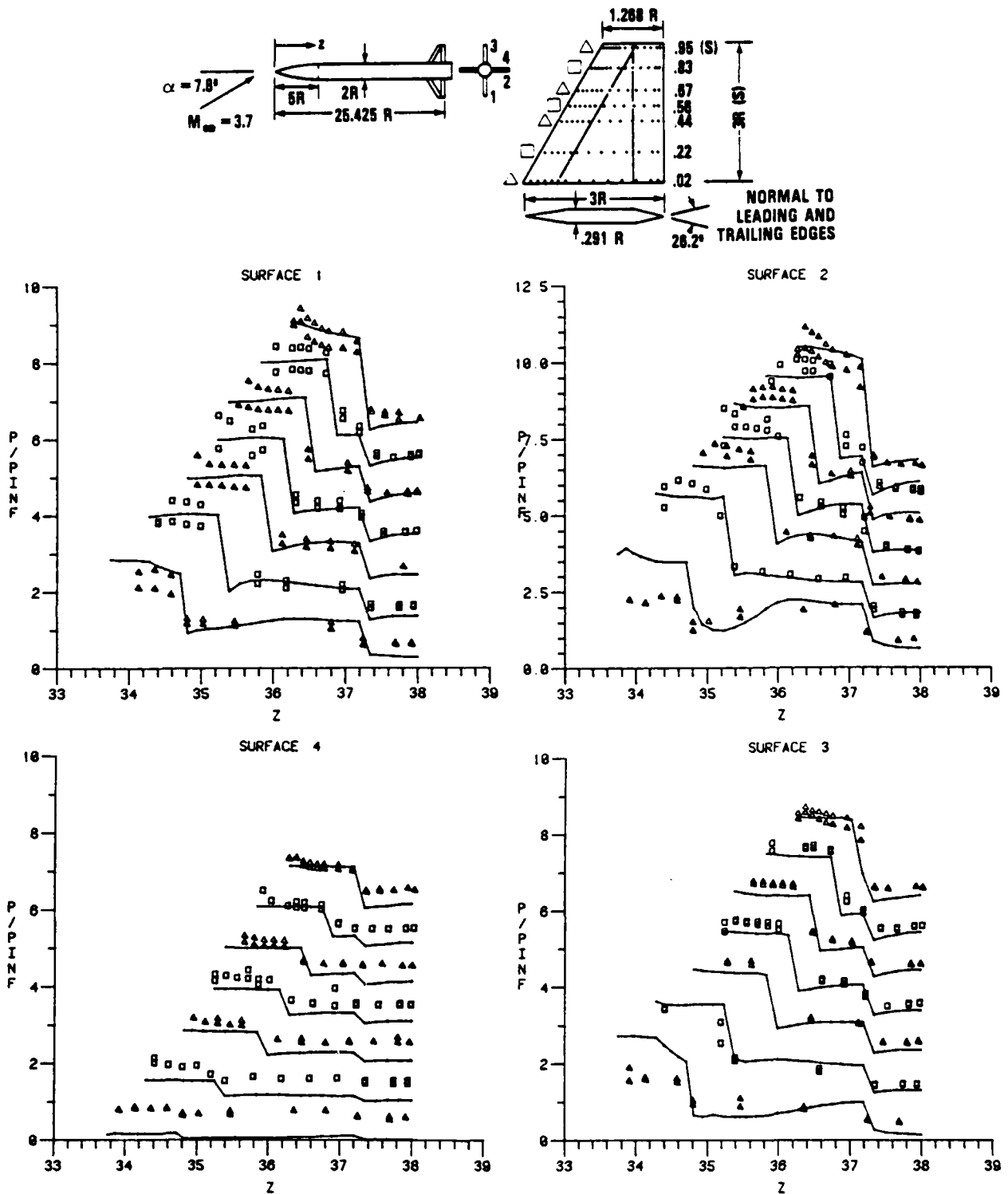


Figure 12. Calculated and measured fin surface pressures on a clipped delta fin configuration in the "+" roll position,  $\alpha = 7.8^\circ$ ,  $M = 3.7$ , Ref. 21. (Zero reference shifted by 1.0 for each successive curve.)

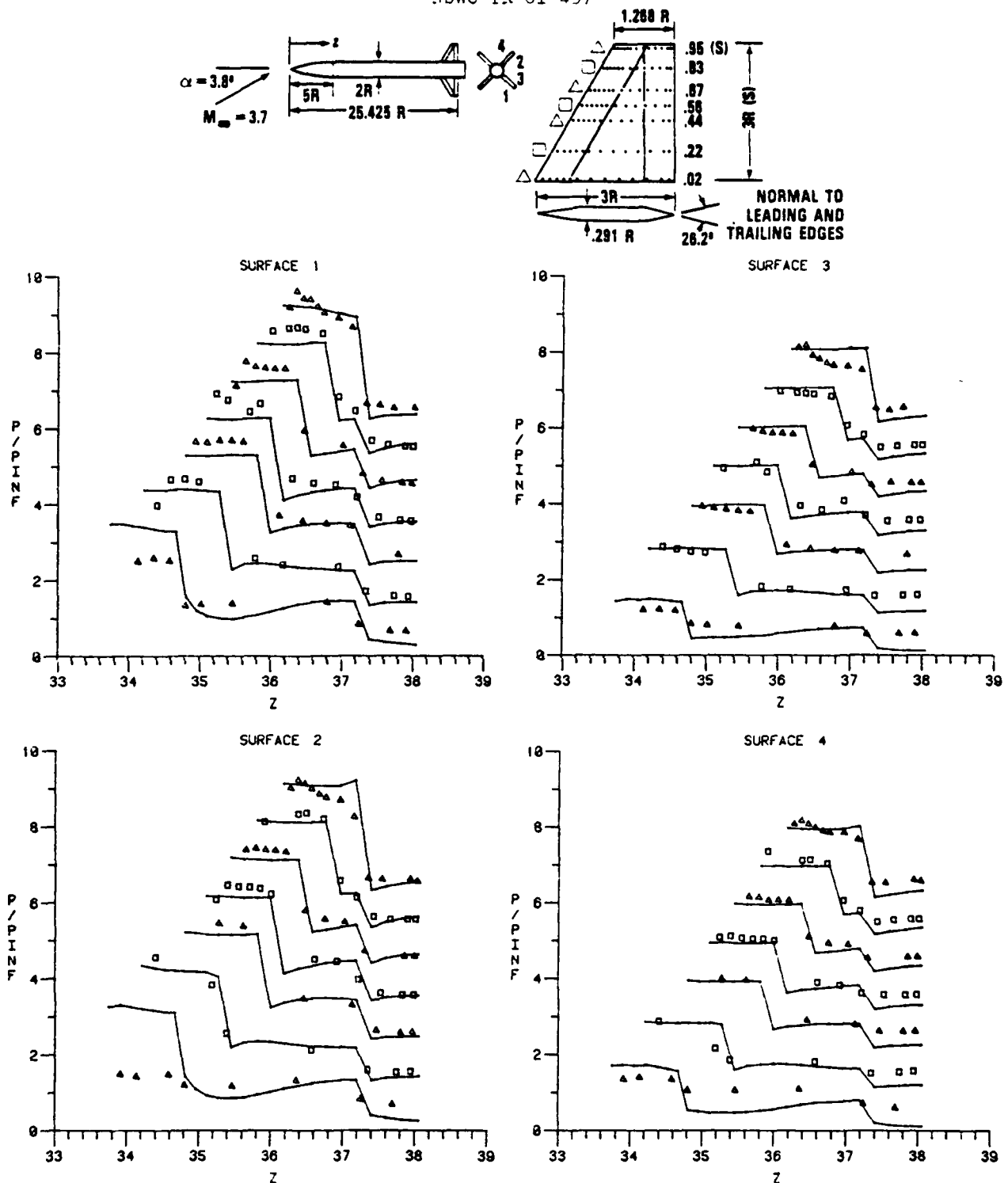


Figure 13. Calculated and measured fin surface pressures on a clipped delta fin configuration in the "x" roll position,  $\alpha = 3.8^\circ$ ,  $M = 3.7$ , Ref. 21. (Zero reference shifted by 1.0 for each successive curve.)

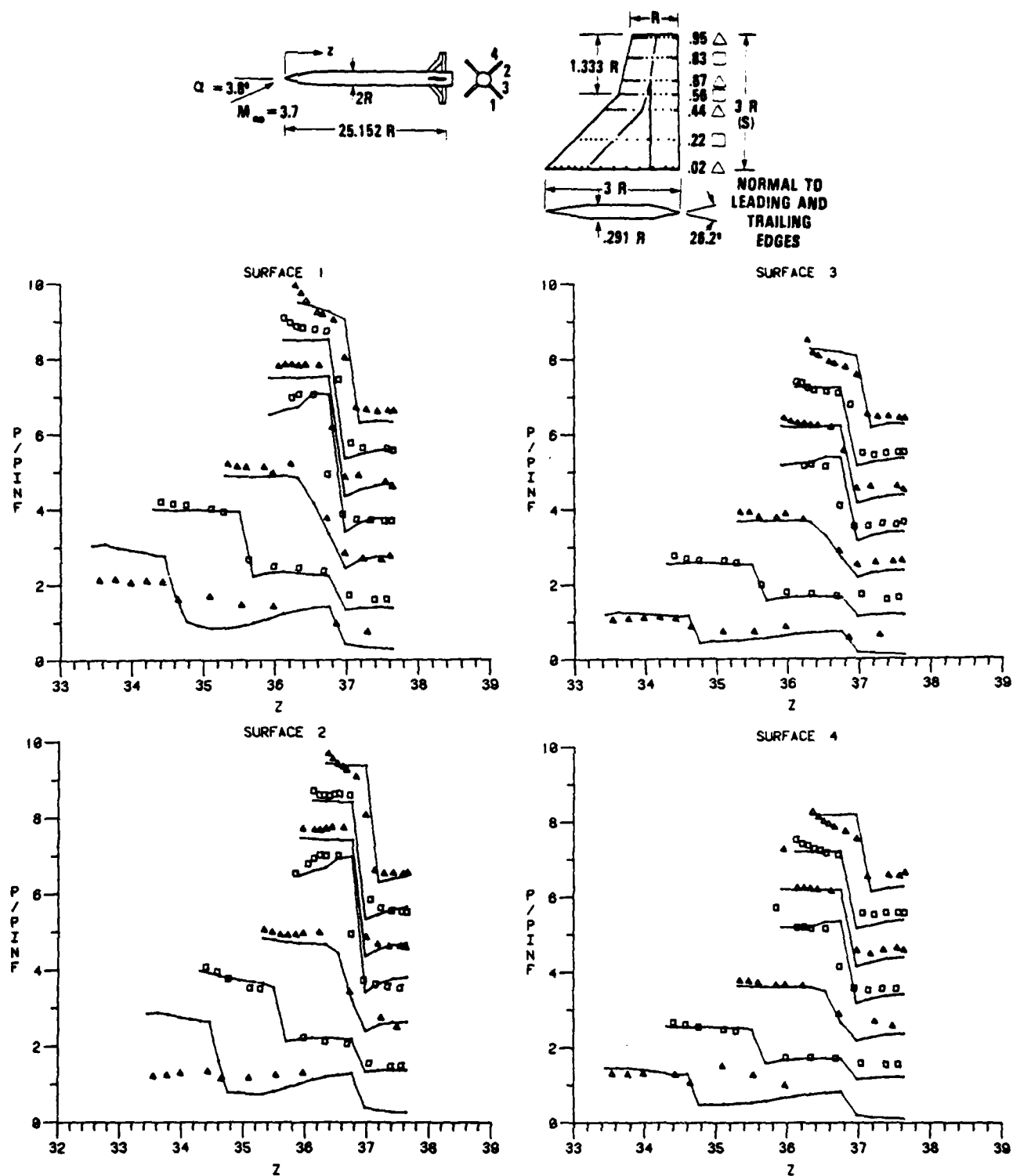


Figure 14. Calculated and measured fin surface pressures on a cranked delta fin configuration in the "x" roll position,  $\alpha = 3.8^\circ$ ,  $M = 3.7$ , Ref. 21. (Zero reference shifted by 1.0 for each successive curve.)

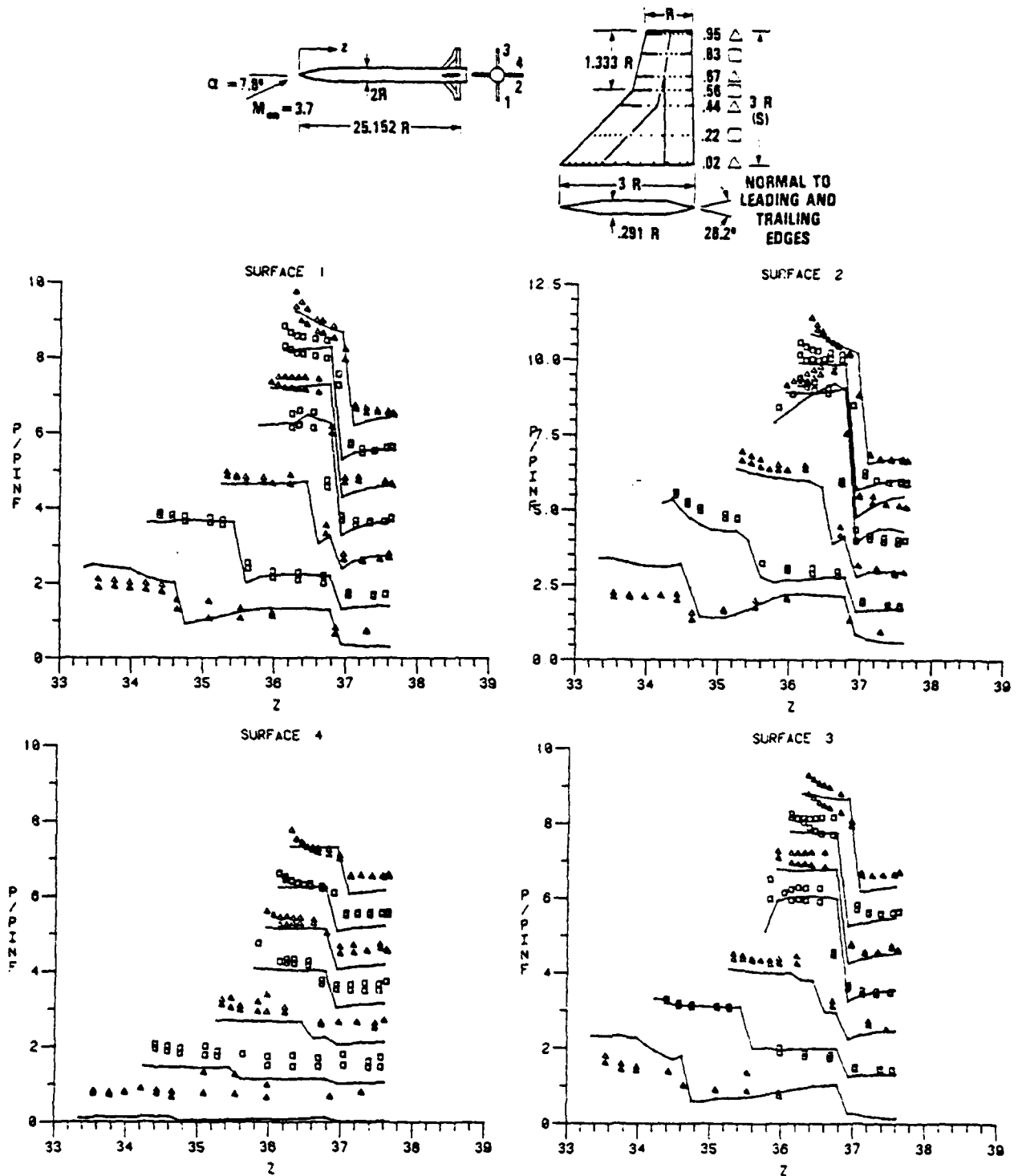


Figure 15. Calculated and measured fin surface pressures on a cranked delta fin configuration in the "+" roll position.  $\alpha = 7.3^\circ$ ,  $M = 3.7$ , Ref. 21. (Zero reference shifted by 1.0 for each successive curve.)

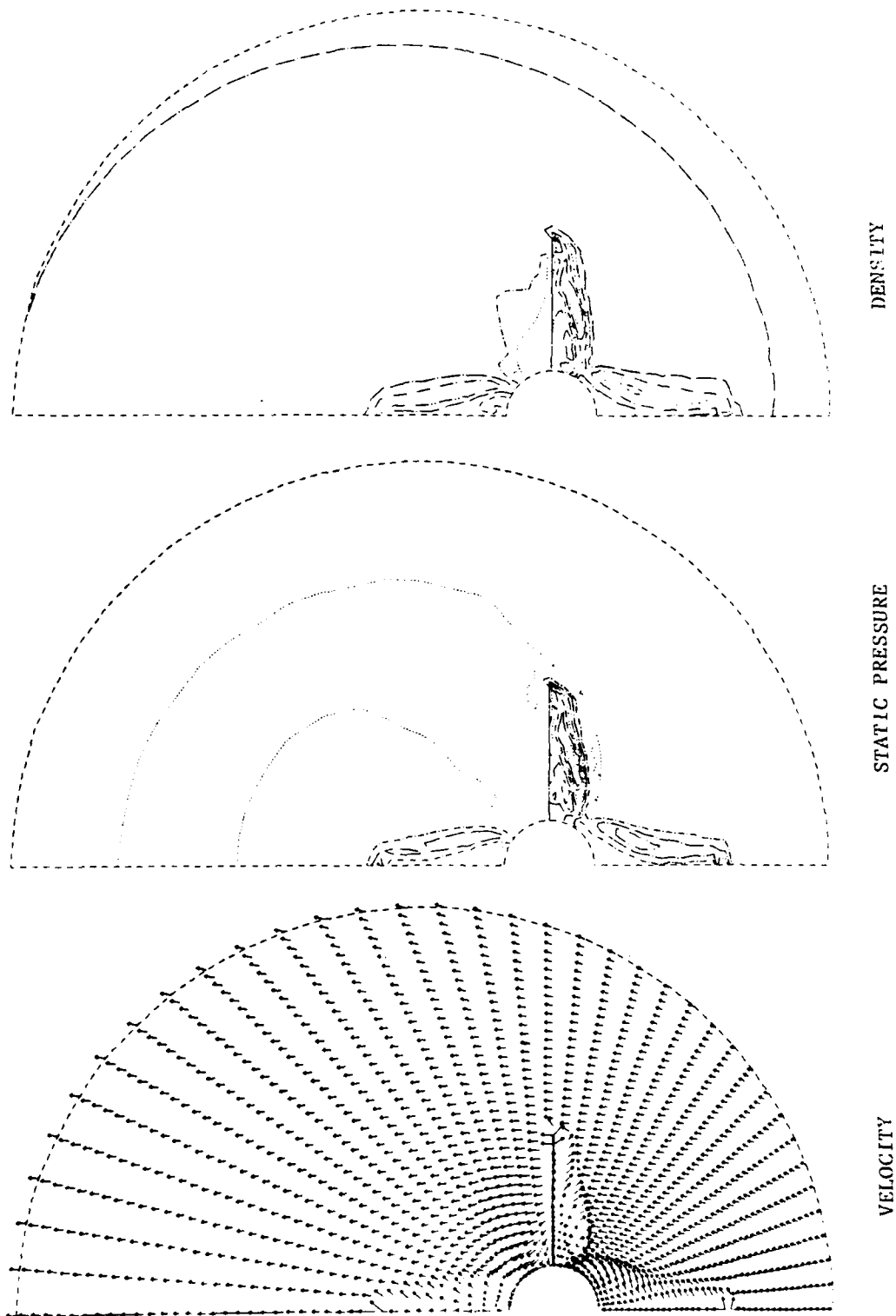


Figure 16. Calculated cross flow field and pressure and density contours for a clipped delta fin configuration in the "4" roll position,  $\alpha = 7.8^\circ$ ,  $M = 3.7$ ,  $Z = 37$ , Ref. 21

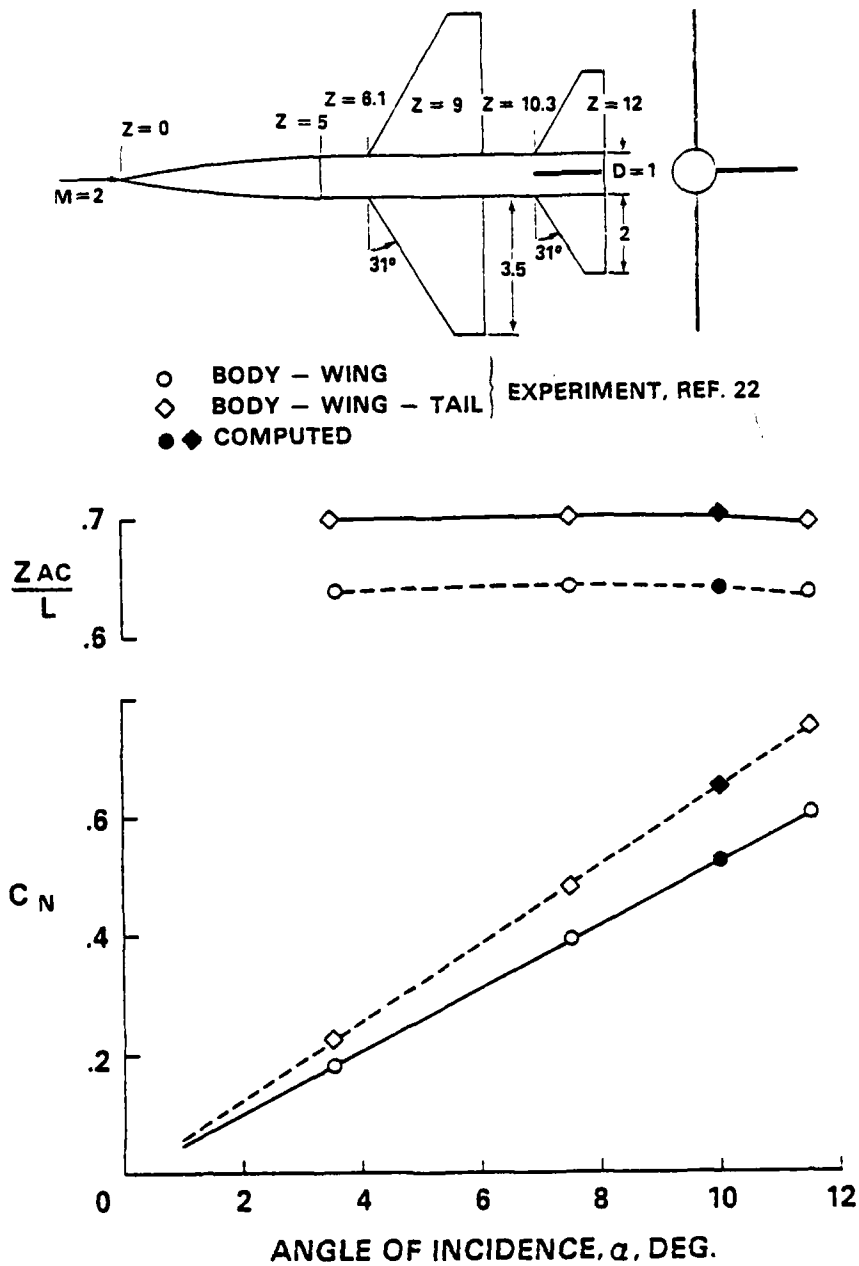


Figure 17. Calculated and measured normal force coefficient,  $C_N$  and center of pressure,  $Z_{AC}/L$ , for body-wing and body-wing-tail configurations of Ref. 20, at  $M = 2.0$ ,  $\alpha \pm 10^\circ$

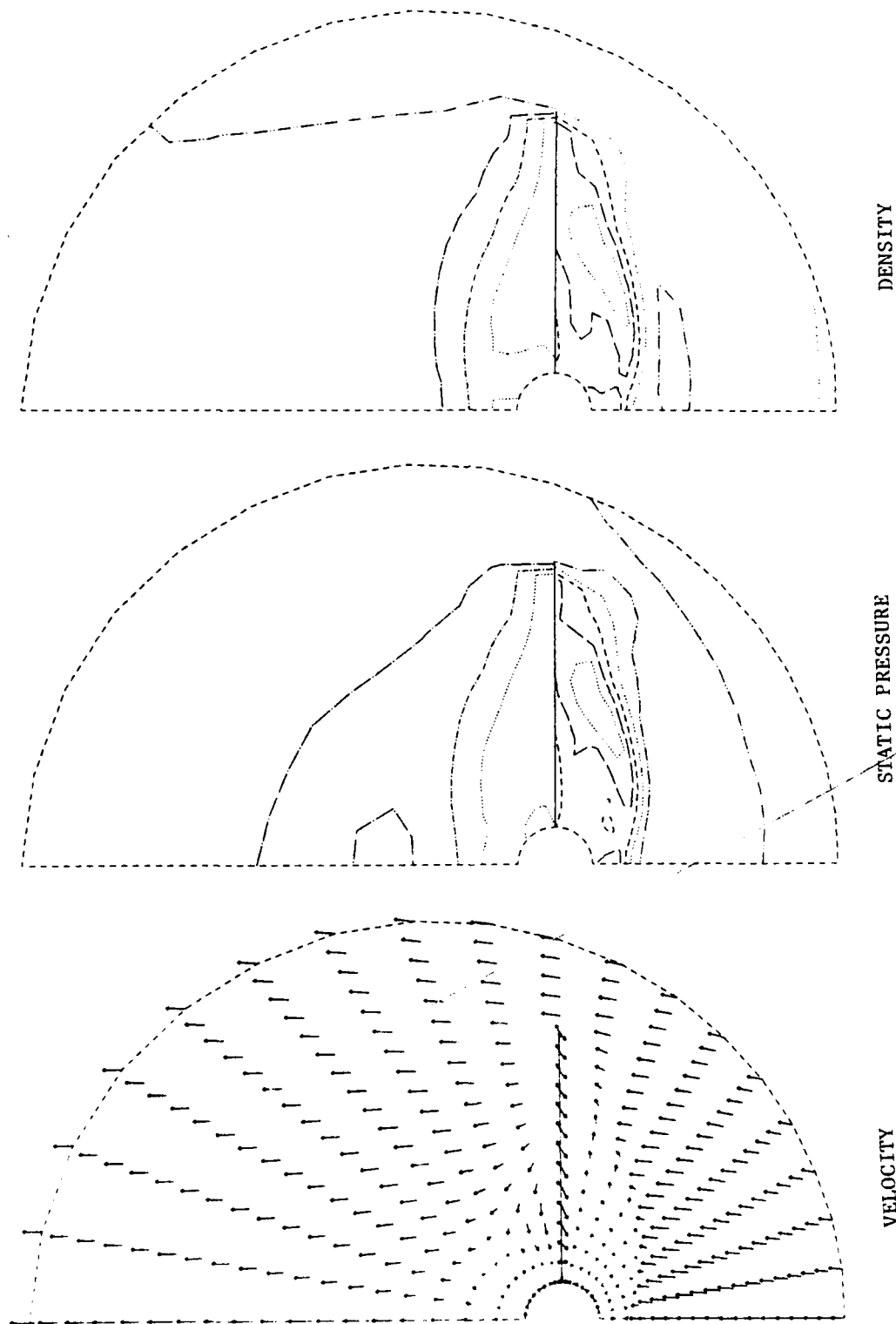


Figure 18. Calculated crossflow field for the body-wing-tail configuration of Ref. 22,  $M = 2.0$ ,  $\alpha = 10^\circ$ .  
a) This station is upstream of the wing trailing edge.



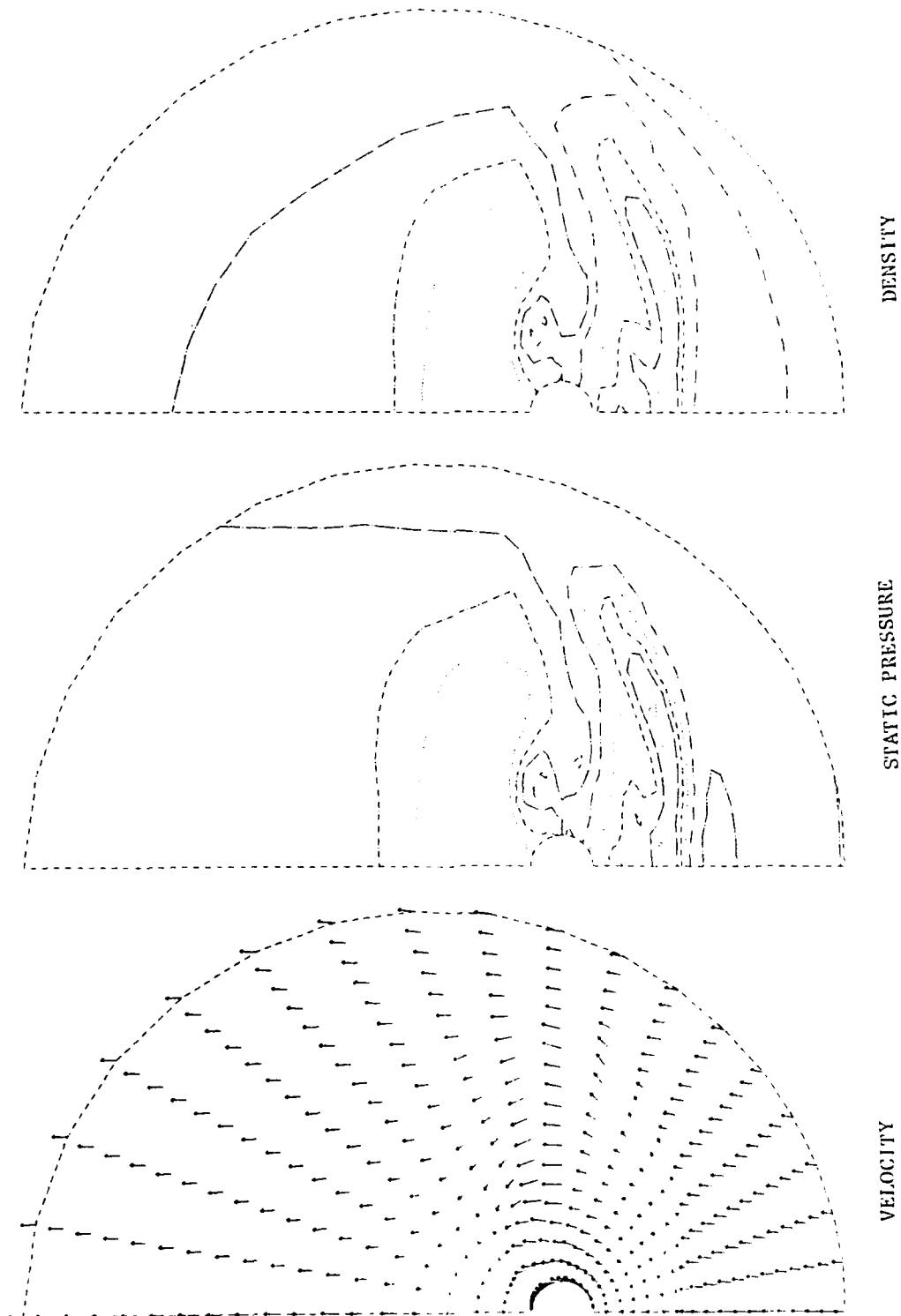


Figure 18. Continued  
b) This station is upstream of the tail.

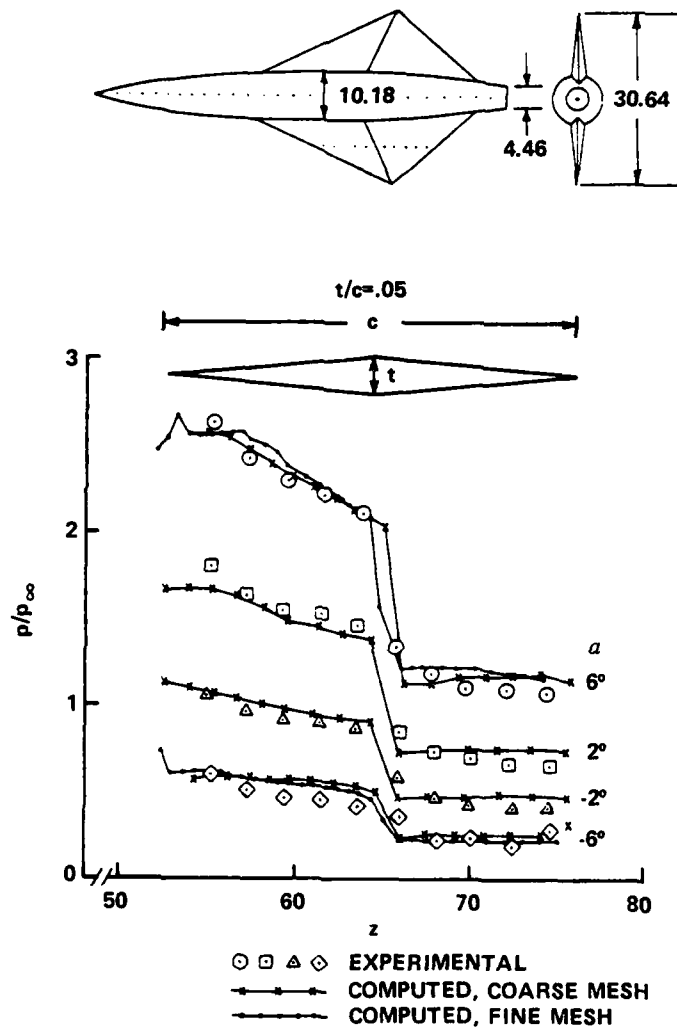


Figure 19. Calculated and measured fin surface pressures on the thin swept wing configuration of Ref. 14 at  $M = 4.5$ ,  $\alpha = 2^\circ$  and  $6^\circ$

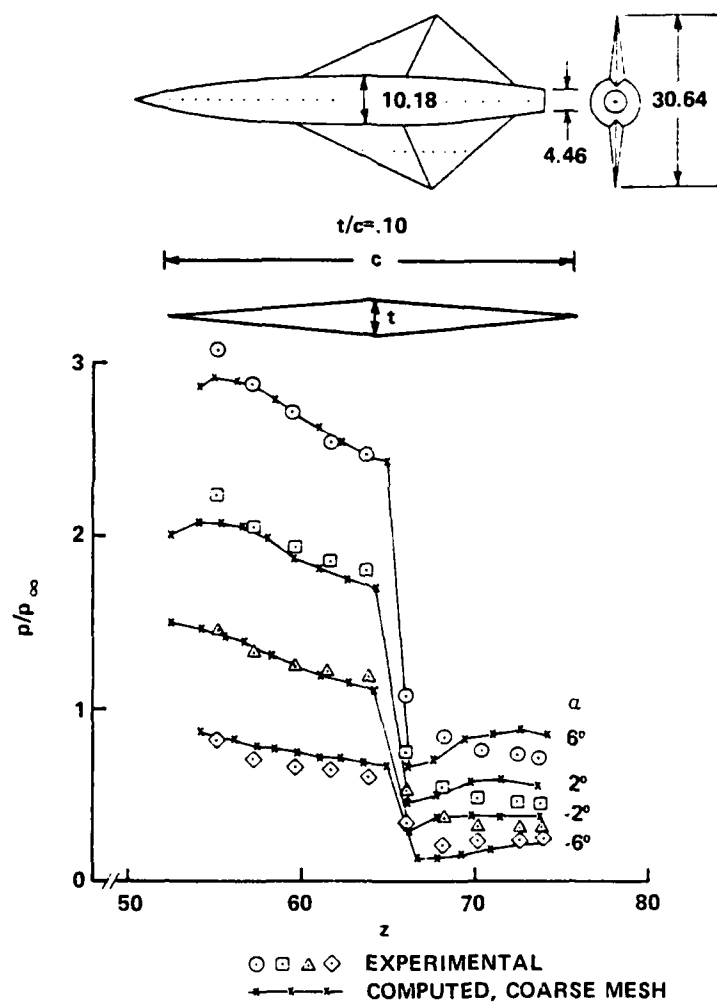


Figure 20. Calculated and measured fin surface pressures on a thick swept wing configuration of Ref. 14 at  $M = 4.5$ ,  $\alpha = 2^\circ$  and  $6^\circ$

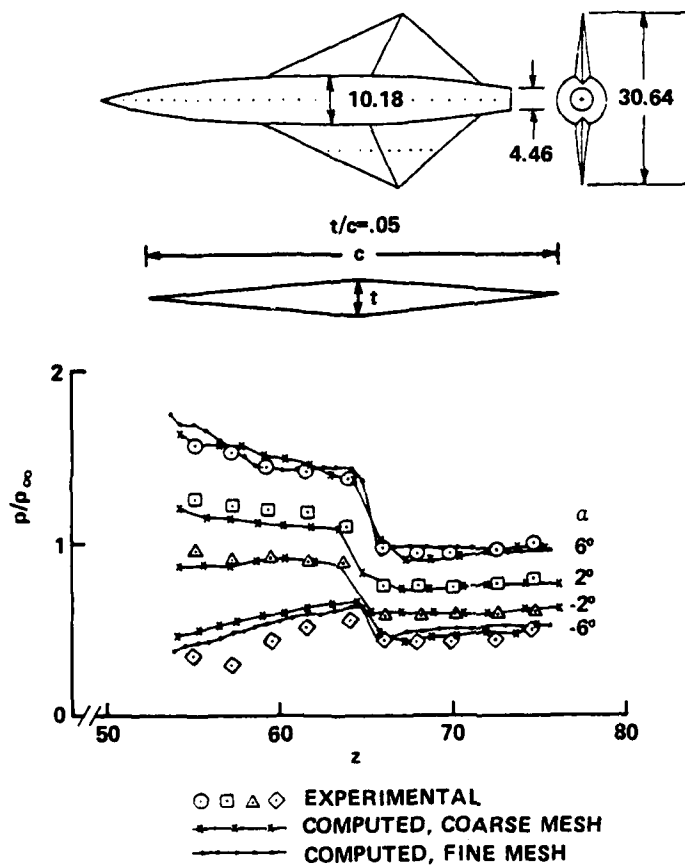


Figure 21. Calculated and measured fin surface pressures on a thin swept wing configuration of Ref. 14 at  $M = 2.5$ ,  $\alpha = 2^\circ$  and  $6^\circ$

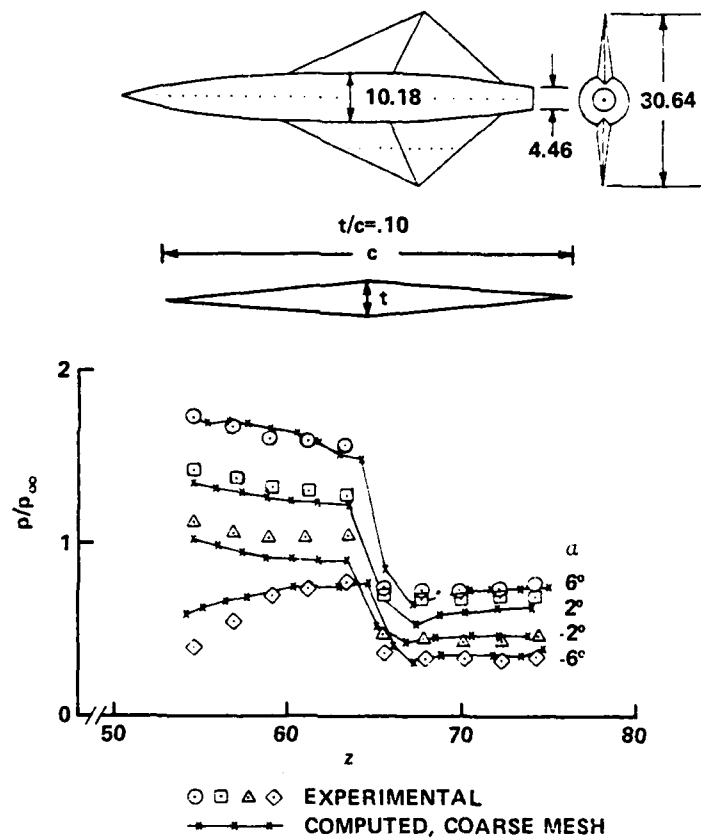


Figure 22. Calculated and measured fin surface pressures on a thick swept wing configuration of Ref. 14 at  $M = 2.5$ ,  $\alpha = 2^\circ$  and  $6^\circ$

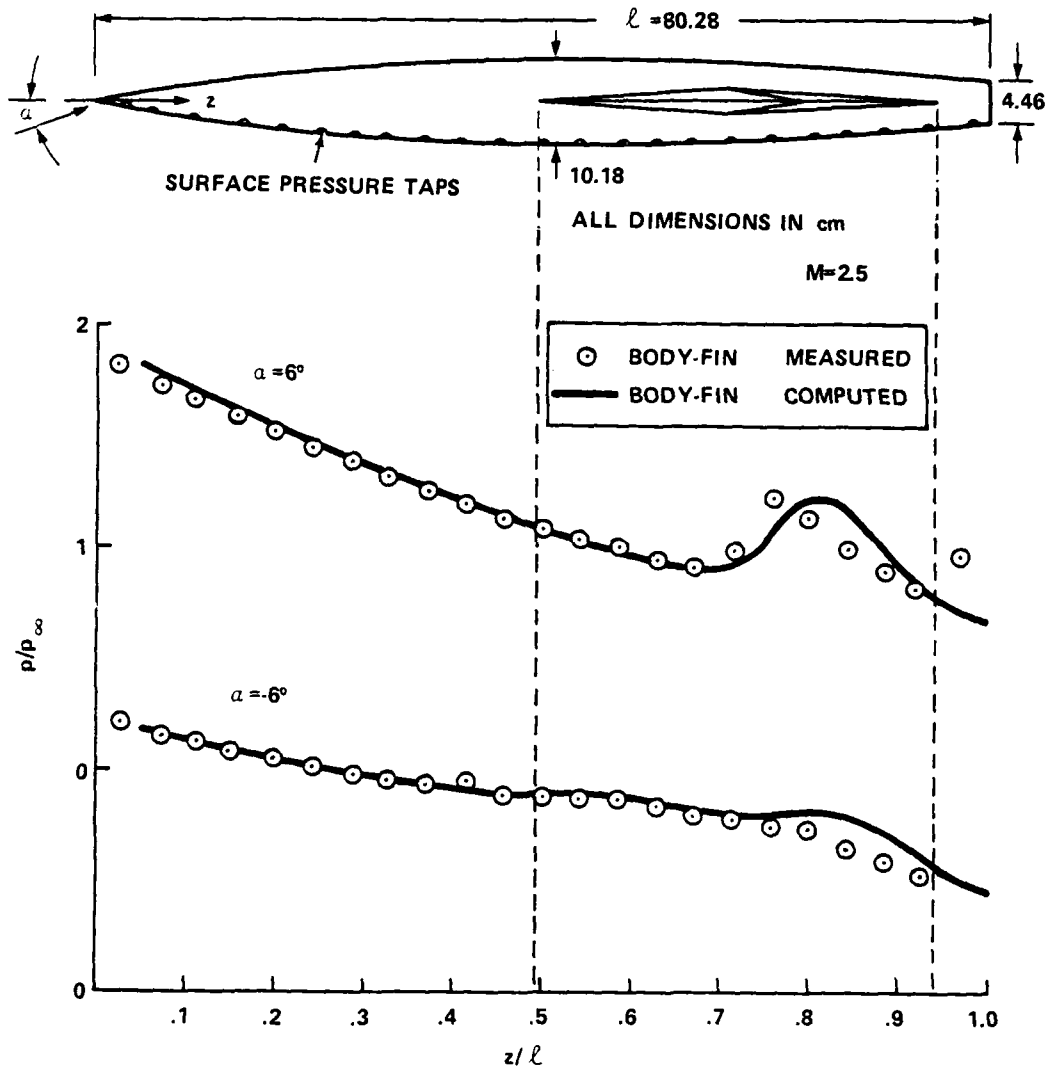


Figure 23. Calculated and measured body surface pressures on the thick swept wing configuration of Ref. 14 at  $M = 2.5$ ,  $\alpha = 2^\circ$  and  $6^\circ$

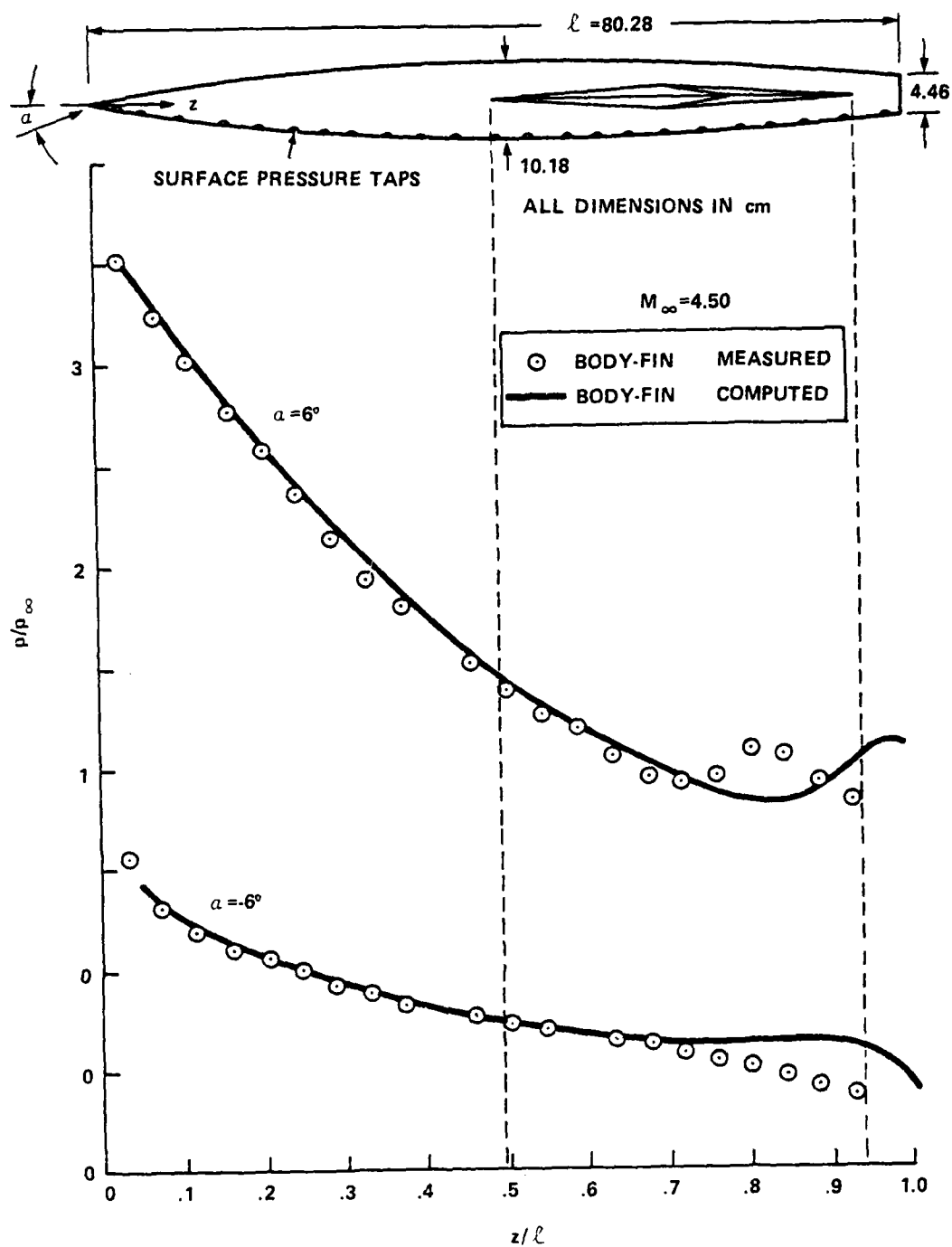


Figure 24. Calculated and measured body surface pressures on the thick swept wing configuration of Ref. 14 at  $M = 4.5$ ,  $\alpha = 2^\circ$  and  $6^\circ$

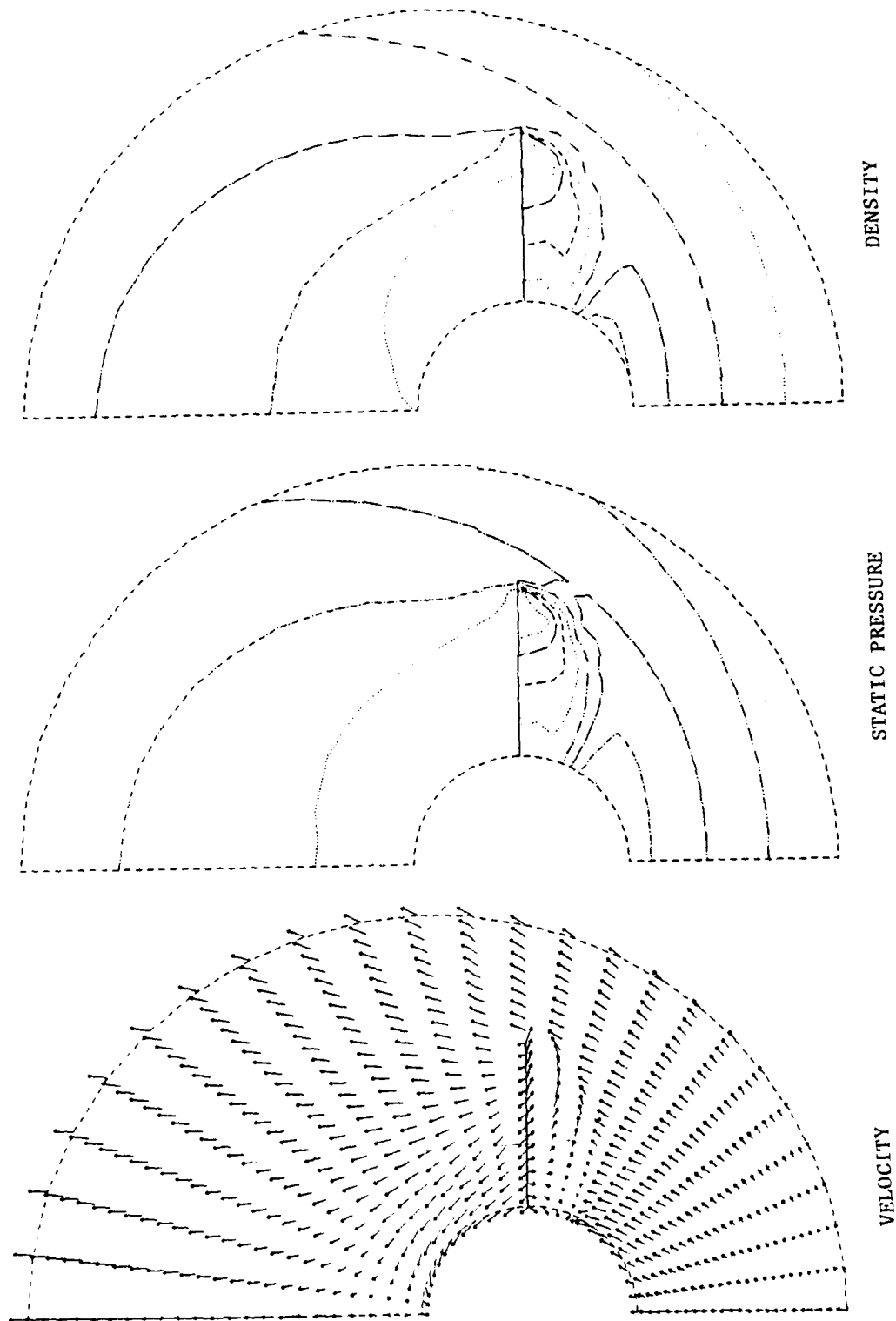


Figure 25. Calculated crossflow field on the thin swept wing configuration of Ref. 14 at  $M = 4.5$ ,  $\alpha = 6^\circ$ ,  $Z = 62$



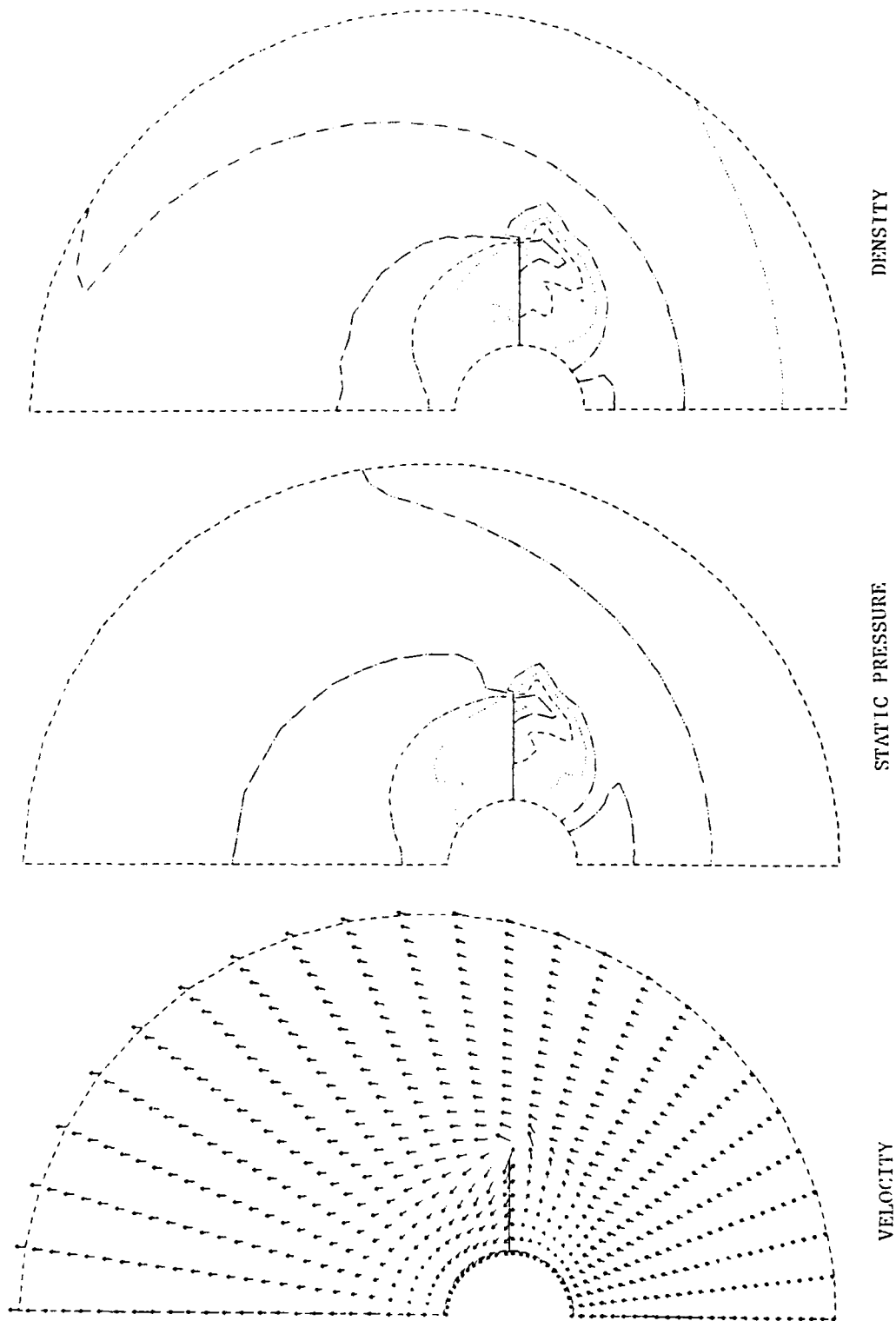


Figure 26. Calculated crossflow field on the thin swept wing configuration of Ref. 14 at  $M = 2.5$ ,  $\alpha = 6^\circ$ ,  $Z = 62$

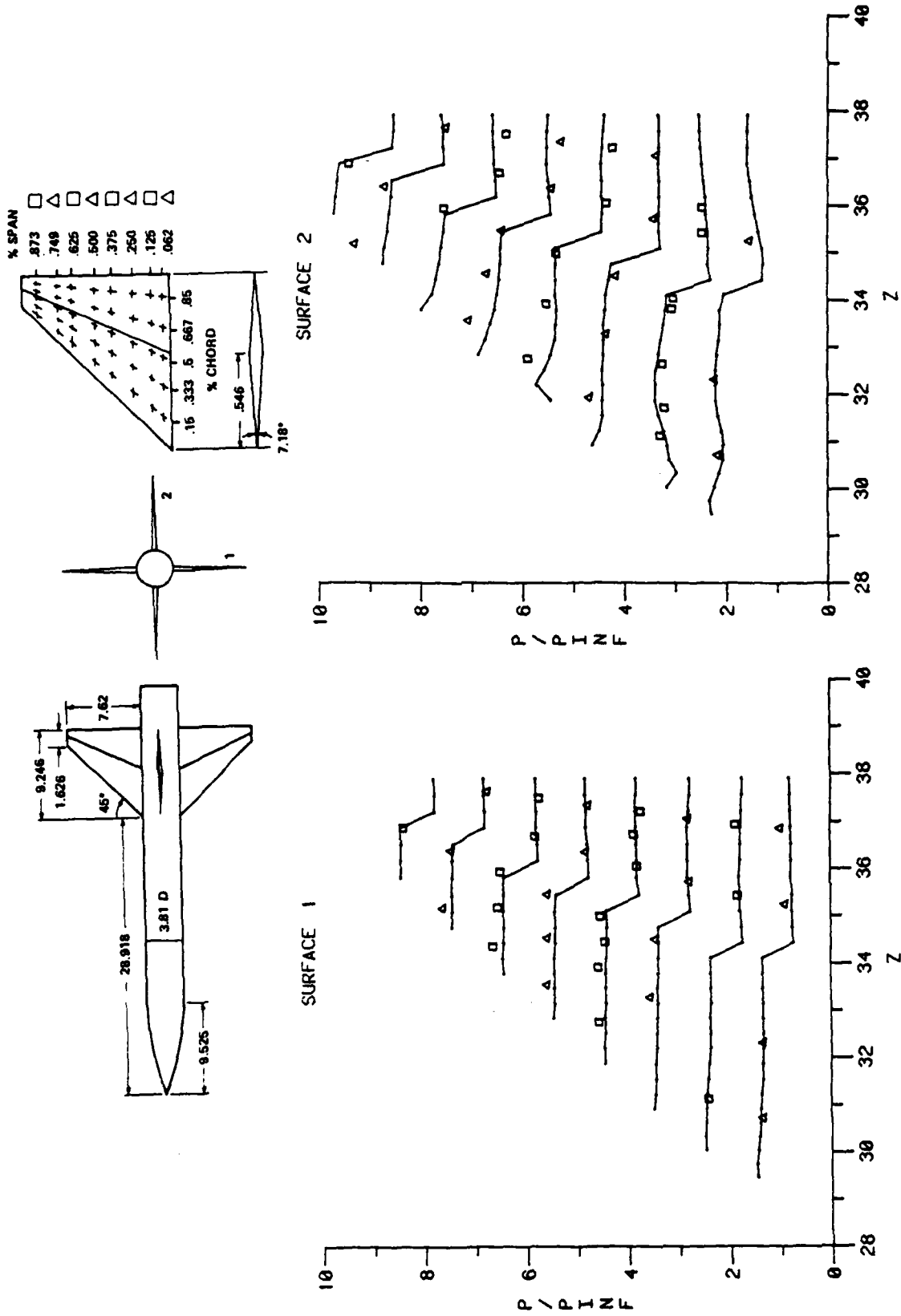
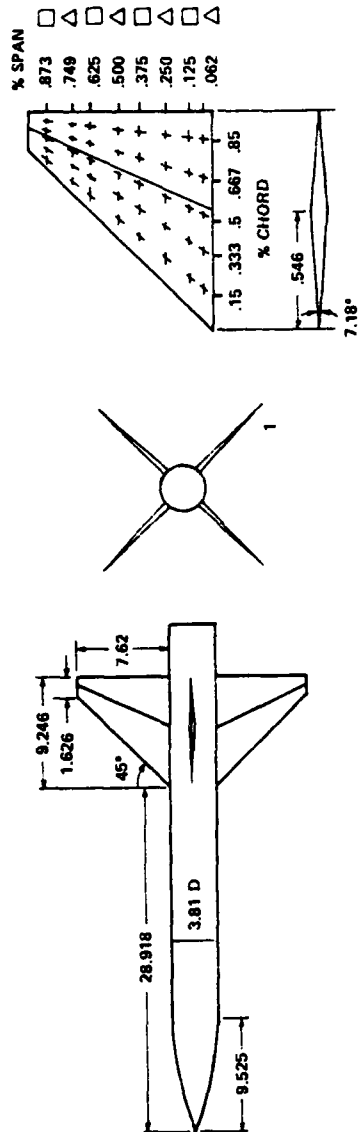


Figure 27. Calculated and measured wing surface pressures on the delta wing configuration of Ref. 23, in the "4" roll position at  $M = 2.7$ ,  $\alpha = 10^\circ$ . (Zero reference shifted by 1.0 for each successive curve.)



SURFACE 1

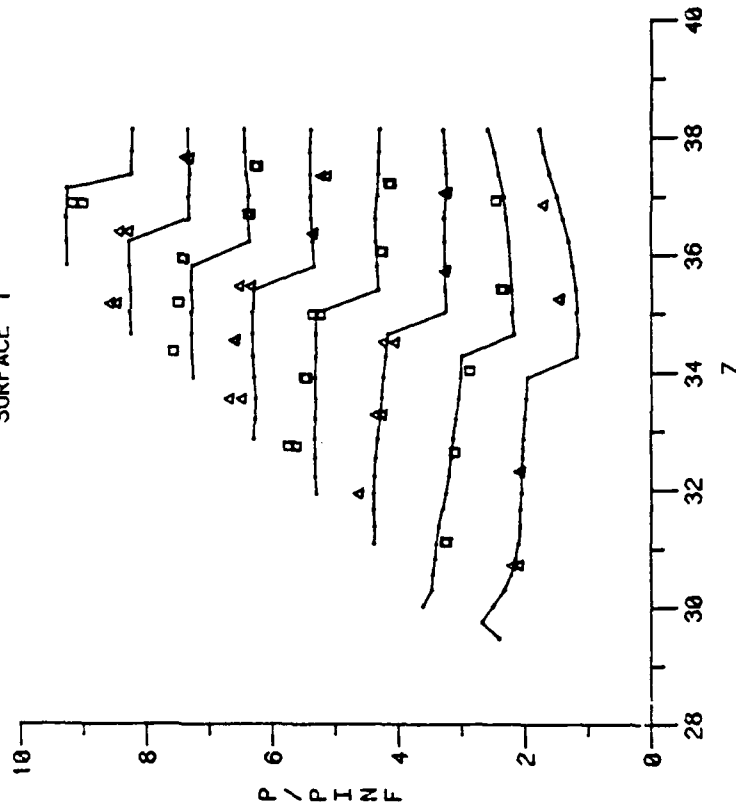


Figure 28. Calculated and measured wing surface pressures on the delta wing configuration of Ref. 23, in the "x" roll position at  $M = 2.7$ ,  $\alpha = 10^\circ$ . (Zero reference shifted by 1.0 for each successive curve.)

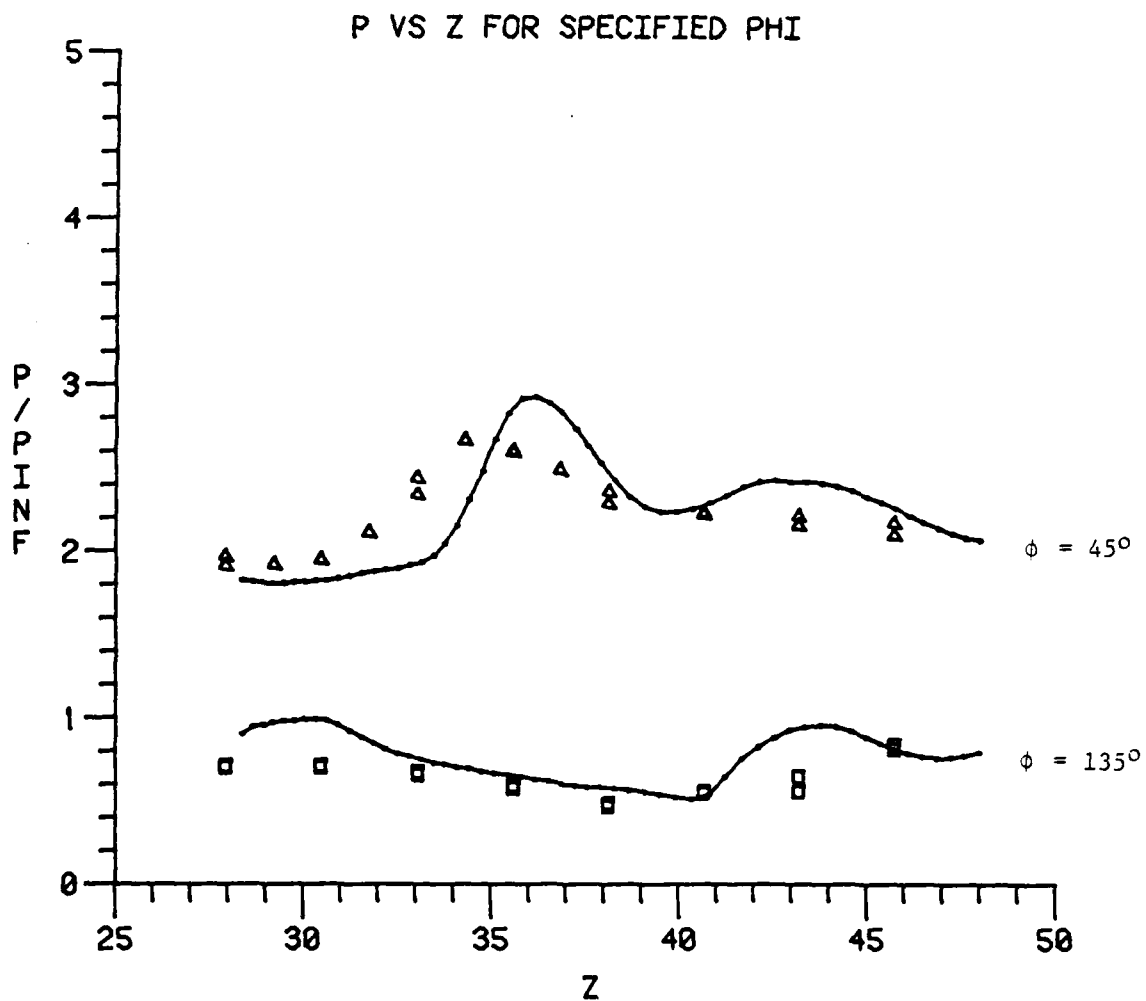
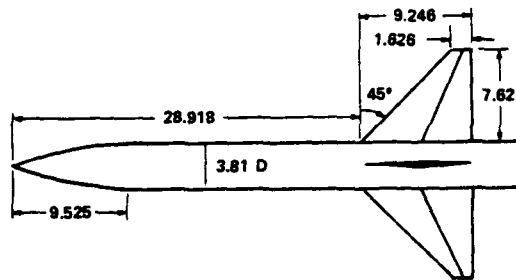


Figure 29. Calculated and measured body surface pressures on the delta wing configuration of Ref. 23, in the "+" roll position at  $M = 2.7$ ,  $\alpha = 10^\circ$

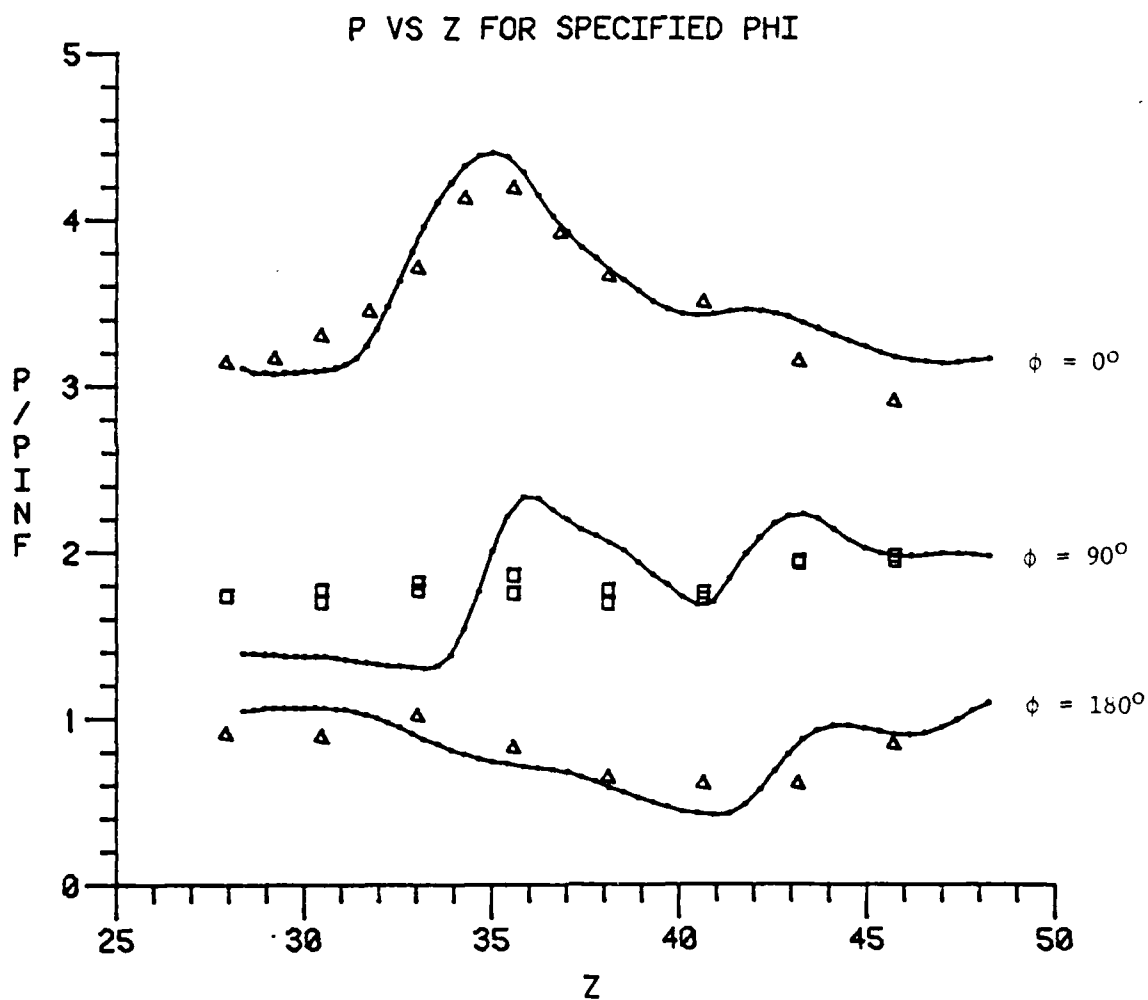
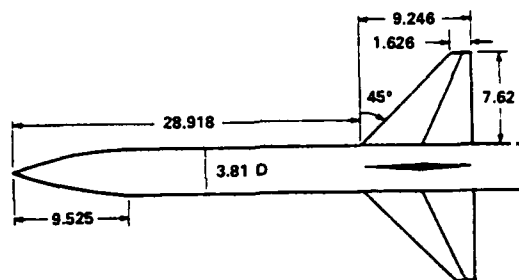


Figure 30. Calculated and measured body surface pressures on the delta wing configurations of Ref. 23, in the "x" roll position at  $M = 2.7$ ,  $\alpha = 10^\circ$

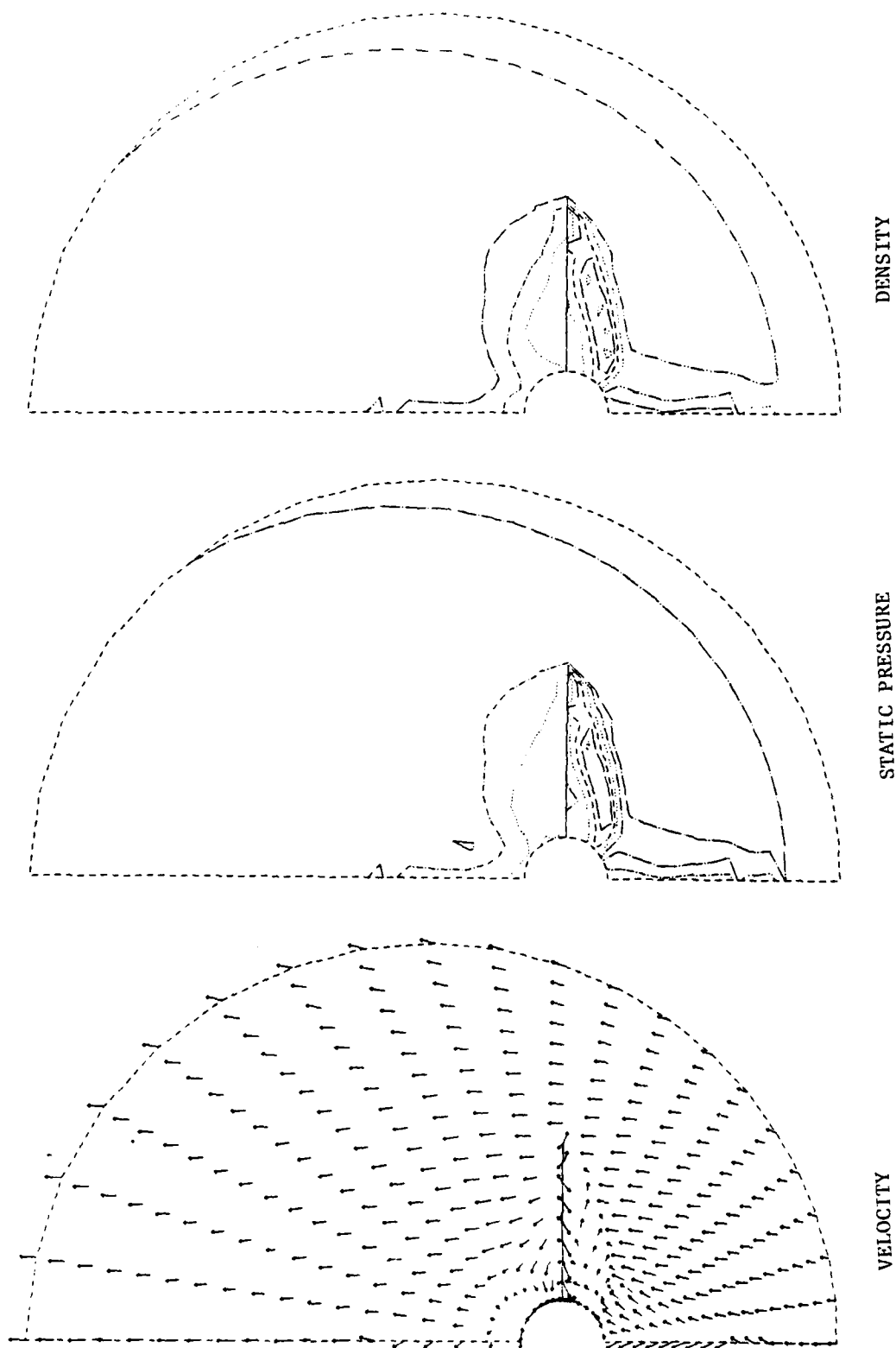


Figure 31. Calculated crossflow field on the delta wing configuration of Ref. 23, in the "4" roll position at  $M = 2.7$ ,  $\alpha = 10^\circ$ ,  $Z = 36.5$

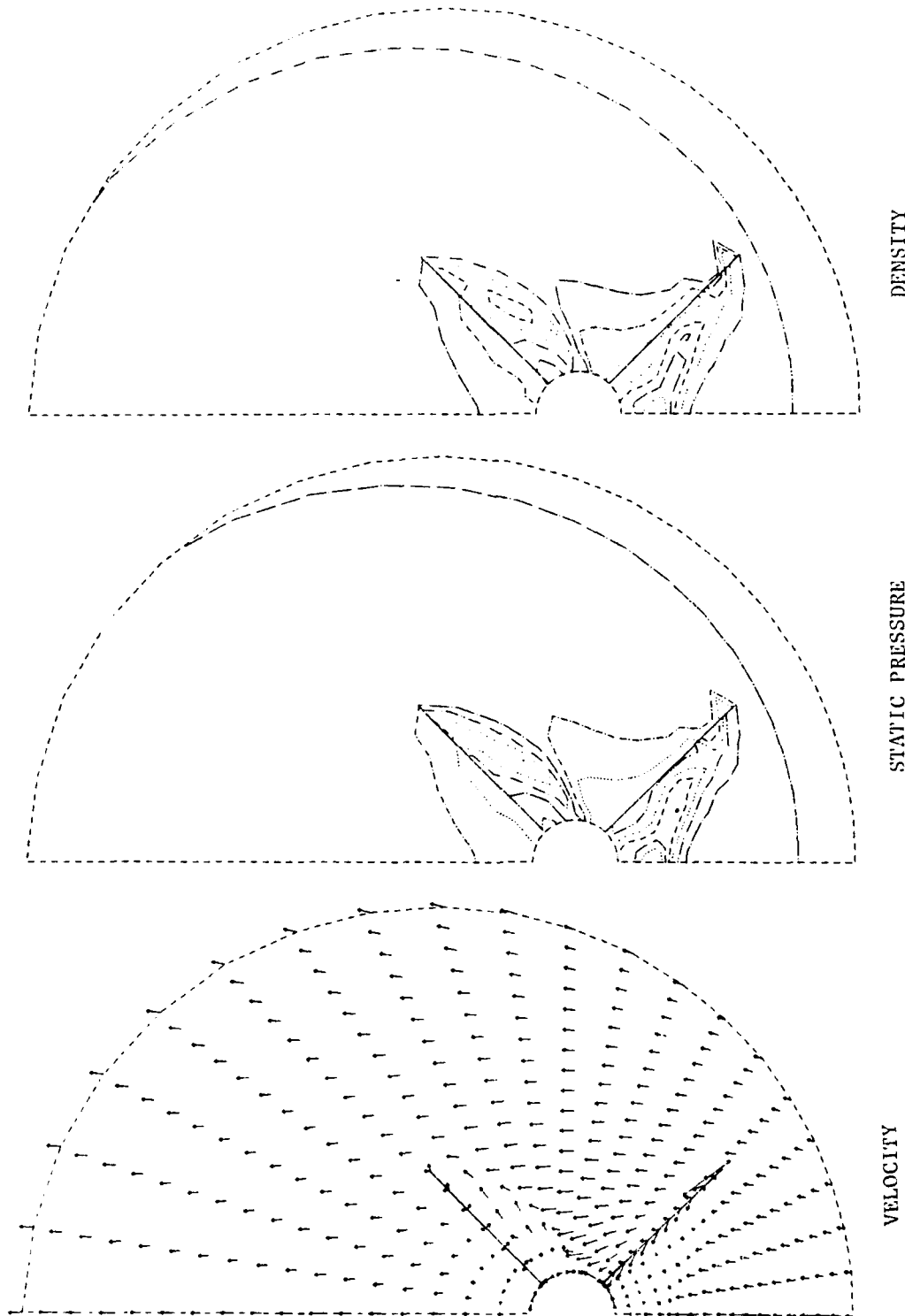


Figure 32. Calculated crossflow field on the delta wing configuration of Ref. 23, in the "X" roll position at  $M = 2.7$ ,  $\alpha = 10^\circ$ ,  $Z = 36.5$

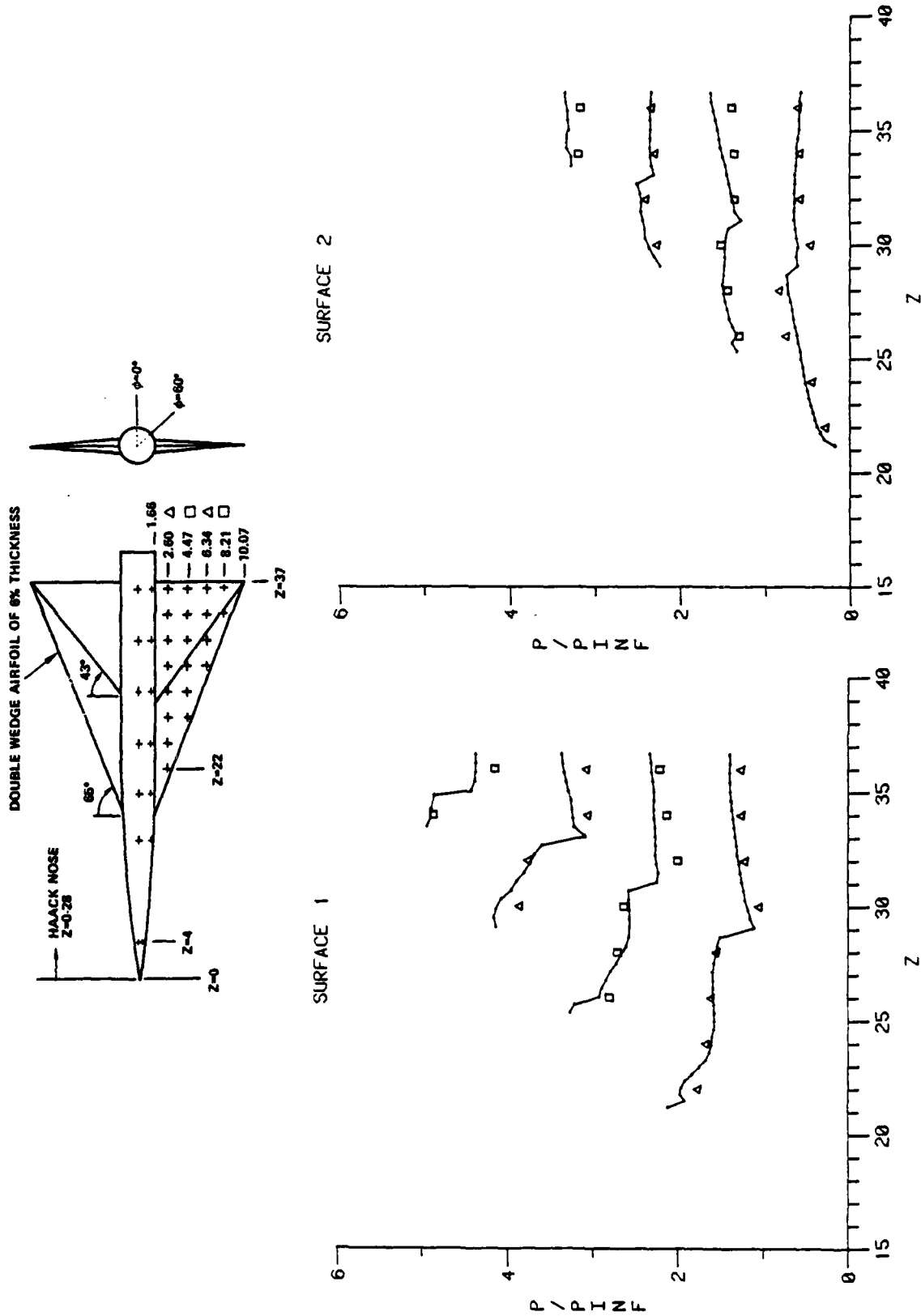


Figure 33. Calculated and measured wing surface pressures on the swept wing configuration of Ref. 24 at  $M = 2.3$  and  $\alpha = 8.8^\circ$ . (Zero reference shifted by 1.0 for each successive curve.)



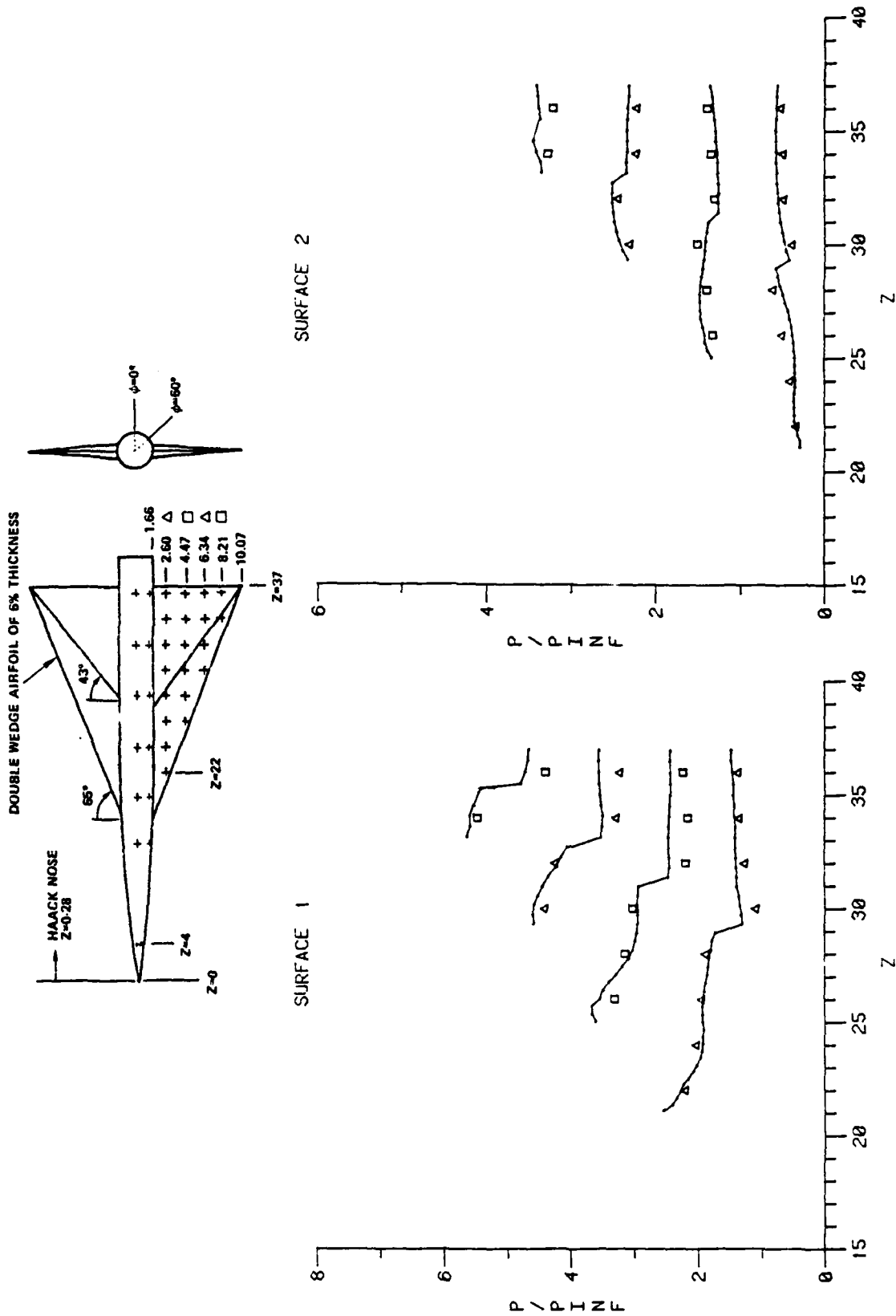


Figure 34. Calculated and measured wing surface pressures on the swept wing configuration of Ref. 24 at  $M = 2.96$  and  $\alpha = 8.6^\circ$ . (Zero reference shifted by 1.0 for each successive curve.)

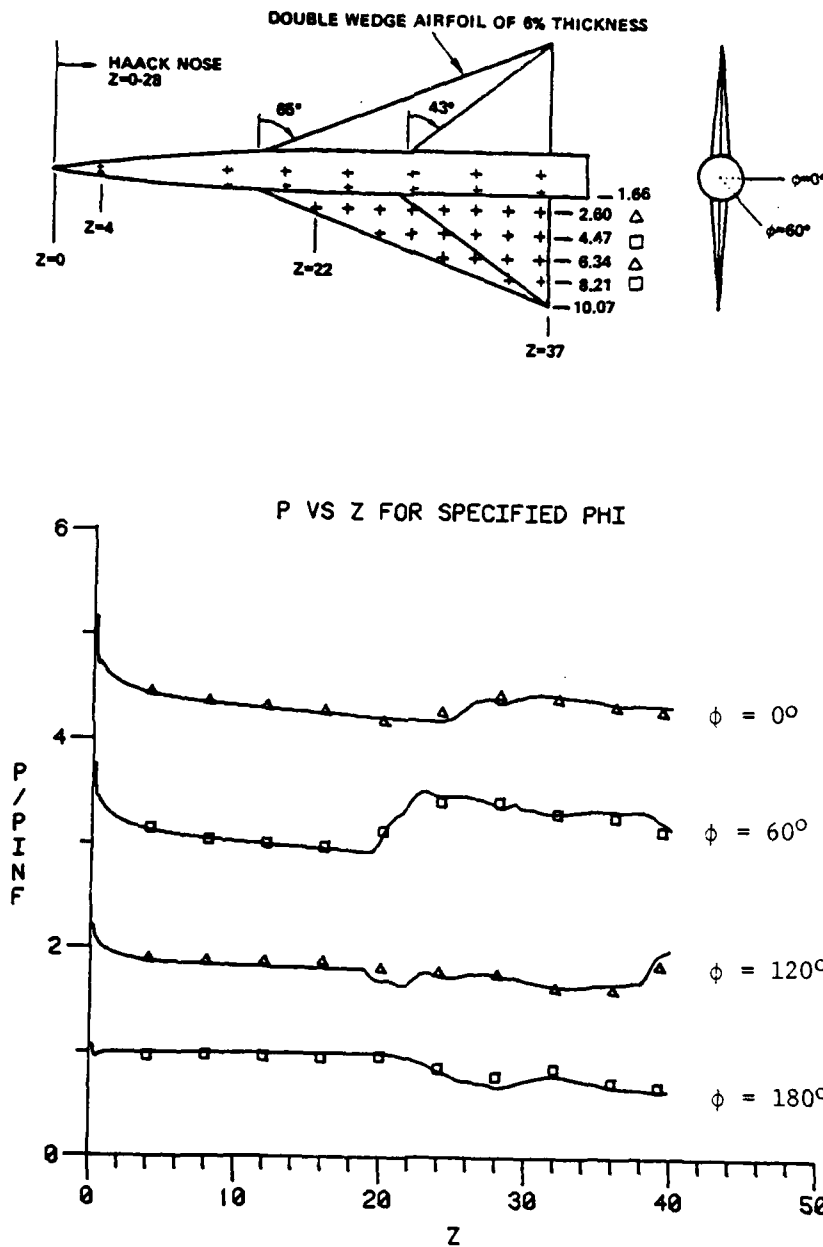


Figure 35. Calculated and measured body surface pressures on the swept wing configuration of Ref. 24 at  $M = 2.3$  and  $\alpha = 8.9^\circ$ . (Zero reference shifted by 1.0 for each successive curve.)

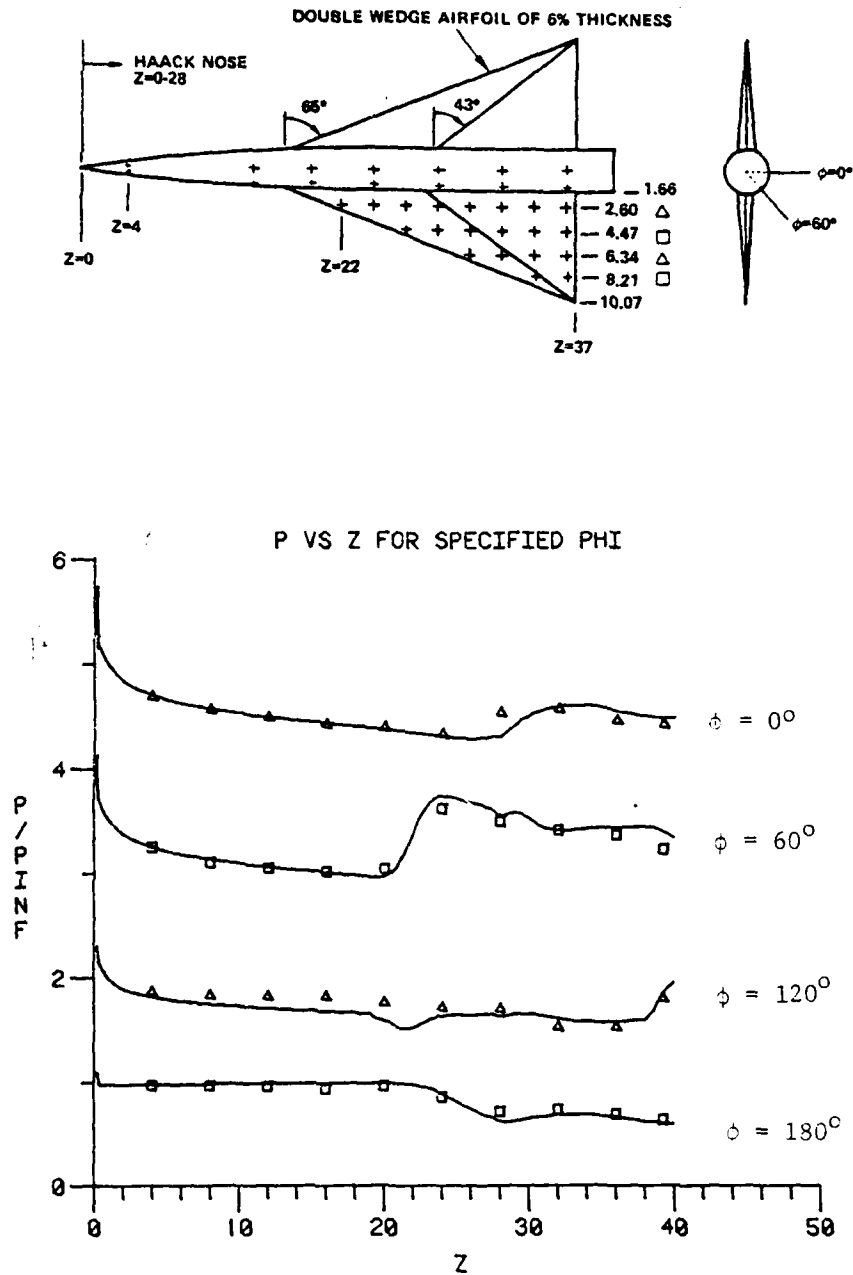


Figure 36. Calculated and measured body surface pressures on the swept wing configurations of Ref. 24 at  $M = 2.96$  and  $\chi = 8.6^\circ$ . (Zero reference shifted by 1.0 for each successive curve.)

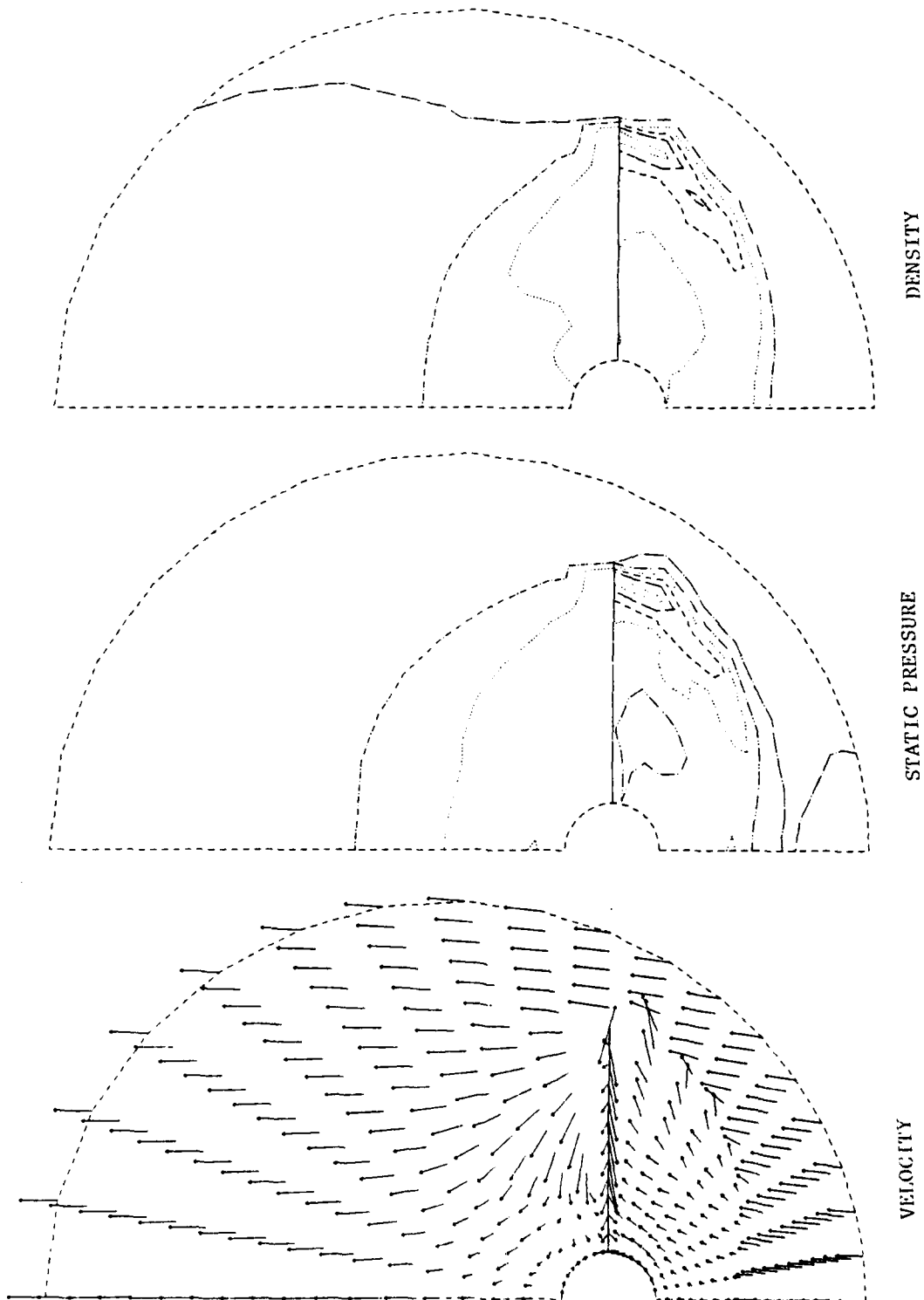


Figure 37. Calculated crossflow plane flow field on the delta wing configuration of Ref. 24 at  $M = 2.3$  and  $\alpha = 8.8^\circ$ ,  $Z = 36$

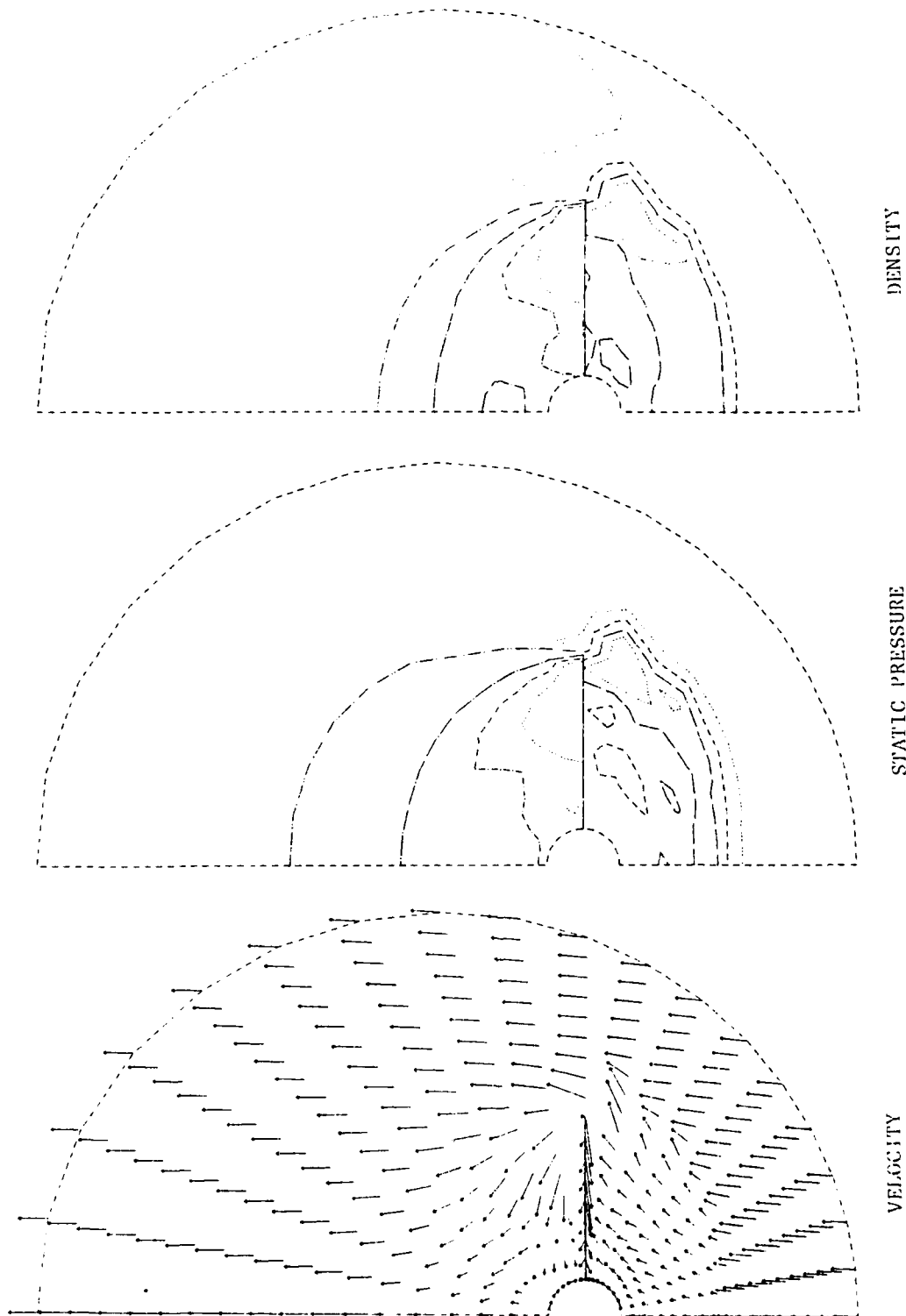


Figure 38. Calculated crossflow plane flow field on the delta wing configuration of Ref. 24 at  $M = 2.96$  and  $\alpha = 8.6^\circ$ ,  $Z = 36$

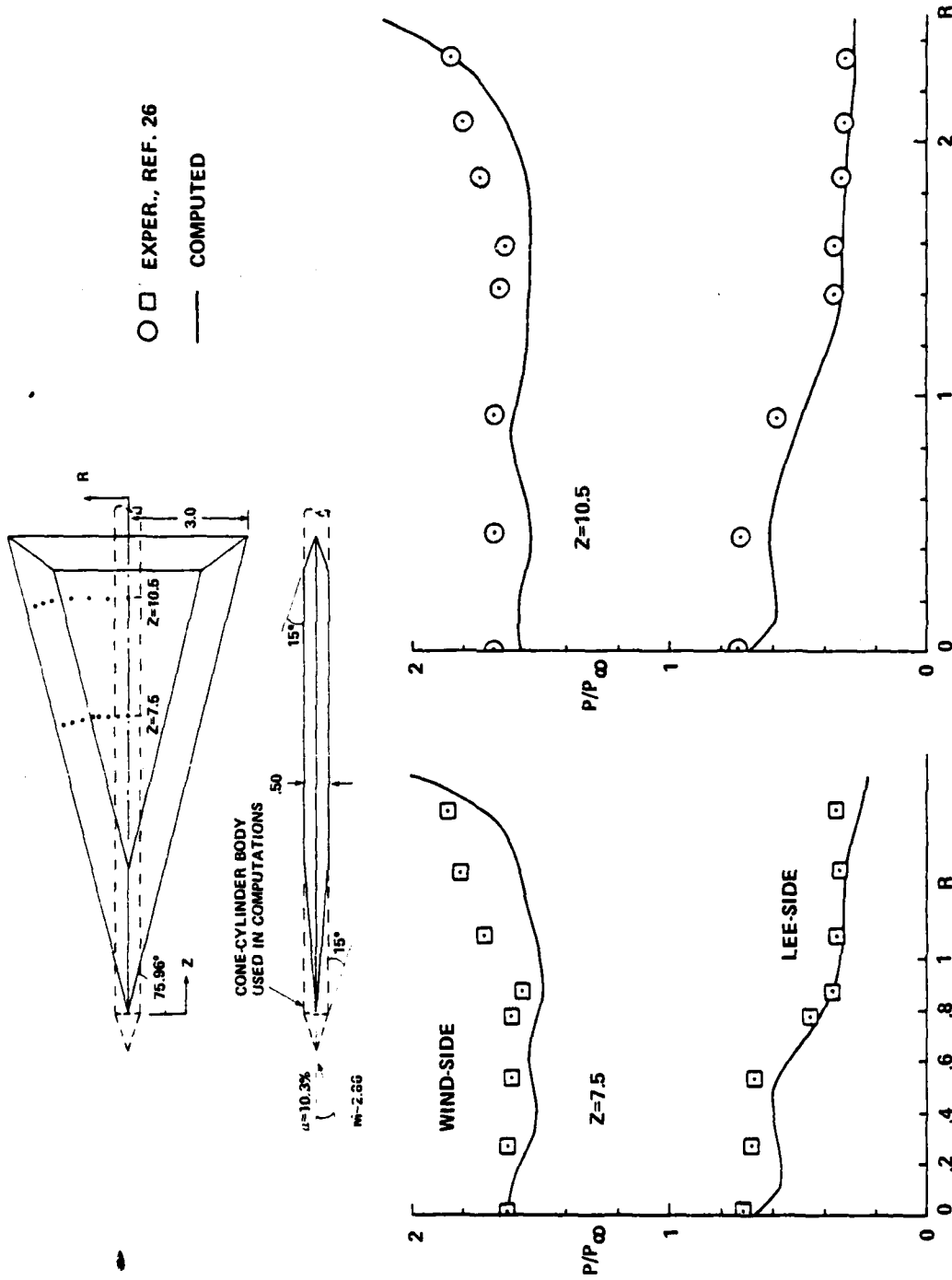


Figure 39. Calculated and measured surface pressures on the delta wing of Ref. 26 at  $M = 2.86$  and  $\alpha = 10.3^\circ$

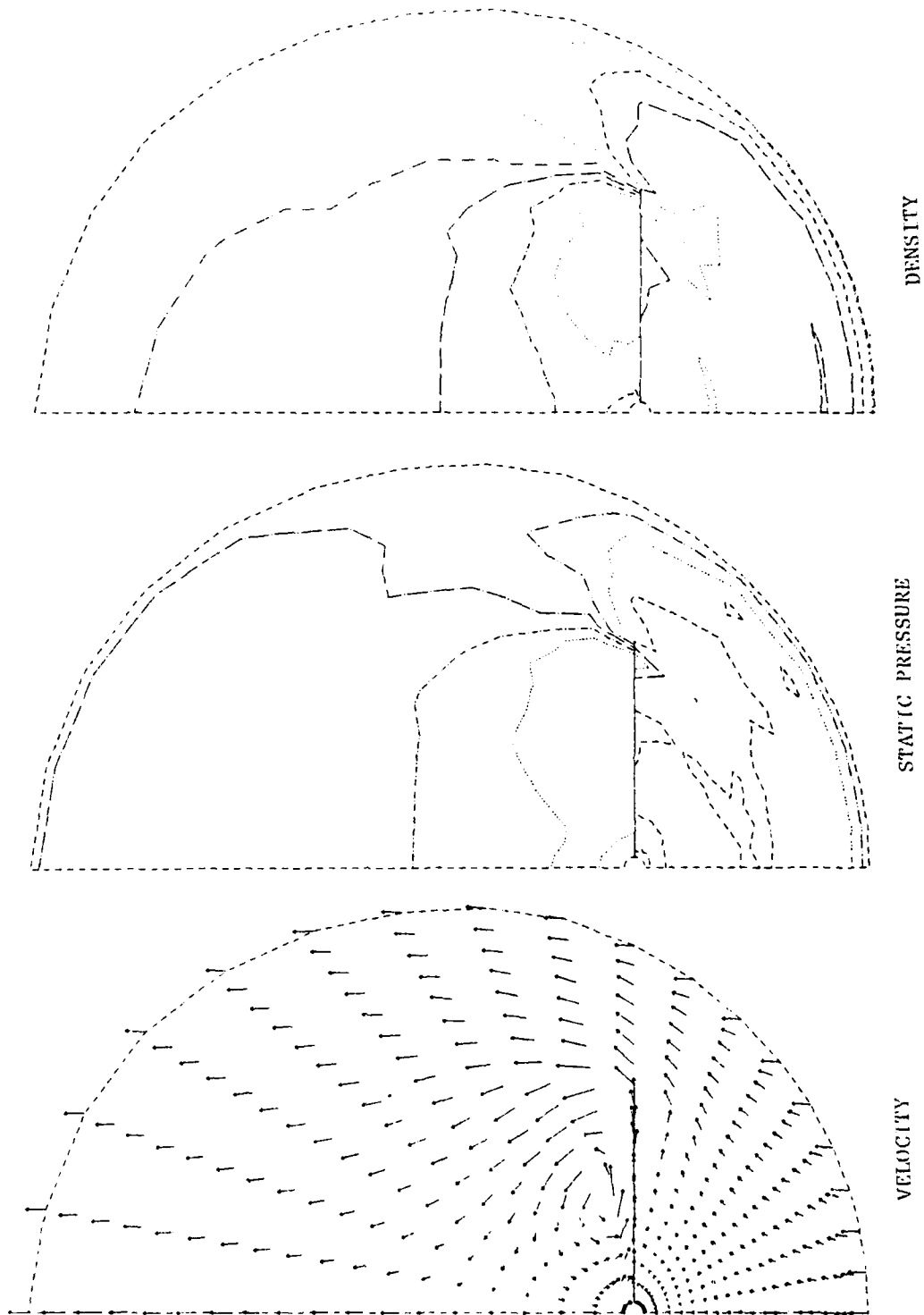


Figure 40. Calculated crossflow plane flow field on the delta wing configuration of Ref. 26 at  $M = 2.86$  and  $\alpha = 10.3^\circ$ . The illustrated station is upstream of the trailing edge.

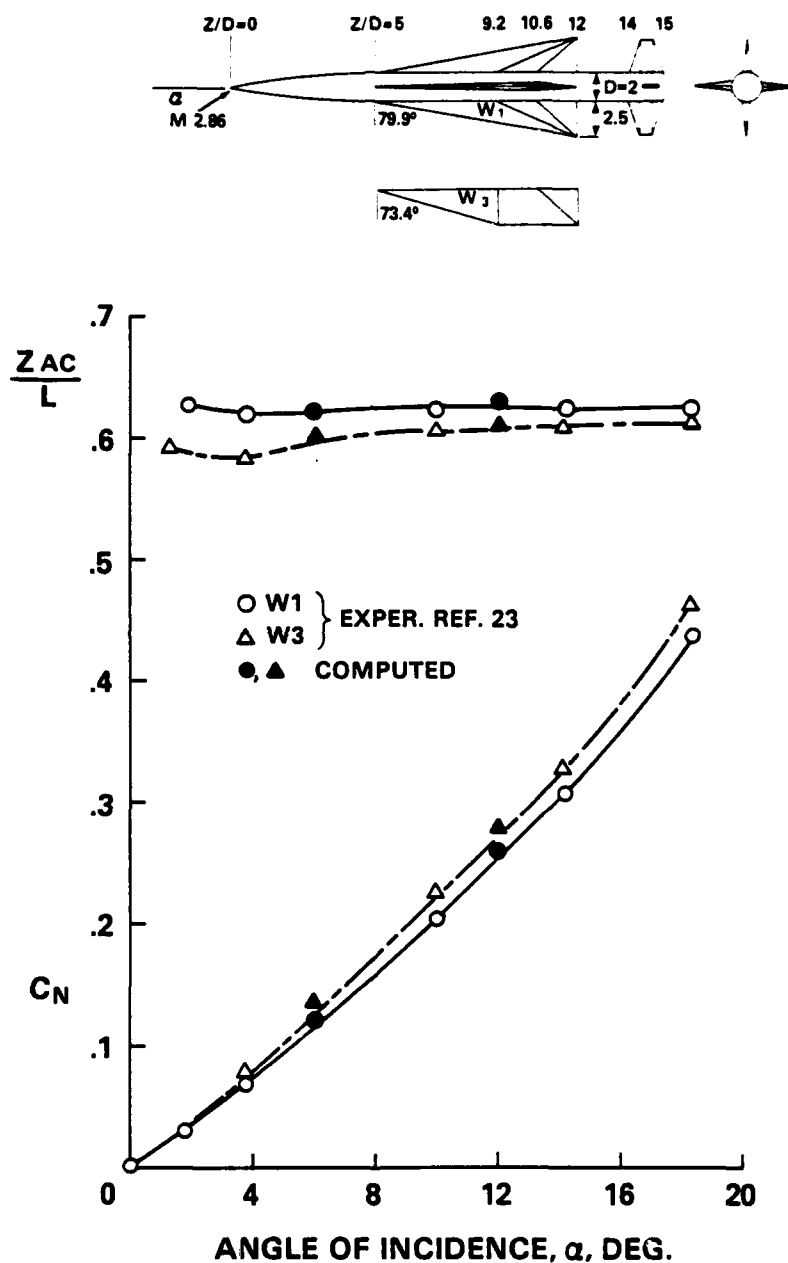


Figure 41. Calculated and measured normal force coefficient and center of pressure for two wing-body-tail configurations of Ref. 27 at  $\alpha = 6^\circ$  and  $12^\circ$ ,  $M = 2.86$  and tail undeflected



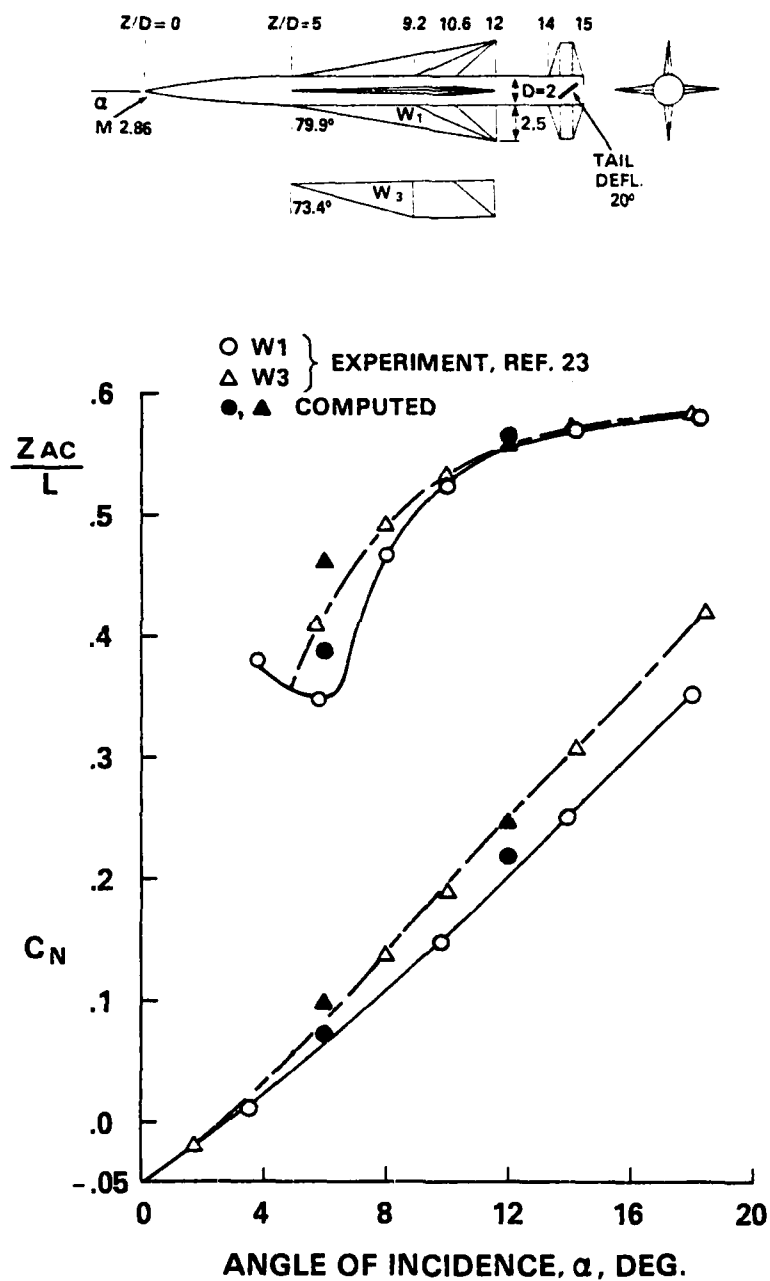


Figure 42. Calculated and measured normal force coefficient and center of pressure for two wing-body-tail configurations of Ref. 27 at  $\alpha = 6^\circ$  and  $12^\circ$ ,  $M = 2.86$  and tail deflected to  $20^\circ$

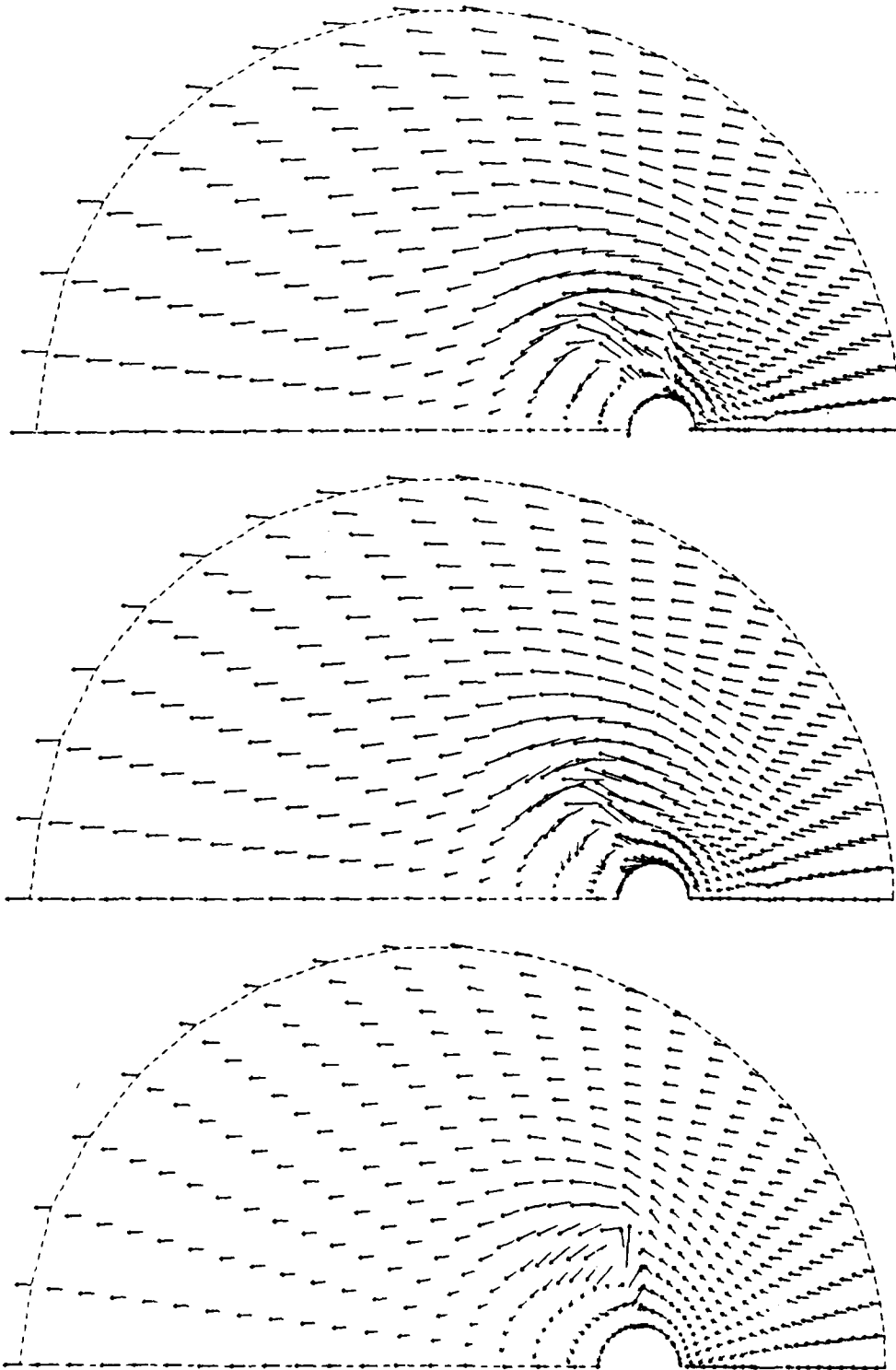


Figure 43. Calculated crossflow plane flow field for the W1 body-wing-tail configuration of Ref. 27 at  $M = 2.86$  and  $\alpha = 12^\circ$ . The forward plane is downstream of the wing trailing edge, the middle station is upstream of the tail leading edge, the rear station is downstream of the tail trailing edge

## REFERENCES

1. Thomas, P. D., Vinokur, M., Bastianon, R., and Conti, R. J., "Numerical Solution for Three-Dimensional Inviscid Supersonic Flow," AIAA J., Vol. 10, No. 7, 1972, pp. 887-894.
2. Moretti, G., Grossman, B., and Marconi, F., "A Complete Numerical Technique for the Calculation of Three-Dimensional Inviscid Supersonic Flow," AIAA Paper 72-192, San Diego, Calif., 1972.
3. Marconi, F. and Salas, M., "Computation of Three Dimensional Flows About Aircraft Configurations," Computers and Fluids, Vol. 1, 1973, pp. 185-195.
4. Kutler, P., Reinhardt, W. A., and Warming, R. F., "Multishocked, Three-Dimensional Supersonic Flowfields with Real Gas Effects," AIAA J., Vol. 11, No. 5, 1973, pp. 657-664.
5. Kyriss, C. L. and Harris, T. B., "A Three-Dimensional Flow Field Computer Program for Manueuvering and Ballistic Re-entry Vehicles," Tenth USN Sym. on Aeroballistics, Jul, 1975.
6. Marconi, F., Salas, M., and Yaeger, L., "Development of a Computer Code for Calculating the Steady Super/Hypersonic Inviscid Flow Around Real Configurations, Vol. I-Computational Techniques", NASA CR 2675, Apr 1976.
7. Solomon, J. M., Ciment, M., Ferguson, R. E., Bell, J. B., "Inviscid Flowfield Calculations for Reentry Vehicles with Control Surfaces," AIAA J., Vol. 15, No. 12, 1977, pp. 1742-1749.
8. Moretti, G., "Conformal Mappings for Computation of Steady, Three-Dimensional, Supersonic Flows," Numerical/Lab. Computer Methods in Fluid Dynamics, ASME, 13, 1976.
9. Hindman, R. S. Kutler, P., Anderson, D., "A Two-Dimensional Unsteady Euler-Equation Solver for Flow Regions with Arbitrary Boundaries," AIAA Paper 1465, Williamsburg, VA., 1979.
10. Solomon, J. M., Ciment, M., Ferguson, R. E., Bell, J. B., and Wardlaw, A.B.Jr., "A Program for Computing Steady Inviscid Three-Dimensional Supersonic Flow on Reentry Vehicles, Vol. 1: Analysis and Programming," Naval Surface Weapons Center/White Oak, Silver Spring, MD., NSWC/WOL TR 77-28, Feb 1977.
11. Wardlaw, A. B. Jr., Hackerman, L. B. and Baltakis, F. P., "An Inviscid Computational Method for Supersonic Missile Type Bodies-Program Description and User's Guide," NSWC/WOL TR 81-459, Mar 1982.
12. Kentzer, C. P., "Discretization of Boundary Conditions on Moving Discontinuities," Proc. of the 2nd Inter. Conf. on Num. Methods in Fluid Dynamics, Lect. Notes in Physics, Vol. 8, Springer-Verlag, 1971, pp. 108-113.

## REFERENCES (Cont.)

13. Wardlaw, A. B. Jr., Solomon, J. M. and Baltakis, F. P., "Supersonic Inviscid Flow Computations of Missile Type Bodies," AIAA Paper No. 80-0271, Jan 1980.
14. Jackson, C. M. Jr., and Sawyer, W. C., "A Method for Calculating the Aerodynamic Loading on Wing-Body Combinations at Small Angles of Attack in Supersonic Flow," NASA TN D-6441, 1971.
15. Harten, A. and Zwas, G. "Switched Numerical Shuman Filters for Shock Calculations," Journal of Engineering Mathematics, 6, 2, April 1972, pp. 207-216.
16. Klopfer, G. H. and Nielsen, J. N. "Euler Solutions of the Body Vortices of Tangent Ogive Cylinders at High Angles of Attack and Supersonic Speeds," AIAA Paper 81-0361.
17. Wardlaw, A. B. Jr., "High Angle-of-Attack Missile Aerodynamics" AGARD Lecture Series No. 98, Missile Aerodynamics, AGARD-LS-98, 1979.
18. Wardlaw, A. B. Jr., Solomon, J. M., Baltakis, F. P. and Hackerman, L. B., "An Inviscid Computational Method for Tactical Missile Configurations," Naval Aeroballistic Committee Symposium, NSRDC, May 1981.
19. Wardlaw, A. B. Jr., Solomon, J. M. and Baltakis, F. P., "Supersonic Inviscid Flowfield Computations of Missile Type Bodies," AIAA Journal, 19, 7, pp. 899-906, July 1981.
20. Oberkampf, W. L. and Bartel, T. J., "Supersonic Flow Measurements in the Body Vortex Wake of an Ogive Cylinder," AFATL-TR-78-127, Nov 1978.
21. Lamb, M., Sawyer, W. C., Wassum, D. L., Babb, C. D., "Pressure Distributions on Three Different Cruciform Aft-Tail Control Surfaces of a Wingless Missile at Mach 1.60, 2.36 and 3.780," Vol. II and III, NASA TM 80097, Aug 1979.
22. Jorgensen, L. H. and Nelson, E. R., "Experimental Aerodynamic Characteristics for Slender Bodies with Thin Wings and Tail," NASA TMX-3310, Mar 1976.
23. Stallings, R. L., Lamb, M., Watson, C. B., "Effect of Reynolds Number on Stability Characteristics of a Cruciform Wing-Body at Supersonic Speeds," NASA TP 1683, Jul 1980.
24. Jernell, L. S., "Comparisons of Theoretical and Experimental Pressure Distributions over a Wing-Body Model at Supersonic Speeds," NASA TN D-6480, Sep 1971.
25. Klopfer, G. H., Nielsen, J. N., "Euler Solutions for Wing and Wing-Body Combination at Supersonic Speeds with Leading-Edge Separation," AIAA Paper No. 80-0126, Jan 1980.

REFERENCES

26. Stallings, R. L. and Lamb, M., "Wing Alone Aerodynamic Characteristics for High Angles of Attack at Supersonic Speeds," NASA TP 1889, Jul 1981.
27. Spearman, M. L. and Sawyer, W. C., "Longitudinal Aerodynamic Characteristics at Mach Numbers from 1.6 to 2.86 for Fixed-Span Missile with Three Wing Platforms," NASA TM 74088, Nov 1977.
28. Courant, R. and Hilbert, D., Methods of Mathematical Physics, Vol. II, Interscience Publishers, New York, 1962.

## NOMENCLATURE

$a$	speed of sound
$b(\phi, z)$	body surface radial location (see Figure 1)
$c(\phi, z)$	bow shock location surface radial location (see Figure 1)
$C_X C_Y$	filter constants for the X and Y directions respectively
$(e_r, e_\phi, e_z)$	unit vectors in the $r, \phi, z$ directions
$h$	enthalpy
$H_o$	stagnation enthalpy
$J^{-1}$	$1/\partial(X, Y)/\partial(r, \phi) = 1/X_r \psi_\phi$
$L(z)$	fin edge radial location
$M$	number of $\phi$ planes
$\bar{n}_f$	fin surface normal vector. Vectors on both upper and lower fin surfaces. Vectors on both surfaces have positive $\phi$ components.
$\bar{n}_b$	body surface normal vector
$\bar{n}_c$	vector directed along body fin junction

See  
Figure  
3

## NOMENCLATURE (Cont.)

$\delta$	turning angle of normal flow component
$\delta^*$	maximum possible turning angle with an attached shock
$\tau$	vector tangent to fin leading edge (see Figure 5)
$\theta$	angle between the fin surface tangent plane and the fin plane in the $r$ direction
$v$	angle between the fin surface tangent plane and the fin plane in the $z$ direction
$\rho$	density
$\sigma(r,z)$	fin surface function (see Figure 2)
$\sigma^*$	maximum attached shock angle
$\phi_f$	angular orientation of fin plane (see Figure 2)
$\phi_o$	angle between adjacent symmetry planes (if such planes exist)
$\phi_*$	$\phi_o$ for symmetric problems and $2\pi$ otherwise

Subscripts

$\infty$	free stream conditions
$-$	downstream of an edge or surface discontinuity (see Figure 5)
$+$	upstream of an edge or surface discontinuity (see Figure 5)
$w$	wall
$f$	fin

## NOMENCLATURE (Cont.)

$\bar{n}_f$	fin surface normal vector upstream of a discontinuity
$\bar{n}$	vectors used in calculating compression or expansion jumps (see Figure 5)
$N$	number of $r$ planes
$P$	$\ln p$
$p$	pressure
$\bar{q}$	velocity vector
$q_n$	velocity component normal to a discontinuity
$q_t$	velocity component tangent to a discontinuity
$(r, \phi, z)$	cylindrical coordinates (see Figure 1)
$s$	entropy
$\bar{s}$	slip plane normal vector (see Figure 3)
$\vec{t}$	edge direction (see Figure 3)
$(u, v, w)$	velocity components (see Figure 1)
$(X, Y, Z)$	computational coordinates
$v_2$	$u(b_j/h) + v$
$v_3$	$v(r\sigma_r) + u$
$\alpha$	angle of attack
$\gamma$	ratio of specific heats



## APPENDIX A

## CHARACTERISTIC ANALYSIS OF THE FIN SURFACE

This Appendix presents a derivation of the equations used for advancing the fin surface points and the point on the fin-body junction. The analysis does not utilize the thin fin approximation and is valid for any gas in thermodynamic equilibrium.

The upper and lower fin surfaces are each independently described by  $\phi = \sigma(r, z) + \phi_f$ . On the upper surface, the flow region lies in  $\phi \geq \sigma(r, z) + \phi_f$  while, on the lower surface, the flow region lies in  $\phi \leq \sigma(r, z) + \phi_f$ . On each fin surface the inviscid boundary condition (22) must be satisfied. This constraint, in conjunction with the full system of equations (9) overspecifies the problem. The proper number of independent equations necessary for advancing the solution along the fin surfaces is obtained by combining the admissible characteristic compatibility conditions associated with (9), with (22) on the fin surface.

The two families of characteristics associated with (9) are stream surfaces and Mach surfaces. Each of these families provide an infinite number of surfaces on which the characteristic relations can be written. Except when considering points on the body-fin junction attention is restricted to planes shown in Figure A-1. The selected stream surface plane coincides with the fin surface and the chosen Mach surfaces intersect the fin surface along a constant  $z$  line. Two independent characteristic compatibility conditions are satisfied on the stream surface. These relations represent the propagation of disturbances for increasing  $z$  along the fin surface. Since the flow domain lies on just one side of each fin surface, only the compatibility condition for the Mach surface lying within the flow domain for  $z < z_0$  is considered admissible. This surface represents the propagation of disturbances from the interior points to the fin boundary for increasing  $z$ . The other Mach surface, which lies outside of the flow domain for  $z < z_0$ , is disregarded and replaced by the boundary condition (22). Application of admissible characteristic compatibility conditions at the boundaries in finite difference calculations was first suggested by Kentzer<sup>12</sup>. This approach was used in Reference 10 to develop the equations for advancing body surface and shock surface points (17) and (19).

For the characteristic analysis of a fin surface, it is convenient to temporarily introduce an additional transformation:

$$\begin{aligned}\zeta &= Z = z \\ \eta &= X = X(r, \phi, z) \\ \xi &= \xi(X, Y, Z) = \phi - \sigma - \phi_f\end{aligned}\tag{A.1}$$

AD-A116 904

NAVAL SURFACE WEAPONS CENTER SILVER SPRING MD F/G 16/4  
AN INVISCID COMPUTATIONAL METHOD FOR TACTICAL MISSILE CONFIGURA--ETC(U)  
DEC 81 A B WARDLAW, F P BALTAKIS, J M SOLOMON  
NSWC/TR-81-457 SBI-AD-F500 038 NL

UNCLASSIFIED

2/2

A  
GROUP 1



END  
DATE  
FILMED  
DTIC

END  
DATE  
FILMED  
DTIC

Note that in the  $\eta, \xi, \zeta$  coordinates,  $\eta = 0$  corresponds to the body alone surface and  $\xi = 0$  corresponds to the fin surface. A quasi-linear system equivalent to (22) is obtained by expanding (5) in terms of the dependent variables

$$Q = (p, u, v, w)^T,$$

introducing the change of variables (A.1), and left multiplying the result by the non-singular matrix:

$$\mathcal{D} = \begin{bmatrix} 1 & 0 & 0 & 0 \\ -w & 1 & 0 & 0 \\ -u & 0 & 1 & 0 \\ -v & 0 & 0 & 1 \end{bmatrix}.$$

The result is given by

$$L(Q) \equiv A \frac{\partial Q}{\partial \zeta} + B \frac{\partial Q}{\partial \eta} + C \frac{\partial Q}{\partial \xi} - \frac{1}{r} \mathcal{D} (E-F) = 0 \quad (\text{A.2})$$

where\*

$$A = \mathcal{D} \begin{bmatrix} \frac{\partial U}{\partial Q} \end{bmatrix}, \quad B = \mathcal{D} \left\{ \eta_z \begin{bmatrix} \frac{\partial U}{\partial Q} \end{bmatrix} + \eta_r \begin{bmatrix} \frac{\partial F}{\partial Q} \end{bmatrix} + \frac{1}{r} \eta_\phi \begin{bmatrix} \frac{\partial G}{\partial Q} \end{bmatrix} \right\},$$

$$C = \mathcal{D} \left\{ \xi_z \begin{bmatrix} \frac{\partial U}{\partial Q} \end{bmatrix} + \xi_r \begin{bmatrix} \frac{\partial F}{\partial Q} \end{bmatrix} + \frac{1}{r} \xi_\phi \begin{bmatrix} \frac{\partial G}{\partial Q} \end{bmatrix} \right\},$$

and  $\begin{bmatrix} \frac{\partial U}{\partial Q} \end{bmatrix}$ ,  $\begin{bmatrix} \frac{\partial F}{\partial Q} \end{bmatrix}$ ,  $\begin{bmatrix} \frac{\partial G}{\partial Q} \end{bmatrix}$  are the Jacobian matrices of  $U$ ,  $F$ , and  $G$ ,

respectively, taken with respect to the components of  $Q$  and subject to the energy equation (7). Explicit expressions for the matrices  $A$ ,  $B$ , and  $C$  can be obtained directly from (A.4), given below. Note that the terms  $\eta_z$ , etc. are given using (A.1) by

$$\eta_z = X_z, \quad \eta_r = X_r, \quad \eta_\phi = X_\phi$$

$$\xi_z = -\sigma_z, \quad \xi_r = -\delta_r, \quad \xi_\phi = 1. \quad (\text{A.3})$$

The pertinent facts concerning the theory of characteristics associated with system of the type (A.2) will be briefly reviewed here; for a more detailed explanation see Reference 28, pp. 577-599. The characteristic matrix associated with (A.2) is

$$A^* (\lambda_1, \lambda_2, \lambda_3) \equiv \lambda_1 A + \lambda_2 B + \lambda_3 C \quad (\text{A.4})$$

\* In terms of the transformation  $r, \phi, t \xrightarrow{\quad} \eta, \xi, \zeta$   
 $U = \tilde{U} r J^{-1}$ ;  $F = r J^{-1} (\eta_z \tilde{U} + \eta_r \tilde{F} + \frac{(\eta_\phi)}{r} \tilde{G})$ ;  $G = r J^{-1} (\xi_z \tilde{U} + \xi_r \tilde{F} + (\xi_\phi/r) \tilde{G})$

$$E = \tilde{E} J^{-1}; \quad J = \eta_r \xi_\phi - \xi_r \eta_\phi$$

$$\begin{bmatrix} \delta (1/a^2 - K/\rho) & \rho\Lambda_2 - u\sigma K & \rho\Lambda_3/r - v\sigma K & \rho\Lambda_1 - w\sigma K \\ \Lambda_1 & 0 & 0 & \rho\sigma \\ \Lambda_2 & \rho\sigma & 0 & 0 \\ \Lambda_3/r & 0 & \rho\sigma & 0 \end{bmatrix} = A^*$$

where

$$\sigma = \Lambda_1 w + \Lambda_2 u + \Lambda_3 v/r, \Lambda_1 = \lambda_1 + \eta_z \lambda_2 + \xi_z \lambda_3,$$

$$\Lambda_2 = \eta_r \lambda_2 + \xi_r \lambda_3, \Lambda_3 = \eta_\phi \lambda_2 + \xi_\phi \lambda_3,$$

$$\text{and } \rho K = (\partial \rho / \partial h)_p, (K = -1/h \text{ for a perfect gas}).$$

A surface  $\psi(\xi, \eta, \zeta) = 0$  is characteristic at a point if its normal at the point satisfies the characteristic condition

$$H(\lambda_1, \lambda_2, \lambda_3) \equiv \det [A^*(\lambda_1, \lambda_2, \lambda_3)] = 0$$

where  $\lambda_1 = \frac{\partial \psi}{\partial \zeta}$ ,  $\lambda_2 = \frac{\partial \psi}{\partial \eta}$ , and  $\lambda_3 = \frac{\partial \psi}{\partial \xi}$ . The characteristic conoid

with vertex  $O = (\zeta_0, \eta_0, \xi_0)$  is the envelope of all characteristic surfaces through  $O$ . The surface of the characteristic conoid is generated by curves, called rays or bicharacteristics which are the lines of contact between the characteristic surfaces and the conoid they envelope. These curves, or rays, are given by the ordinary differential equations

$$\frac{dZ}{dS} = \frac{\partial H}{\partial \lambda_1}, \frac{dX}{dS} = \frac{\partial H}{\partial \lambda_2}, \frac{dY}{dS} = \frac{\partial H}{\partial \lambda_3} \quad (A.6)$$

where  $S$  is a parameter. Each ray through  $\bar{O}$  is determined by selecting real values for  $\lambda_2$  and  $\lambda_3$  and determining  $\lambda_1$  by satisfying the characteristic condition (A.4) at  $O$ . The characteristic condition (A.4) for the system of equations (A.2) is given by

$$H = H_1(\lambda_1, \lambda_2, \lambda_3) H_2(\lambda_1, \lambda_2, \lambda_3) = 0$$

where

$$H_1(\lambda_1, \lambda_2, \lambda_3) = \frac{\rho^3 \sigma^2}{a^2} \quad \text{and} \quad (A.7)$$

$$H_2(\lambda_1, \lambda_2, \lambda_3) = \sigma^2 - (\Lambda_1^2 + \Lambda_2^2 + \Lambda_3^2/r^2) a^2$$

The ray cone therefore has two sheets, one corresponding to  $H_1 = 0$  and one corresponding to  $H_2 = 0$ . The rays generating the sheet corresponding to  $H_1 = 0$  are given, using (A.5), by

$$\frac{d\eta}{d\zeta} = A/w, \frac{d\xi}{d\zeta} = B/w$$

where  $\partial H_1 / \partial \lambda_1 = w$ ,  $\partial H_1 / \partial \lambda_2 = A \equiv \text{grad } \eta \cdot \vec{q}$ ,  $\frac{\partial H_1}{\partial \lambda_3} = B \equiv \text{grad } \xi \cdot \vec{q}$ .

Hence the sheet corresponding to  $H_1 = 0$  is a degenerate cone consisting of a single ray through 0. This ray corresponds in the physical space  $(z, \phi, r)$  to a streamline. The sheet corresponding to  $H_2 = 0$  is a true cone which corresponds in physical space to the Mach cone. For each characteristic surface, the lines of contact with the cone (bicharacteristic rays) have slopes given by:

$$\frac{d\eta}{d\xi} = (\partial H_2 / \partial \lambda_2) / (\partial H_2 / \partial \lambda_1), \quad \frac{d\xi}{d\eta} = (\partial H_2 / \partial \lambda_3) / (\partial H_2 / \partial \lambda_1). \quad (\text{A.8})$$

where

$$\begin{aligned} \partial H_2 / \partial \lambda_1 &= 2(\sigma w - a^2 \Lambda_1) \\ \partial H_2 / \partial \lambda_2 &= 2 \left[ \sigma(\text{grad } \eta \cdot \vec{q}) - a^2 (\Lambda_1 \eta_z + \Lambda_2 \eta_r + \frac{1}{r^2} \Lambda_3 \eta_\phi) \right] \\ \partial H_2 / \partial \lambda_3 &= 2 \left[ \sigma(\text{grad } \xi \cdot \vec{q}) - a^2 (\Lambda_1 \xi_z + \Lambda_2 \xi_r + \frac{1}{r^2} \Lambda_3 \xi_\phi) \right]. \end{aligned} \quad (\text{A.8a})$$

On each characteristic surface, the system (A.2) reduces to one or more scalar compatibility conditions given by

$$\vec{l} \cdot L(Q) = 0 \quad (\text{A.9})$$

where  $\vec{l}$  is a left null vector of  $A^*$  associated with the characteristic condition defining the characteristic surface. For the system (A.2), the left null vectors can be obtained from (A.4) by inspection. Corresponding to  $H_1 = 0$  (i.e.,  $\sigma = 0$ ) there are two independent left null vectors

$$\vec{l}_1 = (0, w, u, v) \quad (\text{A.10})$$

$$\vec{l}_2 = (0, 0, \frac{\Lambda_3}{r}, -\Lambda_2)$$

Corresponding to  $H_2 = 0$ , the left null vector is given by

$$\vec{l}_3 = (\rho\sigma, wK\sigma - \Lambda_1\rho, uK\sigma - \Lambda_2\rho, vK\sigma - \rho\Lambda_3/r) \quad (\text{A.11})$$

To determine the left null vectors, bicharacteristic rays, etc., values of  $\lambda_1, \lambda_2, \lambda_3$  must be specified. The characteristic conditions  $H_1 = H_2 = 0$  provide, for each family, one relation between  $\lambda_1, \lambda_2, \lambda_3$ . Since both  $H_1$  and  $H_2$  are homogeneous of degree 2 in  $\lambda_1, \lambda_2$  and  $\lambda_3$ , it follows that  $H_1 = 0$  and  $H_2 = 0$  each describes a one parameter families of characteristic surfaces.

As previously indicated, attention is restricted to characteristic surfaces which are either tangent to the fin surface or intersect the fin surface along  $\xi = \xi_0$ . Hence  $\lambda_2$  is set to zero and since  $w > a > 0$  the values of  $(\lambda_1/\lambda_3)$  on  $\xi = 0$ , which satisfy Eq. (A.4), are given by

$$\left(\frac{\lambda_1}{\lambda_3}\right)_0 = -\frac{B}{w} \text{ (multiplicity of 2) } (H_1 = 0)$$

$$\left(\frac{\lambda_1}{\lambda_3}\right)_{\pm} = \frac{(\xi_z a^2 \pm a\beta) \lambda_3}{w^2 - a^2} \quad (H_2 = 0) \quad (\text{A.12})$$

where

$$\beta = \sqrt{w^2 / |\text{grad } \xi|^2 - a^2 (\xi_r + \xi_\phi / r)}$$

and  $\lambda_3$  is any non zero value. Since on the fin surface  $B = 0$ , the characteristic surface corresponding to  $H_1 = 0$  with  $\lambda_2 = 0$  is tangent to the fin surface. Since these characteristic surfaces do not leave the flow domain, the associated compatibility conditions  $\tilde{x}_1 \cdot L(Q) = 0$  and  $\tilde{x}_2 \cdot L(Q) = 0$  (with  $\lambda_2 = 0$ ) are admissible on  $\xi=0$ . The final form of the associated compatibility equations used in the present work are given by (23) (corresponding to  $\tilde{x}_1$ ) and (24) (corresponding to  $\tilde{x}_2$ ). These can be obtained by direct substitution of (A.10) into (A.9) with  $\lambda_2 = 0$  and considerable manipulation using the boundary condition (20). In (23), the entropy  $s$  is introduced using the thermodynamic relation

$$dp - \rho dh = -\rho \tilde{T} ds$$

where  $\tilde{T}$  is the temperature. Note that the derivative  $\frac{\partial}{\partial z}$  and  $\frac{\partial}{\partial x}$ , appearing in these equations, are the same as  $\frac{\partial}{\partial \xi}$  and  $\frac{\partial}{\partial \eta}$ , respectively, on  $\xi=0$ .

For  $\lambda_2 = 0$ , there are two distinct characteristic surfaces (and left null vectors) associated with  $H_2 = 0$  corresponding to the values of  $\lambda_1/\lambda_3$  given by (A.12). To determine the appropriate choice of sign in (A.12), the slopes of the associated bicharacteristic rays through a point  $(\xi, \eta, 0)$  are considered. Using (A.8) and (A.12) yields

$$\frac{d\xi}{d\eta} = \frac{d\xi/ds}{d\eta/ds} = \frac{-a(a\xi_z \pm \beta)}{(w^2 - a^2)}$$

Since  $w > a > 0$  and  $\beta > w|\xi_z|$ , it follows that the bicharacteristics are as indicated in Figure A.1. For an upper fin surface, the flow region lies in  $\xi > 0$  and, therefore, the compatibility condition corresponding to the upper sign in (A.12) is the appropriate choice. Analogously, for a lower fin surface the lower sign is the appropriate choice. For both fin surfaces, the compatibility condition (A.9) on  $\xi = 0$  with  $\tilde{x} = \tilde{x}_3$  is given by (24). This is obtained, after considerable manipulation, by evaluating (A.9) on  $\xi = 0$ ,

using the boundary condition (22) with  $\lambda_2 = 0$ ,  $\lambda_3 \neq 0$ , and  $\lambda_1/\lambda_3$  defined by (A.12). Also,  $\frac{\partial}{\partial \eta}$  is replaced by  $\partial/\partial \eta = Y_\xi (\partial/\partial Y)$

where  $Y_\xi = Y_\phi X_r / (X_r + \sigma_r X)$ ; cf., (A.1) and (1).

The above analysis does not apply to the points  $(\zeta, 0, 0)$  along the fin-body junction. These points are special in that they are boundary corners where the flow domain lies in the sector between the body surface and the fin upper (or lower surface: viz., the quarter plane  $\{\eta \geq 0, \xi \geq 0\}$  or  $\{\eta \geq 0, \xi \leq 0\}$ ). The fin-body junction is modeled in a heuristic manner which leads to a separate set of equations for these points. Along the junction, both (22) and (13) are satisfied which implies that the junction is a streamline. It is also assumed that the junction is not a vortical singularity (i.e., the entropy, pressure, etc. are single valued along the junction). Under these circumstances, the compatibility condition (A.9) with  $\tilde{\kappa} = \tilde{\kappa}_1$  implies that  $s$  is constant along the junction. Therefore, because of (22) and (13), only one other independent relation is needed to determine all the flow variables at the junction.

Of the two remaining families of compatibility conditions, only those corresponding to  $\tilde{\kappa}_3$  (i.e., associated with  $H_2 = 0$ ) are considered. From these compatibility conditions an equation can be obtained for advancing the pressure  $p$  along the junction which is independent of (22), (13) and  $s = \text{constant}$ . On the other hand, it can be shown that the compatibility conditions corresponding to  $\tilde{\kappa}_2$  for any choice of  $\lambda_2$  and  $\lambda_3$  (with  $\lambda_2 + \lambda_3 \neq 0$ ) is not independent of (22) and (13) when  $b_z = \sigma_z = 0$  (a case that we do not want to exclude). The specific choice of a compatibility condition from the  $H_2 = 0$  family, is dictated by the fact that the flow domain is a sector and only those compatibility conditions associated with bicharacteristic rays through  $(\zeta, 0, 0)$  which lie in the appropriate sector for decreasing  $\zeta$  should be considered. Among the bicharacteristics associated with  $H_2 = 0$  satisfying this condition there appears to be no particularly convenient choice. One possibility is the bicharacteristic lying on the fin surface at  $(\zeta, 0, 0)$ ; i.e.,  $\partial \xi / \partial \zeta = 0$  at  $(\zeta, 0, 0)$ . From (A.8), this bicharacteristic satisfies  $\partial H_2 / \partial \lambda_3 = 0$ . Simultaneous solution of  $H_2 = 0$  and  $\partial H_2 / \partial \lambda_3 = 0$ , using (22) and (13), yields two possibilities given by

$$\lambda_{1\pm} = a \lambda_2 [a(R\eta_z - T\xi_z) \pm \sqrt{R} \beta^*] / \Omega \quad (\text{A.13})$$

$$\lambda_{3\pm} = -\lambda_2 [(w^2 - a^2) T + a^2 \eta_z \xi_z \pm a \xi_z \beta^* / \sqrt{R}] / \Omega$$

where  $\beta^* = (SR - T^2) (w^2 - a^2) + a^2 (R \eta_z^2 - 2T \eta_z \xi_z + \xi_z^2)$ ,

$R = |\text{grad } \xi|^2$ ,  $S = |\text{grad } \eta|^2$ ,  $T = \text{grad } \eta \cdot \text{grad } \xi$ ,  $\Omega = R(w^2 - a^2) + \xi_z^2 a^2$ ,

and  $\lambda_2 \neq 0$ . To determine the appropriate choice to sign in (A.13), we consider the shape of the bicharacteristic rays determined by (A.13). It follows from (A.8) and (A.13) using (22) and (13), that at  $(\zeta, 0, 0)$

$$d\eta/d\zeta = -a [a(R\eta_z - T\xi_z) \pm \sqrt{R} \beta^*] / \Omega \quad (\text{A.14})$$

Since  $w > a > 0$  and  $RS > T^2$ , it follows that  $\sqrt{R} \beta^* > a |R \eta_z - T \xi_z|$  and thus the bicharacteristics corresponding to (A.13) are as indicated in Figure A-2. Therefore for both the upper and lower fin surfaces the upper sign in (A.13) is the appropriate choice. The form of the compatibility condition (A.9) on  $(\zeta_0, 0, 0)$  with  $\ell = \ell_3$  and  $\lambda_1, \lambda_3$  defined by (A.13) is independent of  $\lambda_2$  and given by (24a). Another possibility is to consider the compatibility condition associated with bicharacteristic ray lying on the body surface,  $\eta = 0$ ; i.e.,  $\partial \zeta / \partial \xi = 0$  at  $(\zeta, 0, 0)$ . These bicharacteristics satisfy  $\partial H_2 / \partial \lambda_2 = H_2 = 0$  which give  $\lambda_1$  and  $\lambda_2$  in terms of an arbitrary  $\lambda_3 \neq 0$  expressed by (A.13) with  $\lambda_2$  and  $\lambda_3$ ,  $\xi_z$  and  $\eta_z$ , and  $R$  and  $S$  interchanged. To determine the sign,  $d\xi/d\xi$  which is given by the right hand side of (A.14) is considered with the above interchanges. The corresponding bicharacteristics are indicated in Fig. A-2. Hence the appropriate choice of sign is the upper and lower sign for the upper and lower surface junctions, respectively. This compatibility condition, evaluated at the junction, is given by (24b).



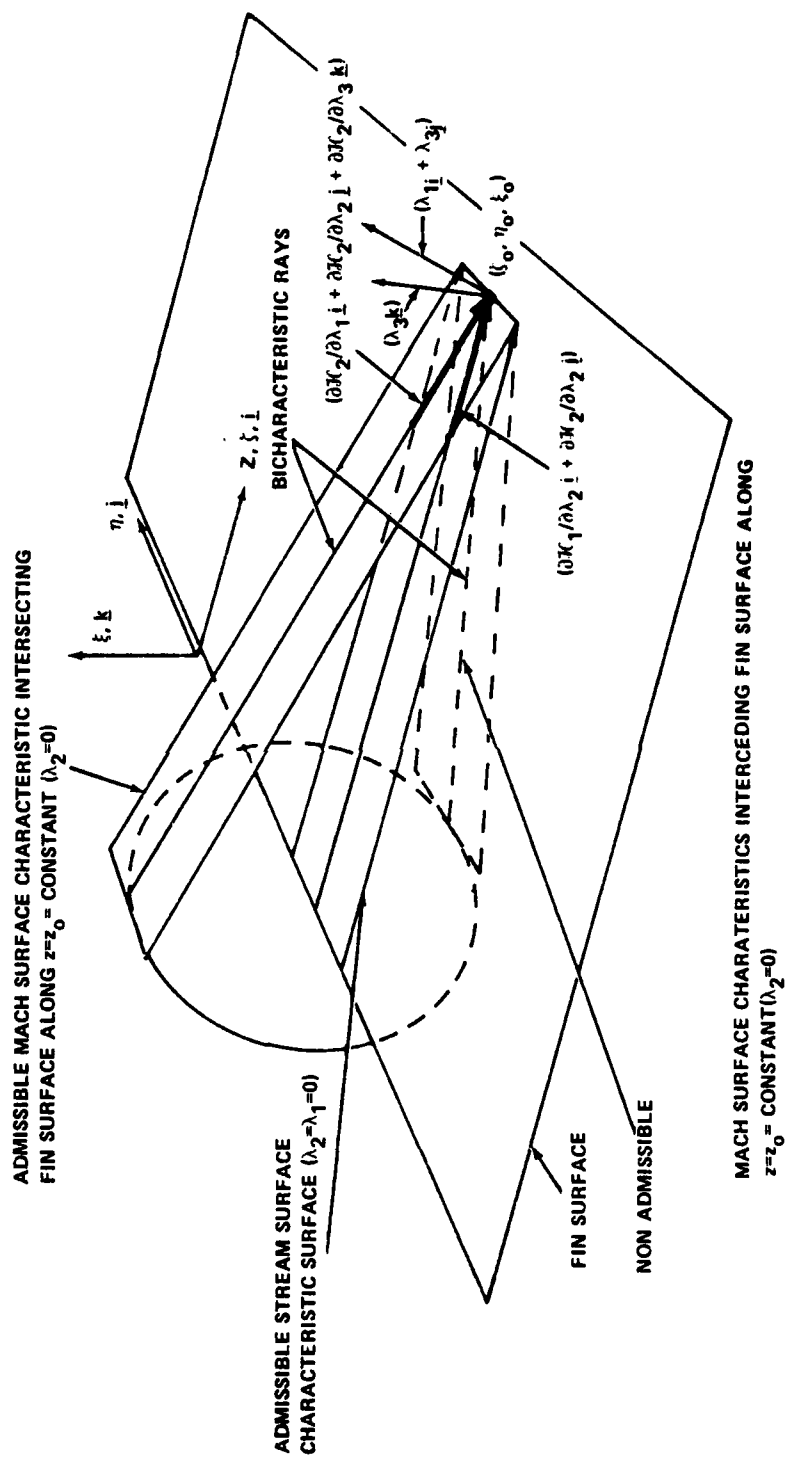


Figure A-1 Characteristic surfaces associated with the upper fin surface

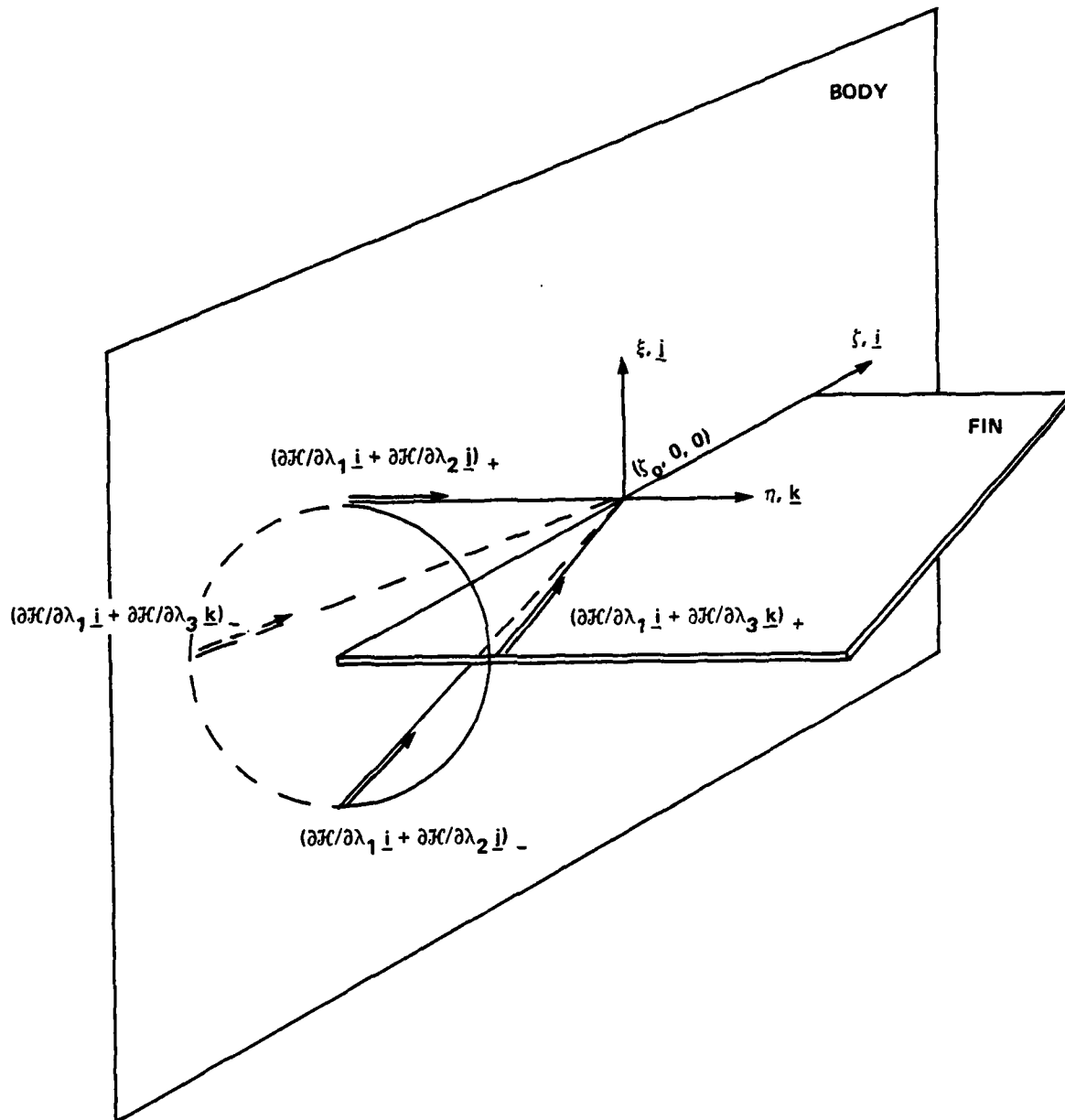


Figure A-2. Bicharacteristic rays associated with body-fin junction

## APPENDIX B

## CALCULATION OF AERODYNAMIC COEFFICIENTS

The aerodynamic forces acting on a missile configuration are determined by numerically integrating the computed fin and body surface pressure distributions. The sign conventions for the components of the aerodynamic force and moment are illustrated in Fig. B-1. The force and moments are computed assuming that the base pressure is equal to  $p_\infty$  and that the moments are taken about the point  $z = z_c$  on the  $z$  axis, as is shown in Fig. B-1. The derivatives with respect to  $z$  of the force components are given by:

$$\frac{\partial F_z}{\partial z} = \sum_{i=1}^{N_f} \int_{\phi_i^a}^{\phi_i^b} p_b b b_z d\phi + \sum_{n=1}^{N_s} S_n \int_{r_{in}}^{r_{on}} p_b(r\sigma_z) dr \quad (B-1)$$

$$\frac{\partial F_n}{\partial z} = \sum_{i=1}^{N_f} \int_{\phi_i^a}^{\phi_i^b} p_b (b \cos\phi + b_\phi \sin\phi) d\phi - \sum_{n=1}^{N_s} \int_{r_{in}}^{r_{on}} p_b [\sin\phi_f + (r\sigma_r) \cos\phi_f] dr \quad (B-2)$$

$$\frac{\partial F_y}{\partial z} = \sum_{i=1}^{N_f} \int_{\phi_i^a}^{\phi_i^b} p_b (b_\phi \cos\phi - b \sin\phi) d\phi + \sum_{n=1}^{N_s} S_n \int_{r_{in}}^{r_{on}} p_b [\cos\phi_f - (r\sigma_r) \sin\phi_f] dr \quad (B-3)$$

$$\begin{aligned} \frac{\partial M_z}{\partial z} = & - \sum_{i=1}^{N_f} \int_{\phi_i^a}^{\phi_i^b} p_b b b_\phi d\phi \\ & - \sum_{n=1}^{N_s} S_n \int_{r_{in}}^{r_{on}} p_b \{ \cos\phi_s [\cos\phi_f - (r\sigma_r) \sin\phi_f] + \sin\phi_s [\sin\phi_f + (r\sigma_r) \cos\phi_f] \} r dr \end{aligned} \quad (B-4)$$

$$\frac{\partial M_x}{\partial z} = (z_c - z) \frac{\partial F_y}{\partial z} + \sum_{i=1}^{N_f} \int_{\phi_i^a}^{\phi_i^b} p_b b^2 b_z \sin\phi d\phi + \sum_{n=1}^{N_s} S_n \int_{r_{in}}^{r_{on}} p_b \sin\phi_s (r\sigma_z) r dr \quad (B-5)$$

$$\frac{\partial M_y}{\partial z} = (z - z_c) \frac{\partial F_n}{\partial z} + \sum_{i=1}^{N_f} \int_{\phi_i^a}^{\phi_i^b} p_b b^2 b_z \cos \phi \, d\phi + \sum_{n=1}^{N_s} S_n \int_{r_{in}}^{r_{on}} p_b \cos \phi_s (r \sigma_z) r dr \quad (B-6)$$

where  $p_b = p - p_\infty$ ,  $\phi_s = \phi$  on fin surface,  $\phi_f = \phi$  of fin plane

The first term in each case represents the body contribution while the second, that of the fins. In the above equations,  $N_s$  is the number of fin surfaces and  $N_f - 1$  is the number of fins not on plane  $\phi = \phi_*$  or  $\phi = 0$ . The parameter  $S_n$  has the value of +1 and -1 on the upper and lower fin surface respectively. As shown in Fig. B-2, the radial locations of the inner and outer fin edges are denoted by  $r_o$  and  $r_i$ , and the quantities  $\phi_i^a$  and  $\phi_i^b$  represent the angular locations of the upper and lower surfaces of the fins number  $i$  and  $i+1$  respectively. In the above,  $\phi_s - \phi_f$  represents the fin thickness, which for the purposes of force and moment calculations has not been set to zero. For test cases discussed in Section 5,  $\phi$  is set to  $\phi_f$  and hence fin thickness is neglected. In the case of pitch plane symmetry:

$$\frac{\partial F_y}{\partial z} = \frac{\partial M_z}{\partial z} = \frac{\partial M_x}{\partial z} = 0$$

The integrals appearing in (B-1) to (B-6) are computed numerically at each step,  $z = z^k$ . The body integrals are all of the form:

$$\tilde{\psi} = \sum_{i=1}^{N_f} \int_{\phi_i^a}^{\phi_i^b} \tilde{v}(\phi) d\phi$$

These are evaluated using

$$\tilde{\psi} = \psi - \sum_{i=1}^{N_f} \frac{1}{2} [\tilde{v}(\phi_i^b) + \tilde{v}(\phi_{i+1}^a)] (\phi_{i+1}^a - \phi_i^b)$$

$$\text{where: } \psi = \int_0^{\phi_*} \tilde{v}(\phi) d\phi \quad ; \quad \phi_o^b = 0 \quad ; \quad \phi_{N_f+1}^a = \phi_*$$

In evaluating  $\psi$ , the body surface pressure on fin planes is taken to be an average of the surface pressure on the upper and lower body fin junctions. It is more convenient to perform the integration of equations in the computational plane. In the symmetric case the above becomes:

$$\psi = 2 \int_0^1 \frac{\tilde{v}(\phi)}{Y_\phi} dY = 2 \int_0^1 v(Y) dY$$

This is numerically integrated on the uniform computational mesh using Simpson's rule in the form

$$\psi = \frac{2\Delta Y}{3} [v_1 + 4v_2 + 2v_3 + 4v_4 + 2v_5 + \dots \\ \dots + 2v_{M-2} + 4v_{M-1} + v_M], \text{ if } M \text{ is odd}$$

and

$$\psi = \frac{2\Delta Y}{3} [v_1 + 4v_2 + 2v_3 + 4v_4 + 2v_5 + \dots \\ \dots + 2v_{M-3} + 4v_{M-2} + \frac{1}{2}(5v_{M-1} + 3v_M)], \text{ if } M \text{ is even.}$$

In the above,  $v_m = v(Y_m)$ ,  $Y_M = 1$  and  $\Delta Y = 1/(M-1)$ . In the last expression, the trapezoidal rule is used for the subinterval  $[Y_{M-1}, Y_M]$ . In the nonsymmetric problem  $\psi$  is written as

$$\psi = \int_0^1 \frac{\tilde{v}(\phi)}{Y_\phi} dY = \int_0^1 v(Y) dY$$

In this case, the integrands are periodic functions of  $Y$  with period 1 (i.e.,  $v(0) = v(1)$ ) and the Simpson's rule becomes

$$\psi = \frac{\Delta Y}{3} [2v_1 + 4v_2 + 2v_3 + 4v_4 + \dots \\ \dots + 2v_{M-1} + 4v_M], \text{ if } M \text{ is odd}$$

and

$$\psi = \frac{\Delta Y}{3} [6v_1 + 3v_2 + 2v_3 + 4v_4 + 2v_5 + \dots \\ \dots + 2v_{M-2} + 4v_{M-1}], \text{ if } M \text{ is even,}$$

where  $v_m = v(Y_m)$ ,  $Y_m = 1 - \Delta Y$  and  $\Delta Y = 1/M$ .

Integration over the fin surfaces is more cumbersome since inner and outer fin edges in every crossflow plane need not coincide with a grid point. Also the fin may consist of many or only a single grid point. In order to allow for leading edge functions which are double valued in  $z$ , such as on an arrow fin, the fin is not required to extend to the body surface. Fin surface integrals have the form:

$$\Psi = \int_{r_i}^{r_o} \tilde{v}(r) dr$$

The integration is carried out in computational coordinates and leads to:

$$\Psi = \int_{X_I}^{X_O} \frac{\tilde{v}(r)}{X_r} dX = \int_{X_I}^{X_O} v(X) dX$$

Here  $X_i$  and  $X_o$  are the inner and outer fin edge locations. Consider the case where the inner-most and outer-most grid points on the surface of the fin occur at  $X_{n_i}$  and  $X_{n_o}$  respectively. The fin surface integral is expressed in

three parts:

$$\Psi = \int_{X_i}^{X_{n_i}} v dX + \int_{X_{n_i}}^{X_{n_o}} v dX + \int_{X_{n_o}}^{X_o} v dX \quad (B-7)$$

The first and last terms are approximated by:

$$\int_{X_i}^{X_{n_i}} v dX = v_{n_i} (X_{n_i} - X_i) ; \quad \int_{X_{n_o}}^{X_o} v dX = v_{n_o} (X_o - X_{n_o})$$

where  $v_{n_i} = v(X_{n_i})$ ,  $v_{n_o} = v(X_{n_o})$ . The remaining term is evaluated using

Simpson's rule which requires that there be an odd number of points on the fin. If the fin contains an even number of points, the outer most interval  $[X_{n_o} - \Delta X, X_{n_o}]$  is evaluated using the trapezoidal rule while the remaining

interval which now consists of an odd number of points is evaluated using Simpson's rule. This leads to the following integration formula for terms 1, 2, and 3:

odd:

$$\int_{X_i}^{X_o} v dx = v_{n_o} (X_o - X_{n_o} + \frac{\Delta X}{3}) + v_{n_i} (X_{n_i} - X_i + \frac{\Delta X}{3}) + \left\{ 4v_{n_i+1} + 2v_{n_i+2} + 4v_{n_i+3} \dots 4v_{n_o-1} \right\} \frac{\Delta X}{3}$$

even:

$$\int_{X_i}^{X_o} v dx = v_{n_o} (\frac{\Delta X}{2} + X_o - X_{n_o}) + \frac{\Delta X}{6} v_{n_o-1} + v_{n_i} (X_{n_i} - X_i + \frac{\Delta X}{3}) + \left\{ 4v_{n_i+1} + 2v_{n_i+2} + 4v_{n_i+3} \dots 4v_{n_o-2} \right\} \frac{\Delta X}{3} + v_{n_o-1} \Delta X (\frac{5}{2})$$

where  $\Delta X = 1/N$

The code also computes, at each computational step,  $Z^k$ , the force and moment vectors acting on the body truncated at  $z = Z^k$ . These quantities are defined, for example, by

$$F_a(Z^k) = \int_0^{Z^k} \frac{\partial F_a}{\partial z} dz \quad (B-8)$$

with similar expressions for the other truncated force and moment components. The integrals of the type (B-8) are evaluated numerically using the trapezoidal rule; i.e.,

$$F_a(Z^{k+1}) = F_a(Z^k) + \left( \frac{Z^{k+1} - Z^k}{2} \right) \left[ \left( \frac{\partial F_a}{\partial z} \right)_{z=Z^k} + \left( \frac{\partial F_a}{\partial z} \right)_{z=Z^{k+1}} \right]$$

with similar expressions for the other force and moment coefficients. Note that this calculation requires the force and moment on the body truncated at the initial plane  $z = z_0$ . These quantities must be given along with the initial flow field data.

The final results are presented in coefficient form by dividing the force components and their derivatives by  $\frac{\rho_\infty}{2} V_\infty^2 A_{ref}$  and the moment components and their derivative by  $\frac{\rho_\infty}{2} V_\infty^2 (A_{ref}) (z_{ref})$ , where  $A_{ref}$  and  $z_{ref}$  are reference area and reference lengths respectively.

The centers of pressure in the pitch and yaw planes are also calculated using:

$$(Z_{cp})_p = [Z_c + M_y/F_n]$$

$$(Z_{cp})_y = [Z_c - M_x/F_y]$$

for  $F_y \neq 0$  and  $F_n \neq 0$ .

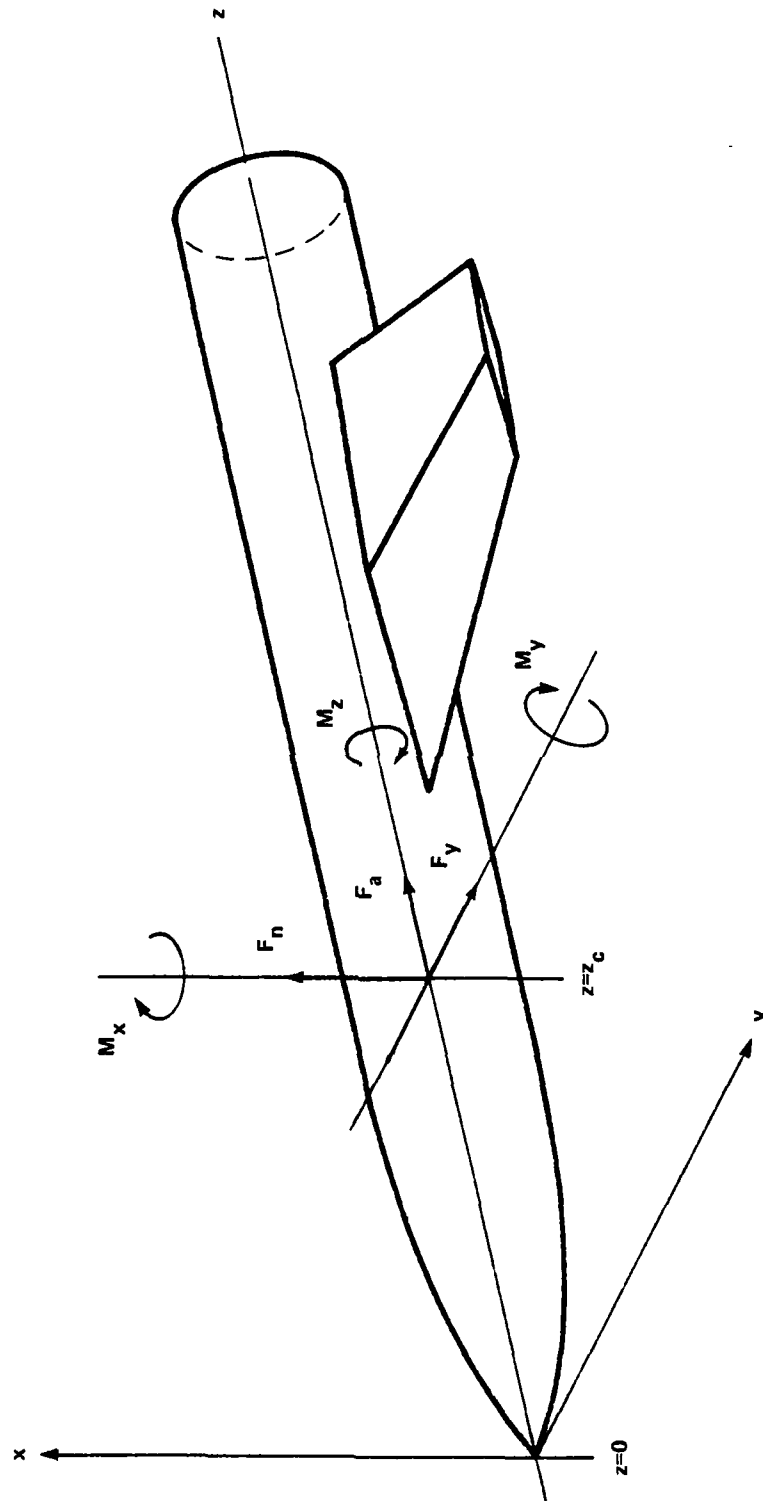


Figure B-1. Coordinate system used when computing aerodynamic force and moment coefficients



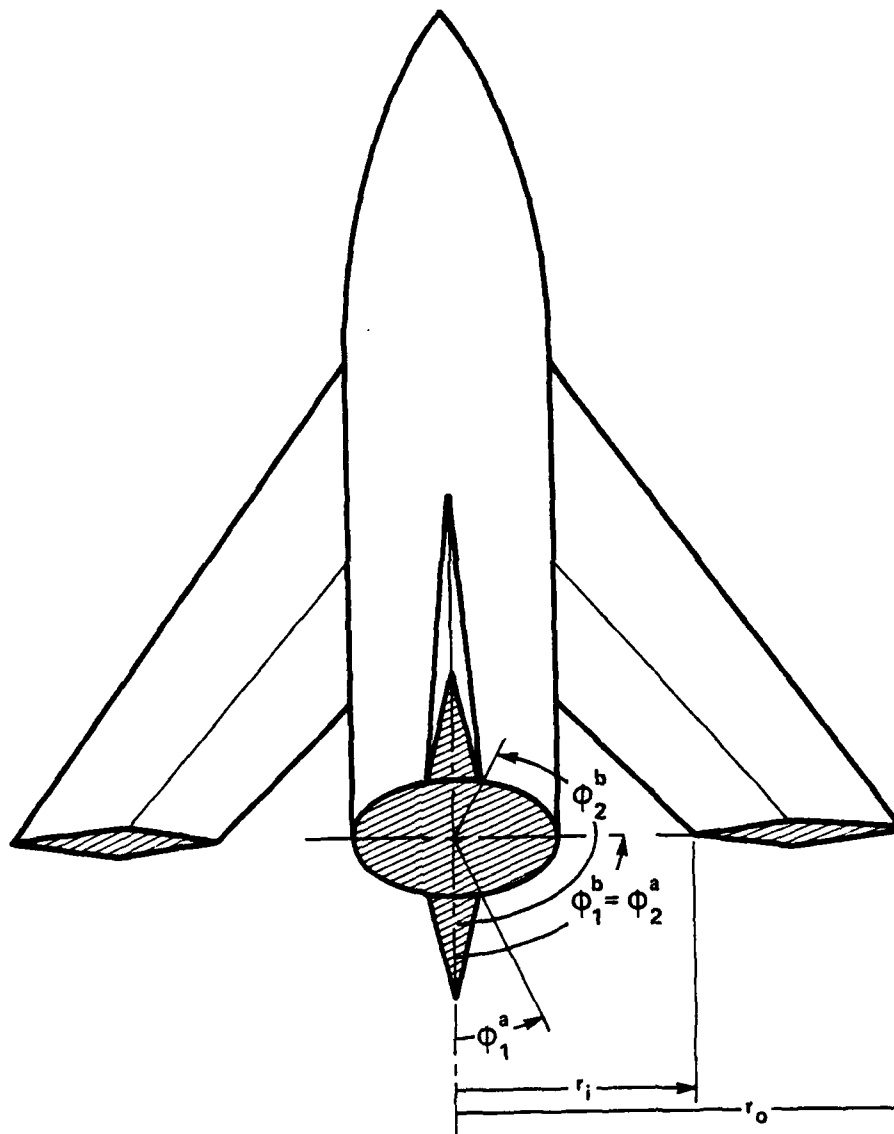


Figure B-2. Definition of parameters used in integration of force and moment coefficients

## DISTRIBUTION

	<u>Copies</u>		<u>Copies</u>
Commander		Commander	
Naval Sea Systems Command		David W. Taylor Naval Ship	
Attn: SEA 62R41, Mr. L. Pasiuk	1	Research and Development	
Technical Library	1	Center	
Washington, DC 20362		Attn: Dr. T. C. Tai	1
Chief of Naval Material		Mr. M. J. Malia	1
Attn: Mr. S. Jacobson (MAT 032)	1	Technical Library	1
Dr. John Huth	1	Washington, DC 20007	
Technical Library	1	Office of Naval Research	
Washington, DC 20360		Attn: Mr. D. Siegel	1
Commander		Dr. R. Whitehead	1
Naval Air Systems Command		Technical Library	1
Attn: AIR-320C	1	800 N. Quincy Street	
AIR-330D, Dr. W. H. Clark	1	Arlington, VA 22217	
AIR-530, S. Loezos	1	Commanding Officer	
Technical Library	1	Naval Air Development Center	
Washington, DC 20361		Attn: Mr. S. Greenhalgh	1
Commander		Mr. C. Rietz	1
Naval Weapons Center		Technical Library	1
Attn: Mr. R. Van Aken	1	Warminster, PA 18974	
Mr. R. Meeker	1	Superintendent	
Mr. Lloyd Smith	1	U.S. Naval Academy	
Mr. R. E. Smith	1	Attn: Head, Weapons Dept.	1
Mr. H. Schafer	1	Head, Science Dept.	1
Technical Library	1	Dr. A. Maddox	1
China Lake, CA 93555		Technical Library	1
Commander		Annapolis, MD 21402	
Pacific Missile Test Center		Superintendent	
Attn: Mr. J. Rom	1	U.S. Naval Postgraduate School	
Mr. G. Cooper	1	Attn: Technical Library	1
Technical Library	1	Monterey, CA 95076	
Point Mugu, CA 93041		Officer in Charge	
		Naval Intelligence Support	
		Center	
		Attn: J. B. Chalk	1
		Technical Library	1
		4301 Suitland Road	
		Washington, DC 20390	

## DISTRIBUTION (Cont.)

	<u>Copies</u>		<u>Copies</u>
Commanding Officer Naval Ordnance Station Attn: Technical Library Indian Head, MD 20640	1	Commanding Officer Harry Diamond Laboratories Attn: Technical Library Adelphi, MD 20783	1
Director, Development Center Marine Corps Development and Education Center Quantico, VA 22134	1	Arnold Engineering Development Center Attn: Mr. J. Usselton Mr. W. B. Baker, Jr. Technical Library	1 1 1
Chief of S and R Division Development Center Marine Corps Development and Education Center Quantico, VA 22134	1	USAF Tullahoma, TN 37389	
Commanding General Ballistic Research Laboratory Attn: Dr. C. H. Murphy Mr. L. McAllister Mr. A. Platou Mr. R. McCoy Dr. R. Sedney Dr. W. Sturek Mr. C. Nietubicz Technical Library Aberdeen Proving Ground, MD 21005	1 1 1 1 1 1 1 1	Commanding Officer Air Force Armament Laboratory Attn: Dr. D. Daniel Mr. C. Butler Mr. K. Cobb Mr. C. Mathews Mr. E. Sears Mr. F. Stevens Dr. L. E. Lijewski Eglin Air Force Base, FL 32542	1 1 1 1 1 1 1
Commanding General ARRADCOM Picatinny Arsenal Attn: Mr. A. Loeb Mr. H. Hudgins Mr. G. Friedman Mr. W. Gadowski Technical Library Dover, NJ 07801	1 1 1 1 1	USAF Academy Attn: Technical Library Colorado Springs, CO 80912	1
Commanding General U.S. Army Missile R and D Command DROMI-TDK Redstone Arsenal Attn: Mr. R. Deep Dr. D. J. Spring Technical Library Huntsville, AL 35809	1 1 1 1	Commanding Officer Air Force Wright Aeronautical Laboratories (AFSC) Attn: Dr. G. Kurylowich Mr. D. Shereda Mr. J. Jenkins Mr. D. Hoak Mr. G. Fleeman Mr. M. Pinney Wright-Patterson Air Force Base, OH 45433	1 1 1 1 1
		Defense Advanced Research Projects Agency Attn: Technical Library Department of Defense Washington, DC 20305	1
		NASA Attn: Technical Library Washington, DC 20546	1

## DISTRIBUTION (Cont.)

	<u>Copies</u>		<u>Copies</u>
NASA Ames Research Center		Applied Physics Laboratory	
Attn: Dr. G. Chapman	1	The Johns Hopkins University	
Mr. V. L. Peterson	1	Attn: Dr. L. L. Cronvich	1
Technical Library	1	Mr. E. T. Marley	1
Moffett Field, CA 94035		Mr. J. C. Hagan	1
		Mr. E. Lucero	1
NASA Langley Research Center		Mr. L. Tisserand	1
Attn: Mr. J. South	1	Mr. G. J. Pietrangeli	1
Mr. L. Spearman	1	Technical Library	1
Mr. C. M. Jackson, Jr.	1	Johns Hopkins Road	
Mr. W. C. Sawyer	1	Laurel, MD 20810	
Dr. R. C. Swanson, Jr.	1		
Miss E. J. Landrum	1	Raytheon Company	
Technical Library	1	Missile Systems Division	
Langley Station		Attn: Mr. D. P. Forsmo	1
Hampton, VA 23365		Technical Library	1
		Hartwell Road	
Virginia Polytechnic Institute		Bedford, MS 01730	
and State University			
Department of Aerospace		McDonnell-Douglas Astronautics	
Engineering		Co. (West)	
Attn: Dr. J. A. Schetz	1	Attn: Dr. J. Xerikos	1
Dr. C. H. Lewis	1	Technical Library	1
Technical Library	1	5301 Bolsa Avenue	
Blacksburg, VA 24060		Huntington Beach, CA 92647	
North Carolina State University		McDonnell-Douglas Astronautics	
Department of Mechanical and		Co. (East)	
Aerospace Engineering		Attn: Mr. J. Williams	1
Attn: Dr. F. R. DeJarnette	1	Mr. S. Vukelich	1
Technical Library	1	Technical Library	1
Box 5246		Box 516	
Raleigh, NC 27607		St. Louis, MO 61366	
The University of Tennessee		Lockheed Missiles and Space	
Space Institute		Co., Inc.	
Attn: Dr. J. M. Wu	1	Attn: Dr. D. Andrews	1
Mr. C. Balasubramayan	1	Technical Library	1
Technical Library	1	P.O. Box 1103	
Tullahoma, TN 37388		Huntsville, AL 35807	
University of Notre Dame		Lockheed Missiles and Space	
Department of Aerospace and		Co., Inc.	
Mechanical Engineering		Attn: Dr. Lars E. Ericsson	1
Attn: Dr. R. Nelson	1	Mr. P. Reding	1
Technical Library	1	Mr. H. S. Shen	1
Box 537		Technical Library	1
Notre Dame, IN 46556		P.O. Box 504	
		Sunnyvale, CA 94086	

## DISTRIBUTION (Cont.)

	<u>Copies</u>		<u>Copies</u>
Nielsen Engineering and Research, Inc. 510 Clyde Avenue Mountain View, CA 95043	1	Martin Marietta Aerospace Attn: Mr. G. F. Aiello Technical Library P.O. Box 5837 Orlando, FL 23855	1 1
General Electric Co. Armament Systems Department Attn: Mr. R. Whyte Burlington, VT 05401	1	Business and Technology Systems, Inc. Attn: Dr. J. B. Eades, Jr. Suite 400 Aerospace Building 10210 Greenbelt Road Seabrook, MD 20801	1
CAL SPAN Advanced Technology Center Attn: Mr. B. Omilian P.O. Box 400 Buffalo, NY 14225	1	Lawrence Livermore Laboratory Earth Sciences Division Attn: Mr. D. G. Miller Technical Library University of California Livermore, CA 94550	1 1
Northrop Services, Inc. Attn: W. Boyle Huntsville, AL 35810	1	Honeywell, Inc. Attn: Mr. S. Sopszak Technical Library 600 Second Street Minneapolis, MN 55343	1 1
Science Applications Inc. Attn: Mr. P. Murad 680 E. Swedesford Road Wayne, PA 19087		Pacifica Technology Attn: Dr. H. T. Ponsford P.O. Box 148 Del Mar, CA 92014	1 1
Vought Corporaton Attn: Mr. F. Prillman Dr. W. B. Brooks Mr. R. Stancil P.O. Box 225907 Dallas, TX 75265	1 1 1	Rockwell International Missile Systems Division Attn: Mr. J. E. Rachner Technical Library 4300 E. Fifth Avenue P.O. Box 1259 Columbus, OH 43216	1 1
Hughes Aircraft Corporation Missiles Systems Group Attn: Dr. J. Sun Technical Library 8433 Fallbrook Avenue Canoga Park, CA 91304	1 1	Boeing Computer Services, Inc. Attn: Mr. R. Wyrick P.O. Box 24346 Seattle, WA 98124	1 1
Sandia Laboratories Attn: Mr. R. La Farge Mr. R. Eisler Mr. W. Wolfe Technical Library Albuquerque, NM 87115	1 1 1 1		

NSWC TR 81-457

DISTRIBUTION (Cont.)

	<u>Copies</u>		<u>Copies</u>
Motorola Inc.		Library of Congress	
Missile Systems Operations		Attn: Gift and Exchange	
Attn: Mr. G. H. Rapp	1	Division	1
8201 East McDowell Road		Washington, DC 20390	
P.O. Box 1417			
Scottsdale, AZ 85252		GIDEP Operations Office	
		Corona, CA 91720	1
Raytheon Company			
Spencer Laboratory		Defense Printing Service	
Attn: Mr. S. Pearlsing	1	Washington Navy Yard	
Mr. P. Giragosian	1	Washington, DC 20374	1
Box SL7162			
Burlington, MA 01803		EG&G Washington Analytical	
		Services Center, Inc.	
Defense Technical Information		Attn: Technical Library	1
Center		P.O. Box 552	
Cameron Station		Dahlgren, VA 22448	
Alexandria, VA 22314	12		

